Diamond unipolar devices: Towards impact ionization coefficients extraction

DRICHE Khaled

December 2018

Diamond unipolar devices: Towards impact ionization coefficients extraction

DRICHE Khaled

Doctoral Program in Applied Physics

Submitted to the Graduate School of
Pure and Applied Sciences
in Partial Fulfillment of the Requirements
for the Degree of Doctor of Philosophy in
Engineering

at the
University of Tsukuba

Contents

Introduction

Climate change... 97% of the published climate studies articles agree with the fact that recent global warming is entirely caused by human activities [1]. Since the industrial revolution, the constant demand for more energy consumption (consistent with population increase), more efficient technologies and small size components (Moore's Law) increases over the years. The gases emitted to produce electrical energy (CO_2, CH_4, etc.) plus other gases rejected by actual cars (such as CO_2) impact considerably on the atmosphere by greenhouse effect - without referring other factors. As humans are responsible for global warming, then humans have to fixe the problem. One solution, if we need to continue using electrical energies, is the development of components with lower power conduction losses and higher breakdown characteristics that could be used in nuclear power plants, high-power commutation cells, hybrid (electric) cars and so on.

The choice of the material to reach low power conduction losses and higher breakdown is of great importance. Nowadays, silicon-based devices control about 95% of all electronic components. Silicon carbide SiC and gallium nitride GaN are at present under research and development and start to be integrated into some electronic circuits such as to control the power of indoor air conditioners or inverters systems for railway cars, and other materials like Ga_2O_3, AlN or diamond are still under research for power electronic application. The laters are known as ultra wide bandgap materials, and they seem to be the required solution against low power losses. Among them, diamond is one of the promising materials for the next next-generation devices owing to its exceptional physical and electrical properties such as high breakdown field ($\geq$ 10 MV/cm) to use the device for high power control, high carrier mobility (2000 cm^2/V.s for holes and 1000 cm^2/V.s for electrons) for fast switching and high frequency devices, high saturation velocity, high thermal conductivity (22 W/cm.K) for a perfect heat dissipation and low dielectric constant (5.5 eV). Many teams are working to improve the quality of diamond substrates, devices, and extracting material parameters to reveal the strength of diamond to be used for power electronic applications [2]. Theoretically, diamond is the best semiconducting material capable of having high breakdown voltages and low specific-on resistances. Especially, due to the incomplete ionization of the dopant (boron with ionization energy of 380 meV for p-type and phosphorus with ionization energy of 570 meV for n-type), it is even more efficient at high temperature. Various diamond Schottky barrier diodes (SBDs) - to control the direction of the current flow - with good forward ($\geq 10^3$ A.cm^2 at 6 V) and good reverse performances (blocking capability more than 1 kV with leakage current below 1 pA) were already reported [3, 4]. Additionally to SBDs, switches diamond field effect transistors (FETs) were also investigated through metal-oxide-semiconductor FETs (MOSFETs) using either an H-terminated diamond surface with not negligible current densities in on-state [5, 6] or an O-terminated one with high blocking characteristics [7, 8, 9]. Similar studies were done for metal-semiconductor FETs (MESFETs) [10, 11].

Besides these listed devices, efforts are also oriented on junction FETs (JFETs), FinFETs, and bipolar devices such as Schottky-pn, pin diodes or bipolar junction transistors (BJTs) [12, 13, 14, 15, 16]. Despite the important and promising recent improvement reported, a lot of work still has to be done such as on wafer size, crystal quality, ion implantation, high resistivity of the n-type diamond layer, fabrication process, diamond parameter extraction, and device design to take full advantage of diamond material [17]. For the design, one needs to properly terminate the edge of the electrode at the surface to avoid premature breakdown of the devices due to electric field crowding at the borders. For that, a technique called edge termination (ET) is used to push the limit of the devices.

The purpose of this thesis is to use the strength of the edge termination to extract impact ionization coefficients which are intrinsic diamond parameters that can be used to predict the blocking capability of diamond-based devices. The primary target was to develop an optimized structure to extract the impact ionization coefficients intrinsic parameters of diamond in an accurate manner by suppressing electric field crowding effect, and at the same time to evaluate the extracted impact ionization coefficients by comparing the experimentally and simulated results for field effect transistors.
I managed my time to explore two edge terminations for Schottky barrier diode called field plate (FP) oxide and floating metal guard ring (FMGR) (or floating field ring - FFR) where the efficiency of the guard ring integration on electric field distribution was observed [18]. Besides, two different normally-on FETs were fabricated, a MESFET and a reverse blocking (RB)-MESFET. The RB-MESFET distinguishes from the MESFET by its drain contact that is Schottky contact instead of Ohmic. It provides a bi-directional switch that improves the on-state power losses and is used in matrix converters and push even more the capacity of a MESFET. The development of transistors is inseparable from the Schottky diode since both are required to fabricate commutation cells.

Chapter 1

The road to diamond power devices

1.1 Power electronics devices

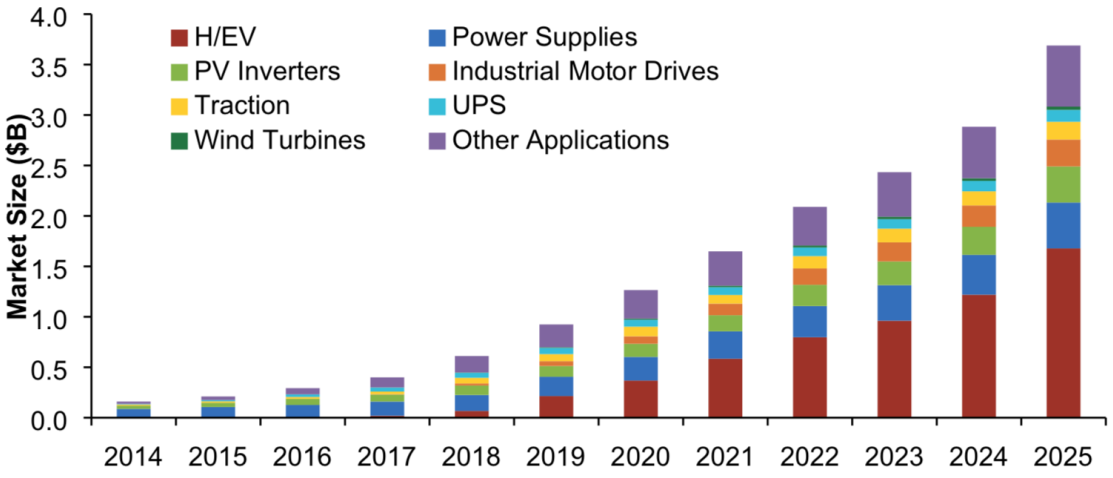

Figure 1.1: Prediction of wide bandgap market size by potential application [19]

Power electronics plays a fundamental role in our modern life. The constant need for electricity implies an increase in energy production. From transmission to distribution, power devices answer to this condition to convert high power energy to medium or low power. And hence, one of the essential tasks is to switch the power from the on-state to the off-state (and vice versa). A power device needs to be able to transport high currents in the on-state with as lower as possible on-resistance (voltage drop). And to withstand high voltages in the off-state. Nowadays, silicon (Si)-based devices are mainly used, silicon carbide SiC and gallium nitride GaN start to be integrated. Si material sees its physical limit reached. The growing energy demand and efficiency allowed an investigation of wide bandgap (WBG) materials. Thanks to their high bandgap and better dielectric strength, WBD materials can improve the efficiency and reduce the size of the devices. Potential application areas of WBG power electronics are presented in figure 1.1. A broad application range is predicted for the next seven years such as industrial motor drives (e.g., variable frequency or speed drive - VFD or VSD), photovoltaics (PV) inverters, power supplies and hybrid and electric vehicles (H/EV). At present, power supplies are the major WBG market provided by SiC Schottky barrier diodes. Soon, H/EV market is expected to become more massive than the one of the power supply. All these predictions are based upon the global warming alert that forces the modern city to adapt its energy production and efficiency use. In June 2015, the first railcar traction inverter using only SiC power devices in Tokyo was reported by Mitsubishi Electric's achieving 40% power saving [20] and GaN will be soon available such as GaN on Si. The actual drag of full integration is due to a delayed predicted price drop which is related to the wafer size. Among the interesting WBG semiconductors materials, laboratories are now focusing on gallium oxide Ga_2O_3 because of the easiness of growing the material with large area size. However, diamond is not considered to be a WBG material but within the ultra WBG (UWBG) materials owing to its outstanding physical properties which are discussed and compared to other WBG.

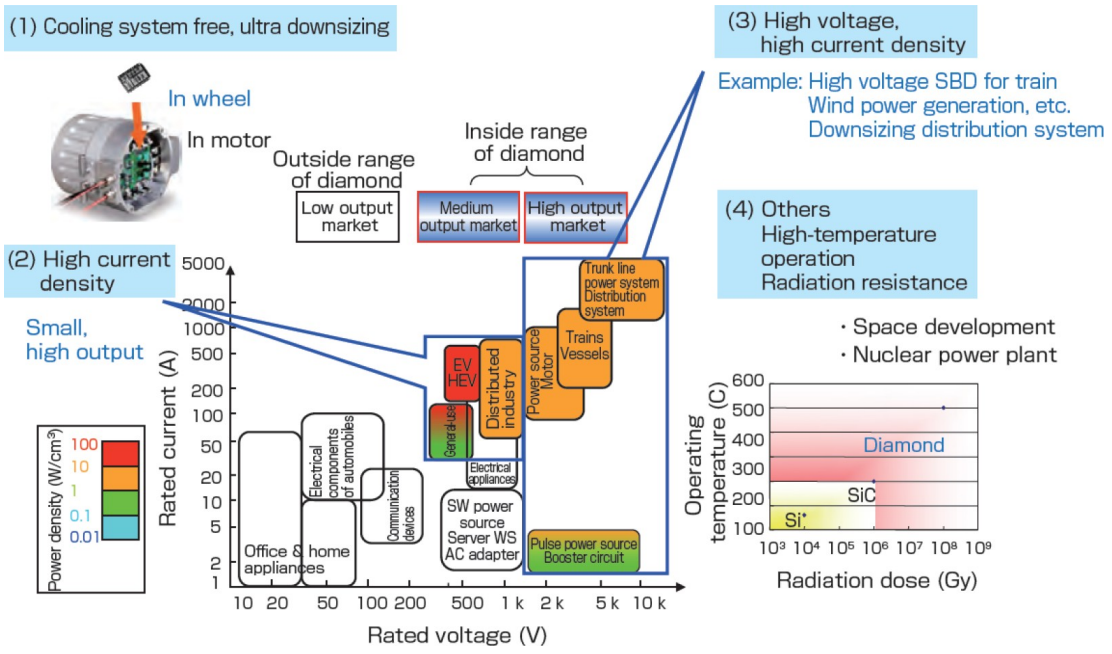

Figure 1.2: Prospective applications of diamond power devices. [21]

1.2 Wide bandgap semiconductors

Figure 1.2 shows the prospects of diamond power devices. WBG semiconductors are seen to be the answer for high power handling and high operating frequency. Diamond can be promising for medium and high output market, it is investigated as a potential candidate for space development and nuclear power plant. There are opportunities for WBG materials and especially diamond to explore what Si material cannot reach.
The main physical properties of WBG (SiC & GaN) and UWBG (β-Ga_2O_3 & Diamond) semiconductors that may replace Si for power electronics are enclosed in table 1.1. In fact, due to a low cost of using Si as semiconductor, there is no interest in replacing Si by another WBG material for low power applications. SiC, GaN, β-Ga_2O_3 have better dielectric strength than Si. SiC surpass Si for the thermal conductivity. Recently, the first transistor with interesting properties using β-Ga_2O_3 was reported [22]. This encouraged the community to strengthen the possible use of the material for power electronics. The extremely low thermal conductivity (0.1 to 0.2 W/cm.K) can limit the integration of the material. To overcome this issue new architecture, as well as device environment, needs to be adapted. A combination of two semiconducting materials may be one solution. Diamond, with its incredible physical properties, is seen as the ultimate and most suitable semiconductor for power electronics devices. Its critical field ($\geq$ 10 MV/cm) is about 30 times than that of Si. It is common to compare the WBG semiconductors through the Baliga's figure of merit (BFOM) for power electronics application. BFOM defines the best material characteristics to reach the lowest conduction losses and is given by,

$$BFOM = E_s.\mu.E_c^3 \tag{1.1}$$

Another illustration to compare the different semiconductor is done for a fixed reverse voltage of 1 kV and an area of 1 cm^2, but first, some basic equations are reminded. Let's

Property	Symbol [Unit]	Si	4H-SiC	GaN	β-Ga_2O_3	Diamond
Band gap	E_G [eV]	1.1 *i*	3.23 *i*	3.45 *d*	4.5 *i*	5.45 *i*
Dielectric constant	E_s	11.8	9.8	8.9	10	5.5
Critical field	E_c [MV/cm]	0.3	2	3 - 4	6.5 - 8	$\geq$ 10
Thermal conductivity	λ [W/cm.K]	1.5	5	1.5	0.1 - 0.2	22
Electron (e^-) mobility	μ_e [cm^2/V.s]	1500	1000	1250	200	1000
Hole (h^+) mobility	μ_h [cm^2/V.s]	480	100	200	-	2000
(e^-) Sat. drift velocity	v_s [10^7 cm/s]	1	2	2.2	-	2.7
(h^+) Sat. drift velocity	v_s [10^7 cm/s]	1	-	-	-	1.1
Baliga's FOM	BFOM [Si = 1]	1	165	635	1231	23017

Table 1.1: Main physical properties of wide bandgap (WBG) and ultra WBG semiconductors compared to Si for power electronics. Corresponding BFOMs were added. *i* and *d* stand for indirect and direct gap, respectively. BFOM, *Baliga's figure of merit*.

consider a one-dimensional non-punch-through (NPT) diode with a p-type drift layer. The specific on-resistance can be expressed as

$$R_{on}S = \frac{W_D}{q\mu_p N_A} \tag{1.2}$$

where W_D is the drift layer thickness, N_A the acceptor concentration, μ_p the hole mobility, and q the elementary charge. The BV is obtained by integrating the electric field along the depletion region:

$$BV = \frac{W_D E_m}{2} \tag{1.3}$$

From the expression of the electric field related to the doping concentration and the depletion region:

$$E_m = \frac{qN_A W_D}{E_s E_0} \tag{1.4}$$

By combining equation 1.3 and 1.4, the doping concentration can be expressed as,

$$N_A = \frac{E_s E_0 E_m^2}{2qBV} \tag{1.5}$$

Expression 1.2 can, therefore, be also written as

$$R_{on}S = \frac{4BV^2}{\mu_p E_s E_0 E_m^3} \tag{1.6}$$

From this equation, for a given BV of 1 kV and an area of 1 cm^2, the following comparison between the different material for drift layer thickness required and on-resistance of the diode are summarized in the table 1.2.

	Unit	Si	4H-SiC	GaN	β-Ga_2O_3	Diamond
W_D	μm	67	6.7	10	2.5	2
R_{on}	$m\Omega$	94	0.17	0.5	0.03	0.0004

Table 1.2: Comparison of different semiconductor material used to fabricate a 1-kV diode with 1 cm^2 area.

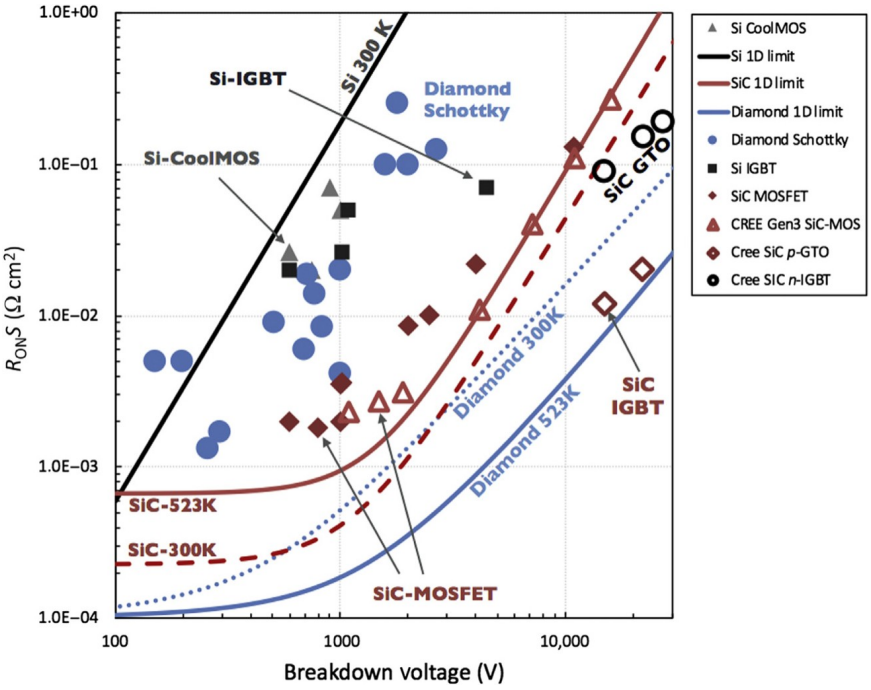

Figure 1.3: Specific on-resistance ($R_{on}S$) as a function of breakdown voltage (BV). Solid lines are 1D theoretical limits for Si (300 K), SiC (523 K) and diamond (523 K) extracted from [23]. Symbols are experimental data. Only Schottky diodes are represented for diamond - courtesy to E. Gheeraert [24].

It is seen in this table that thanks to a higher critical field, wide bandgap materials and especially diamond require thinner drift layer and hence lower on-resistance are achievable.

From a punch-through (PT) diode structure, and taking into account the incomplete ionization, the acceptor concentration dependence of the ionization energy, Umezawa *et al.* [23] reported the relationship between specific on-resistance $R_{on}S$ and BV. The one-dimensional limit for diamond was realized as seen in figure 1.3 [24]. Diamond has the best trade-off between specific on-resistance and breakdown voltage. It performances improve when increasing the temperature due to incomplete ionization of impurities. Oppositely, SiC characteristics degrade when the temperature rises. Experimental diamond reported data are from only Schottky diodes and are far from the theoretical limit. If a particular architecture such as edge termination structure is used, a theoretical 1D boundary can be crossed as presented for Si and SiC with Si insulated-gate bipolar transistor or SiC gate turn-off thyristor, respectively.

1.3 Diamond devices background

1.3.1 Diamond Schottky diodes

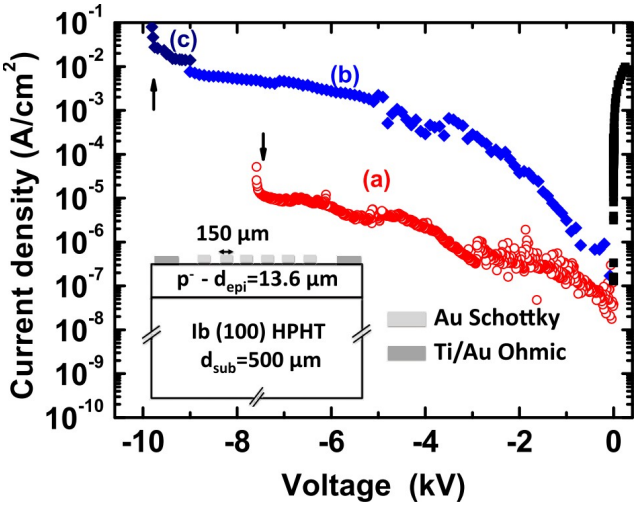

Figure 1.4: High breakdown field on a p-type Schottky diode. A schematic cross section of the fabricated sample is shown [25].

Diamond bipolar and unipolar diodes exhibiting interesting forward and reverse characteristics have been reported. Bipolar diode was investigated through p-type-intrinsic-n-type (*pin*) diodes by several groups [26, 27, 28, 15]. However, as stipulated in the thesis title, a background of only unipolar devices will be given. Schottky barrier diodes (SBDs) have already proven remarkable features in both the on-state and the off-state [29, 30, 25, 31, 3]. P. N. Volpe *et al.* reported a lateral Schottky diode with a high breakdown field of 7.7 MV/cm corresponding to 9.7 kV [31]. The structure, as well as the electrical characterization, are shown in figure 1.4. The active layer was oxygen-terminated surface and has a doping level of 10^{16} cm^{-3} and a thickness of 13.6 μm. The experimentally obtained breakdown field is close to the expected value for diamond. It is much larger than the Si or SiC critical field; however, the on-state was compromised. Another Schottky barrier diode that also exhibited a high breakdown field was reported by A. Traore *et al.* [3]. A punch-through O-terminated pseudo-vertical Schottky diode was used. The breakdown voltage was 1 kV for a maximum electric field of 7.7 MV/cm. The on-state characteristics were also interesting with a high current about 3000 $A.cm^{-2}$. A post-annealing treatment exhibited a formation of a thin layer of zirconium oxide ZrO_2, lowering the Schottky barrier height (SBH), and hence, shifting the threshold voltage to nearly 0 V, as seen in figure 1.5. Further works on diamond Schottky barrier diodes with important results were also reported [30, 32].

In addition, Schottky m-i-p^+ diodes were reported with a high breakdown voltage of about 2.5 kV (4.2 MV/cm) [33] and a maximum current density of 7.5 kA/cm^2 [34]. Another unipolar diode used with a fully depleted thin n-type layer in contact with the Schottky electrode is the diamond Schottky-pn diode (SPND) [35, 14]. It was investigated for both phosphorus P-doped thin layer [36] and lightly nitrogen N-doped layer [37]. The highest current density of 60 kA/cm^2 was obtained for the lightly P-doped layer. In both cases, the breakdown field was 3.4 MV/cm. This kind of unipolar diode had exhibited no trade-

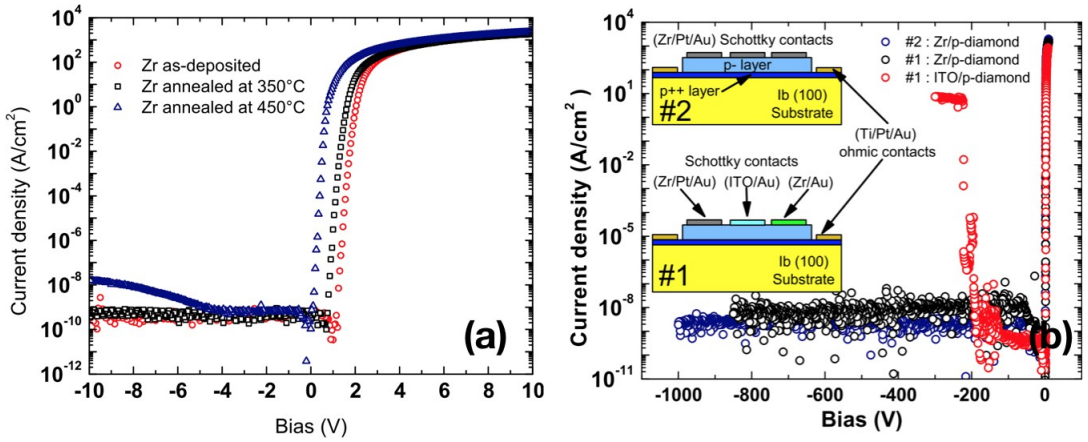

Figure 1.5: (a) Post-fabrication annealing influence on the forward characteristics and (b) high breakdown voltage of 1 kV (7.7 MV/cm) obtained in off-state at 300 K. A cross-sectional view is given. At high temperature, the Zr/oxidized diamond forms a thin oxide layer [3].

off between on-resistance R_{on} and breakdown voltage. All the characteristics recalled above were obtained on unterminated structure diodes. Even without edge termination architectures, Schottky diodes have demonstrated extremely high breakdown fields. If an edge termination is added, one can expect higher breakdown fields. In the following section, an introduction of edge termination techniques of diamond devices and important investigation will be shown.

1.3.2 Edge termination structures

For high blocking voltage devices, it is essential and crucial to optimize the device structure by the use of edge termination technique. For a merely structured diode, breakdown voltage (and thus breakdown field) is well below the ideal limit due to a field crowding at the edges that cause a premature breakdown, as it was reported on SiC or GaN [38, 39]. Figure 1.6 summarizes some typical edge termination structures.

Mesa structure (figure 1.6-A) suppress the crowding field at the n^+/p^- edge by avoiding the lateral depletion. This technique is widely used for Si and SiC with results close to the ideal case [41]. Mesa technique is not well adapted for SBDs since the peak electric field is at the edge of the metal contact. Therefore, other edge termination techniques were investigated to overcome this problem as shown in figure 1.6. SiC and GaN have already reported SBDs using field plate (FP) structure [42, 43] before been investigated for diamond SBDs by simulation [44, 45] and experience [46, 47]. The electric field at the edge of the main Schottky contact is relaxed thanks to electrical line forces formed between the metal and the ionized acceptors through the oxide. Two parameters in FP structure can be optimized, the oxide thickness and the FP length L_{FP}. K. Ikeda *et al.* have reported on the importance of a high-k material such as aluminum oxide Al_2O_3 to decrease the electric field peak at the edge. Indeed, due to the O-terminated diamond surface that implies a positive electron affinity (EA), almost only Al_2O_3 has a large band offset to avoid holes and electrons from tunneling through the oxide. H. Umezawa *et al.* reported that the sensitivity of the field oxide thickness was more important than the

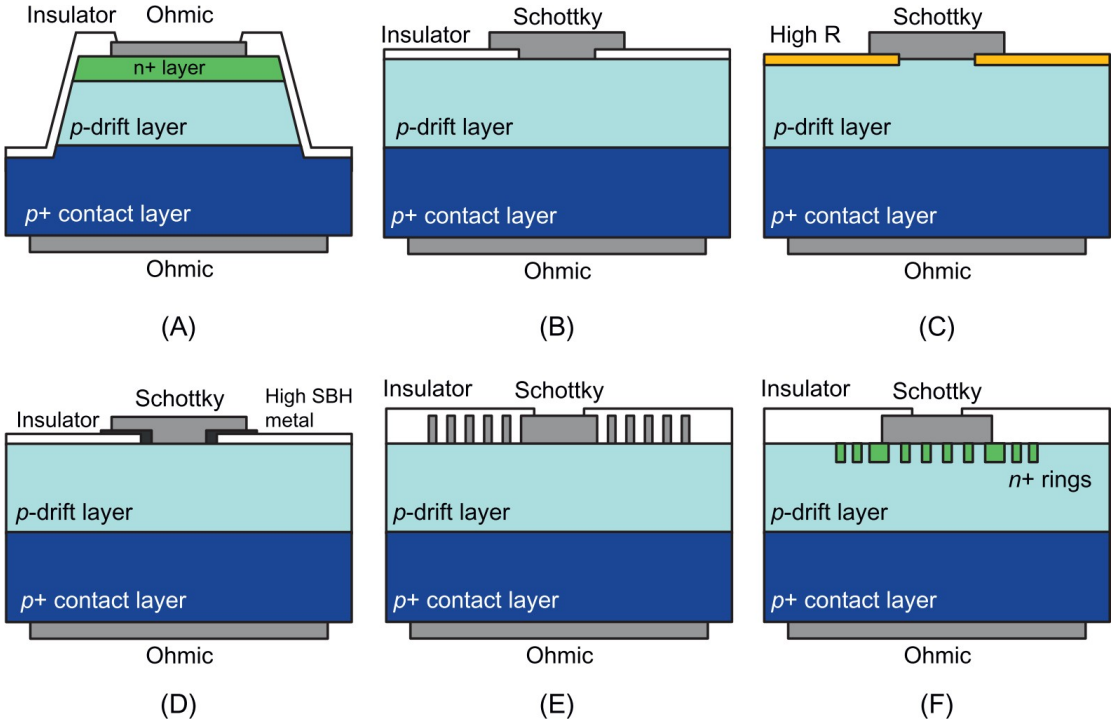

Figure 1.6: Schematic cross-sectional views of different edge terminated diamond diodes. Named as: (A) mesa, (B) field-plate, (C) surface passivation, (D) double Schottky metal, (E) floating metal rings and (F) JBS with JTE. *JBS*, junction barrier Schottky. *JTE*, junction termination extension — courtesy to H. Umezawa [40].

influence of the field plate length L_{FP} [40]. An optimized L_{FP} varies from 5 to 10 μm for an entire doping range of power device. A cross-sectional and a top view of the fabricated FP-SBDs reported in [47] are shown in figure 1.7. An O-terminated thick drift layer was used, and a field oxide of 0.2 μm thickness was deposited on a vertical SBD. The reverse electrical characterization is also shown in figure 1.7. The estimated maximum electric field for an unterminated SBD is 0.8 MV/cm. However, when a field plate with small L_{FP} is used the utmost electric field is doubled and reach 1.8 MV/cm. The limitation of the maximum electric field could be due to several parameters such as the propagating dislocation from the heavily boron doped diamond substrate, a non-optimized field oxide thickness or also an oxide roughness at the edges.

Another edge termination structure, in the same framework as the FP technique, is the ramp oxide FP. By creating a Bevel oxide shape at the edges (gradual thickness increase), one hot point is suppressed leading to a 90% achievable ideal device breakdown considering a high-k material [48]. This structure has never been investigated experimentally yet. S. Rugen from the university of Bremen (Germany) also studied floating metal rings structure (figure 1.6-E) effectiveness [49]. Influence of the ring spacing and number were reported. Further details will be given in chapter 4. This kind of ET technique is also widely used for SiC and GaN semiconducting material where a number of rings and spacing between the rings and rings width are optimized [50, 51, 52]. With the technology improvement, the guard ring in SiC devices uses implanted heavily doped regions (figure 1.6-F). Ion implantation is not a mature technology for diamond material so far.
It is known that a power device needs edge termination structures to reach characteristics

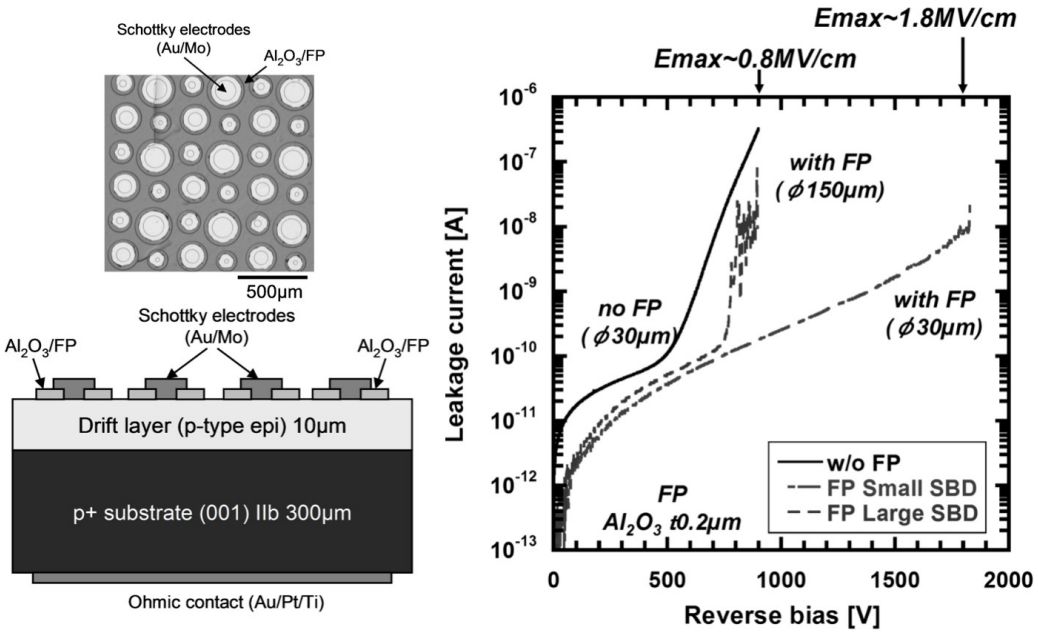

Figure 1.7: Current-Voltage characteristics of diamond SBDs with and without field plates. A cross-sectional and a top view are also presented. [47].

near-ideal case. At present, few edge termination structures were investigated experimentally. Further, structures have to be explored for diamond to take advantage of full diamond field strength. And only after parameters such as impact ionization coefficients which are field dependent, can be measured accurately.
The work realized on SBDs can also be integrated for transistors fabrication which the premature breakdown occurs for the same reasons (peak electric field at the gate edge).

1.3.3 Diamond unipolar field effect transistors

H-terminated or O-terminated diamond surface can be used to fabricate field effect transistors (FETs). The first one leads to a surface channel conduction via two-dimensional hole gas (2DHG), and the second leads to bulk channel conduction due to the oxidization. Both of them are investigated for diamond.
Three modes are referenced for transistors; the depletion mode corresponding to a regular switch-off of the transistor by forming a space charge region (SCR) under the gate and the deep depletion mode which is available only for MOSFETs, because of the high doping level of the channel that may induces gate leakage current in case of MESFETs. An finally, the inversion mode transistor that forms a thin conducting layer of minority carrier within the channel. Recently, T. T. Pham *et al.* have reported that a time constant for minority carrier generation about 10^{30} years is required to switch from the deep depletion regime to a strong inversion regime, which is impossible [8]. This very long time constant for minority carrier generation is related to an exponential dependence of the bandgap.

1.3.3.1 Depletion mode transistor

The depletion mode transistor is a normally-on device. It requires a reverse voltage to be applied to the gate for channel modulation and transistor switch-off. Bulk channel or surface channel conduction are the two main types.

Bulk channel FET

Despite the difficulties encountered to grow a good n-type layer, junction FETs (JFETs) using diamond were successfully fabricated and characterized [53]. Figure 1.8 presents a schematic section and a top view of the diamond lateral JFET reported by T. Iwasaki *et al.* [54, 55]. At present, normally-on and normally-off JFETs were realized [12]. A maxi- mum current density of 450 A/cm^2 was achieved at a high temperature of 573 K, and the transistor was normally-off [56]. A maximum blocking voltage of 600 V (6 MV/cm) was obtained for different device parameters and a temperature of 200 °C [57]. The maximum breakdown field obtained is here also more significant than the physical limits of 4H-SiC and GaN. The temperature operation facilitates the activation of the n^+ layer. Vertical type JFET is challenged to realize, but it is under investigation.

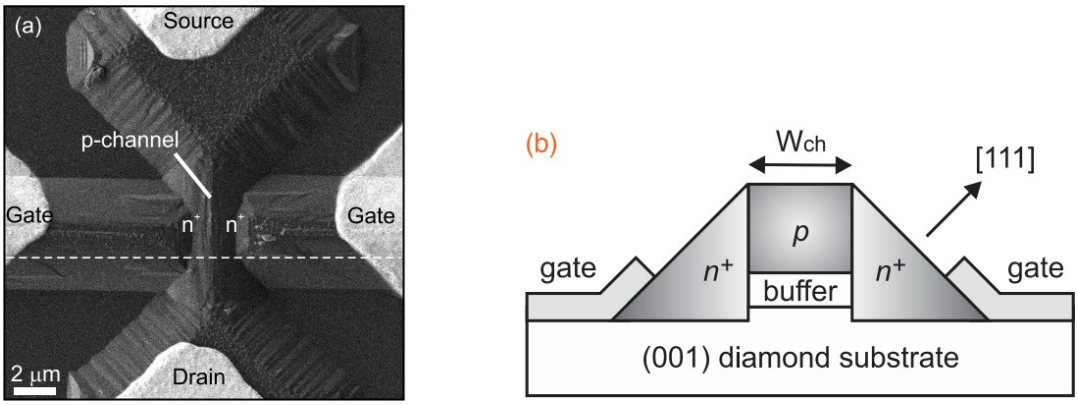

Figure 1.8: (a) Top view and (b) cross-sectional view of the junction field effect transistor with lateral pn junction [54].

Metal-semiconductor FETs (MESFETs), following the similar physics than JFETs, were also investigated through surface channel conduction for high-frequency applications [58, 59, 10] and bulk channel conduction [11]. The bulk conduction is more suitable for high power switching transistor. Background and more details will be given in chapter 4.

Surface channel FET

Surface channel conduction is widely used for diamond MOSFET. In fact, only depletion mode is achievable when a diamond surface is H-terminated. As the diamond EA is negative, considering the band alignment, a barrier will be formed for holes and not for electrons. Many works on H-terminated MOSFET were reported [60, 61, 62]. Surface channel MOSFET are transistors that have exhibited higher current densities and lower on-resistances as compared to bulk channel conduction FETs. The maximum drain current density reached 1.3 A/mm [63]. Lastly, vertical-type 2DHG MOSFET was realized [64]. Figure 1.9 shows the on-state characteristics of a vertical 2DHG MOSFET. The current density exceeds the 200 mA/mm, and the corresponding breakdown voltage was about 350 V. Figure 1.9-(b) highlight the weakness of using an H-terminated surface.

Even if the oxide stabilizes, the thin H-layer formed, increasing the temperature degrades the transistor characteristics. And hence, the H-terminated MOSFET cannot be used for temperatures higher than 200°C. A normally-off behavior was reported for a planar H-terminated diamond MOSFET by partially terminated the channel by oxygen [6]. The highest breakdown voltage realized for this structure was about 2 kV, but the maximum drain current density decreased by about two orders of magnitude as compared to the vertical-type. A trade-off on-resistance and breakdown voltage are here observable.

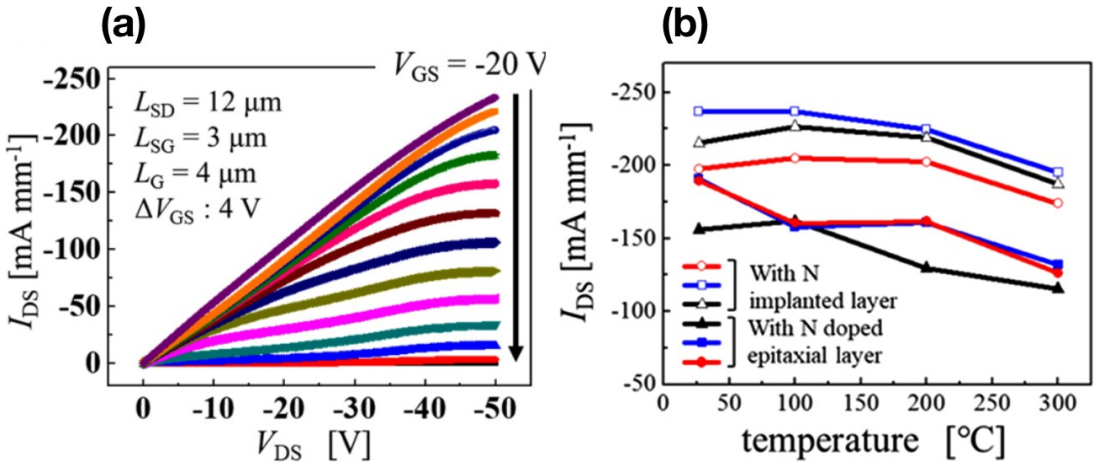

Figure 1.9: (a) On-state characteristics of vertical-type 2DHG MOSFET and (b) temperature influence of the maximum drain current density [64].

1.3.3.2 Deep depletion mode transistor

One of the last reported work on unipolar bulk conduction MOSFET, was realized by T. T. Pham *et al.* The first achieved and observed deep depletion mode of a transistor. Basically, the deep depletion is a regime observed just before a strong inversion occurs. However, as explained earlier, the inversion regime does not take place naturally because of the ultra-wide bandgap of diamond. The deep depletion allows higher channel doping (in the range of 10^{16} to 10^{17} cm^{-3}) as compared to a bulk conduction MESFET. For the same doping level, a MESFET will see its gate leakage current importantly high with incapacity to close the channel. The high doping level improves (decreases) the on-resistance and (increase) the maximum drain current. A conceptual cross-sectional view and an SEM picture of the fabrication MOSFET are shown in figure 1.10-(a). As a counterpart, the breakdown voltage is low and reported to be about 200 V. This fabricated and reported device had a poor maximum drain current density because the Ohmic source and drain were directly deposited on the active layer. A heavily doped layer beneath the source and drain can further improve the characteristics.

1.3.3.3 Inversion mode transistor

To overcome the issue of inversion regime obtention in diamond MOSFETs, Matsumoto *et al.* have developed a structure that provides the minority carrier to under the gate. Figure 1.11-(a) and (b) show the cross-section of the structure as well as a picture of

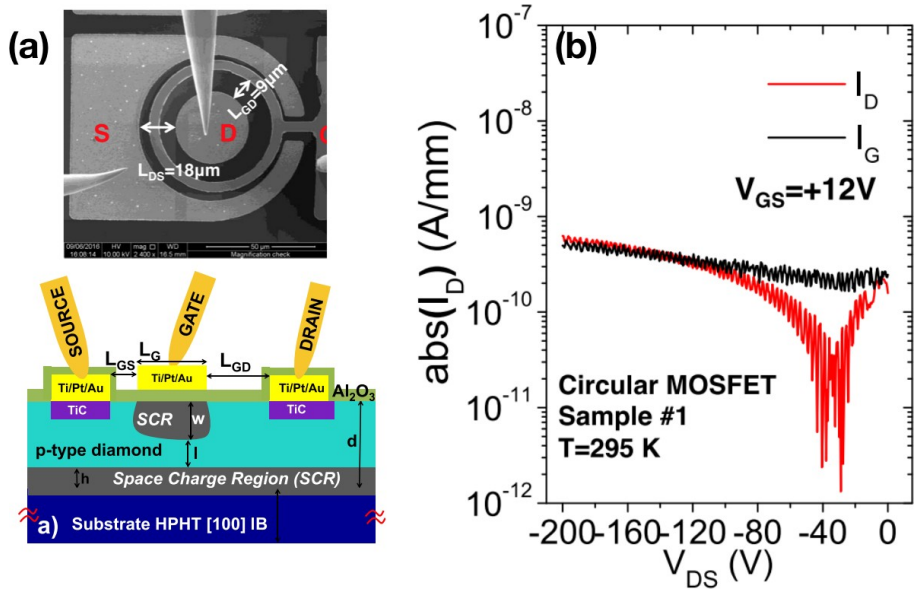

Figure 1.10: (a) Schematic cross view and SEM picture of the fabricated O-MOSFET. (b) Off-state characteristics. The transistor exhibited up to 200 V of breakdown voltage [65].

the fabricated MOSFET. An n-type channel was used, and a heavily doped boron p^+ selectively grown layer under the source and drain electrodes were added. The heavily doped boron layers are hole tanks that bring the missing minority carriers needed to form the inversion layer. Device electrical characteristics at the on-state are given in figure 1.11-(c). The transistor was normally-off, and a maximum drain current density of -1.6 mA/mm was obtained. Nonetheless, the reported field effect mobility was 8 $cm^2/V.s$ which is very low as compared to diamond measured value by Hall effect [66]. The breakdown voltage was not discussed, but an extremely low breakdown is expected.

1.4 Conclusion

In this first chapter, the increasing demand for better device performances and the warning of global warming brought the research to explore new semiconducting materials for high power applications. Diamond one of the recognized ultra wide bandgap material had demonstrated its capacity to be used for the future next-generation of power devices after maturity. Its exceptional physical properties give opportunities in a wide range of applications. Simple lateral and pseudo vertical Schottky barrier diodes have exhibited a maximum electric field (7.7 MV/cm) close to the commonly known one (10 MV/cm). However, due to an critical amount of dislocations within the heavily doped boron substrate that induce leakages, it is difficult to achieve the same maximum electric field. Fortunately, the quality of the bulk, as well as the epitaxial layer, are now under investigation.

Edge termination technique is essential for high power devices. Unfortunately, a few experimental studies were reported, and it was using field plate structure. Further structures need to be explored to reach the ideal breakdown voltage. Important FETs were also reported as it was seen in this chapter; however, the breakdown field remains low as compared

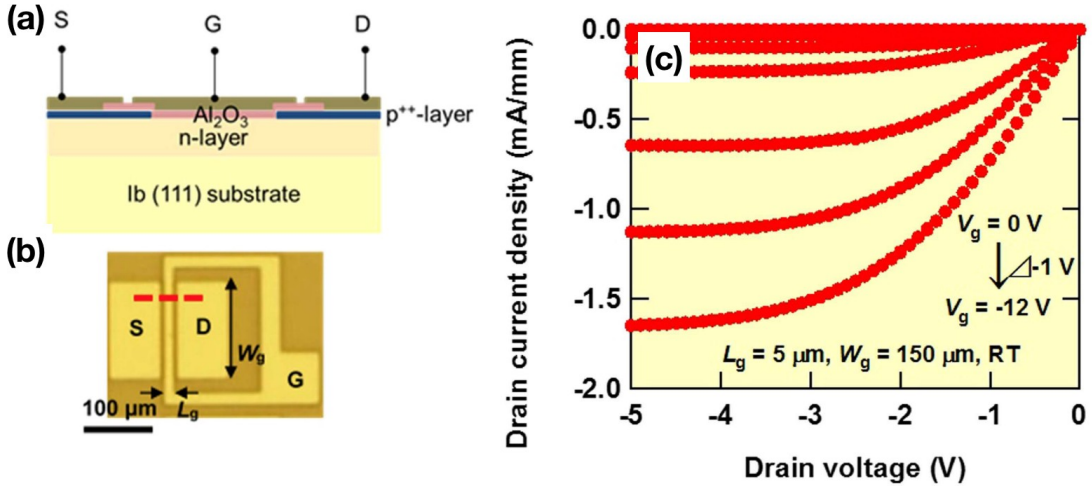

Figure 1.11: (a) Cross-sectional view and (b) top view picture of the inversion mode MOSFET. (c) On-state state characteristics [9].

to the theoretical expectation of diamond. For a good understanding of the breakdown characteristics of a device, it is crucial to know the impact ionization coefficients as a function of the electric field. The extraction of accurate parameters requires a device with characteristics near the ideal ones. It was already shown for power devices using SiC or GaN that only edge termination technique can bring to that level. Chapter 5 is dedicated to the impact ionization coefficients from the background to the measurement.

Chapter 2

Unipolar devices theory and simulation's model

Unipolar power devices are mainly used and preferred in power devices as compared to bipolar devices. A unipolar device uses conduction of majority carrier (either electrons or holes) which make it a suitable device for fast switching from the on-state to the off-state. Indeed, during the on-state operation of a bipolar power device, injection of mi- nority carriers occurs. These minority carriers must be removed when the device switches from the on-state to the off-state. The processes to remove the minority carriers (such as electron-hole recombination process) induces significant power losses, and this makes unipolar devices more suitable for low power losses.
In this chapter, the theory behind the unipolar devices and implemented simulation models will be presented. Two unipolar devices have attracted the attention, the rectifier Schottky diode and the switch metal-semiconductor field effect transistor (MESFET). Among the unipolar power transistors, metal-oxide-semiconductor field effect transistor (MOSFET) have gain popularity due to their normally-off behavior and the possibility to apply a forward bias on the gate to reach the accumulation without any leakage current. However, a MESFET has the advantage of taking rid of problems due to the oxide/semiconductor interface (one of the critical issues in MOSFET) such as interface traps or reliability is- sues. The MESFET offers a better control in defining short channel lengths for high-speed applications [10, 67] and its low gate resistance and low voltage drop is of great importance in microwave performance. The capacity of a MOSFET to use high doping channel layer to reach low on-state losses is also its weakness regarding off-state losses where the MESFET is more suitable for high breakdown and power capability.

2.1 Schottky diode

Compared to other diamond devices, Schottky diode is a promising power device since several groups have already reported high breakdown voltages [68, 29, 31, 30, 3]. Figure 2.1-(a) represents the general transfer characteristics of the ideal power devices. Due to the power dissipation issue, power devices (Schottky rectifiers) are not used in a linear regime, and hence two states are used:

- The off-state where $I = 0$ & $V \neq 0$
- The on-state where $I \neq 0$ & $V = 0$

In a real diode, figure 2.1-(b), the power dissipation is critical in the on-state due to the presence of a voltage drop originated from a threshold V_{TH} and a series resistance R_{on}. But it is also critical in the off-state when the leakage current starts to increase for high voltages. In most cases, this off-sate power dissipation ends by a breakdown voltage. The maximum BV that a device can withstand is limited by the material breakdown field [24].

2.1.1 Schottky contact

An Ohmic contact distinguishes from a Schottky contact (rectifier) by the difference of work functions between the metal φ_m and the semiconductor φ_s. Figure 2.2 shows the band structure of a metal and a p-type semiconductor electrically isolated system. At thermal equilibrium, when the metal and semiconductor are in intimate contact, the Fermi levels forces to align giving rise to a built-in potential barrier $V_0 = V_{bi}$ and a semiconductor band bending. When the metal work function is lower than that of the semiconductor,

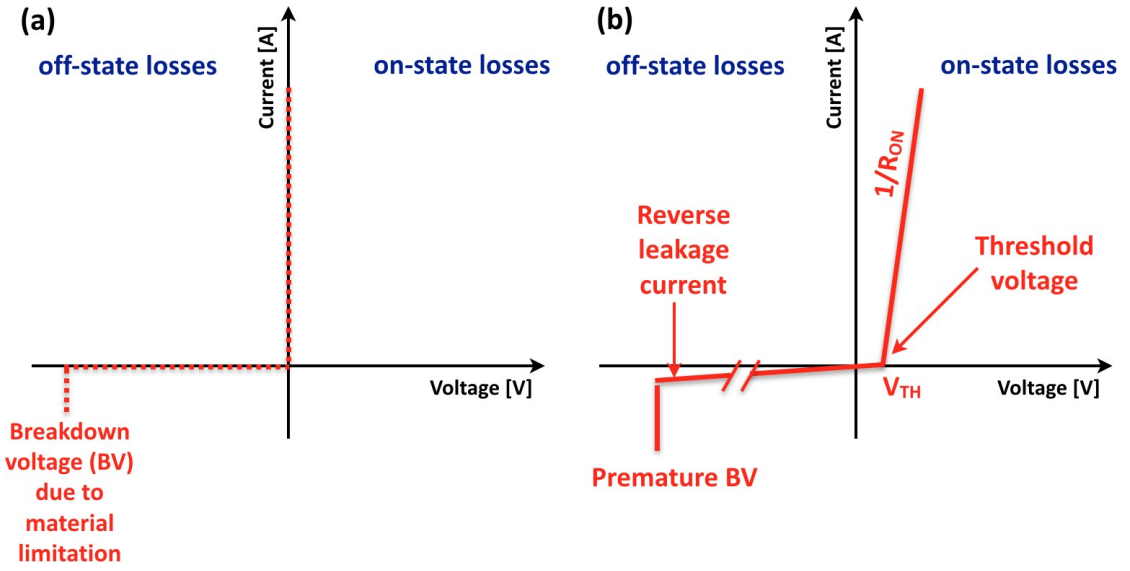

Figure 2.1: (a) Ideal characteristics of a diode. No current flowing in the off-state and no on-state voltage drop. (b) A typical representation of real characteristics of a diode. The device is limited by a breakdown voltage at the off-state and the voltage drop induces on-state losses in the forward region.

the band will be downward bent blocking the free holes to reach the metal side. The built-in potential formed can be approximated as follow $qV_{bi} \approx \varphi_{SBH} - E_a$, where E_a is the acceptors' ionization energy and φ_{SBH} is the Schottky barrier height in eV. The ideal Schottky barrier height (SBH) is defined by the Mott equation:

$$\varphi_{SBH} = E_g/q - (\varphi_m - X_s) \tag{2.1}$$

where X_s is the electron affinity (EA) of the semiconductor, E_g the band gap energy of the semiconductor and q the elementary charge. Under forward bias, V_0 is lower, which promotes carrier injection from the semiconductor into metal. However, if a reverse bias is applied the barrier V_0 increases further causing a band bending increase and pushing away the free holes blocked by the barrier. A depletion region formed at equilibrium when no bias is applied due to Schottky-Mott theory, extend from the Schottky electrode. The depletion width W represents the depletion region. Within this depletion region (or space charge region - SCR) free holes do not exist, only fixed ionized acceptors are present (Figure 2.2). The depletion layer width W_D which is bias dependent can be expressed, under the abrupt approximation by,

$$W_D = \sqrt{\frac{2E_0E_s}{qN_A}\left(V_{bi} + V_a - \frac{k_BT}{q}\right)} \tag{2.2}$$

The metal/semiconductor contact is rarely ideal because of interface defects which reduce the contact quality. One effect known in Schottky diode is the barrier lowering effect or Schottky effect). When a reverse bias is applied, equipotentials are created parallel to the Schottky electrode. The presence of equipotentials give rise to electric field at the metal/semiconductor interface considering a Columbic interaction (force of attraction)

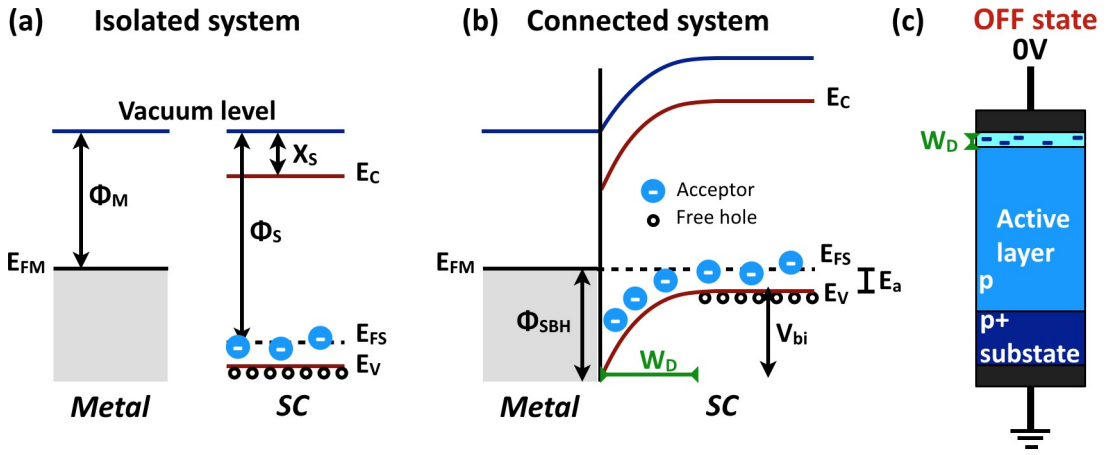

Figure 2.2: Schematic band diagram of built-in potential creation on Schottky contact for (a) an isolated system and (b) intimately connected system at equilibrium. (c) A one dimensional model of the Schottky diode at 0 V applied bias (reverse state). SC, *semiconductor*.

between a charge carrier located at a distance x in semiconductor and its mirror charge image charge at -x (an electron for a p-type semiconductor and *vice versa*) into metal [69]. This phenomenon affects the carrier injection by inducing a variation of the barrier $\Delta\varphi_{im}$ near the interface. An expression of barrier lowering due to Schottky effect is given by:

$$\Delta\varphi_{im} = \sqrt{\frac{qE_m}{4\pi E_0 E_s}} \tag{2.3}$$

Taking into consideration the image force barrier lowering, the Schottky barrier becomes:

$$\varphi_{SBH} = \varphi_{SBH0} - \sqrt{\frac{qE_m}{4\pi E_0 E_s}} \tag{2.4}$$

where φ_{SBH0} is the SBH without taking into account the image force lowering. E_m is the maximum electric field in the depletion region at the metal/semiconductor junction. The following equation can calculate it:

$$E_m = -\sqrt{\frac{2qN_A(V_{bi}+V_a)}{E_0 E_s}} \tag{2.5}$$

with N_A the acceptor doping concentration and V_a the applied bias. Even at zero bias the SBH undergo the image force lowering and hence the SBH at zero-bias φ^0_{SBH} can be approximated by

$$\varphi^0_{SBH} = \varphi_{SBH0} - \Delta\varphi^0_{im} \approx \varphi_{SBH0} - \left(\frac{2q^3 N_A V_{bi}}{(4\pi)^2 (E_0 E_s)^3}\right)^{1/4} \tag{2.6}$$

Andrews and Lepselter [70, 71] gave an empirical expression of the bias dependent SBH that includes the static dipoles [72] (a link between the electrode and the fixed ionized acceptors) under reverse bias V_r:

$$\varphi_{SBH}(V_r) = \varphi^0_{SBH} - \Delta\varphi_{im} - aE_m$$
$$= \varphi^0_{SBH} - \left(\frac{2q^3 N_A (V_{bi} + V_r)}{(4\pi)^2 (E_0 E_s)^3}\right)^{1/4} - a\left(\frac{2qN_A (V_{bi} + V_r)}{E_0 E_s}\right)^{1/2} \quad (2.7)$$

a is thought to be related to the density and depth of the interface state [71]. This bias dependence of SBH allows an enhancement of the reverse leakage current increase by degrading the barrier height.

The space charge region (SCR) formed beneath the Schottky junction depends strongly on the applied reverse bias. The capacitance C of a reverse-biased junction, when considering a uniform doping, can be expressed as follows:

$$C = \frac{E_0 E_s S}{W_D} \quad (2.8)$$

where E_0, E_s and S are the permittivity in vacuum, the permittivity in diamond and the device area, respectively. From the depletion width as a function of applied reverse bias expression 2.2 combined to equation 2.8, one can derive the following equation,

$$\frac{1}{C^2} = \frac{2}{qE_s A^2 [B]_{CV}} \left(V_{bi} - V - \frac{2kT}{q}\right) \quad (2.9)$$

In equation 2.9, V_{bi}, q, k, T and $[B]_{CV}$ are the built-in potential, the elementary charge, the Planck constant, the temperature, and the non-compensated acceptors' concentration (N_A - N_D), respectively. From C^{-2} vs V plotted curve, the slope of the linear part gives $[B]_{CV}$ and the extrapolation to $C^{-2}=0$ gives V_{bi}. An expression of the acceptor concentration extracted by C(V) is used,

$$[B]_{CV} = N_A - N_D = \frac{-2}{qE_s A^2} \frac{1}{d(1/C^2)/dV} \quad (2.10)$$

2.1.2 Reverse current

The reverse current of a Schottky diode can be explained by the thermionic emission (TE) mechanism. The Schottky effect induces a reverse current dependent on the bias following this equation:

$$I(V) = A^* S T^2 exp\left(-\frac{q(\varphi^0_{SBH} - \Delta\varphi_{im}(V) - aE_m(V))}{k_B T}\right) \quad (2.11)$$

where $V = V_{bi} + V_r$, S the diode section, k_B is the Boltzmann constant, T the lattice temperature and A^* the Richardson constant. When a high electric field is applied, TE

mechanism is not enough to explain the reverse current. The presence of the high electric field thermally excites the carriers close to the thinner part of the barrier potential and hence contributing in tunneling phenomena of the carriers referenced as thermionic field emission (TFE) mechanism. An estimation of the TFE reverse current is defined as

$$I(V) = \frac{2SA^*(q\pi TV)^{1/2}qE_{00}}{k_B^{3/2}} exp\ -\ \frac{q(\varphi_{SBH}^0 - \Delta\varphi_{im} - aE_m)}{k_BT} + \frac{q^3 V E_{00}^2}{3(k_BT)^3} \qquad (2.12)$$

The tunneling parameter E_{00} depends on doping concentration N_A and the carrier effective mass m^*, $E_{00} = 18.5 \times 10^{-3} \sqrt{(N_A/(5.7m^*))}$.

2.1.3 Forward current

Current transport of a Schottky diode is based on a nonlinear regime. Most of the reported diamond rectifiers have exhibited a forward current described by a TE mechanism. In that aim, only that mechanism will be introduced. Drift and diffusion model will not be exposed here; more information can be found in A. Traore thesis [73].
The forward current explained by TE mechanism can be expressed as follow:

$$I = I_s exp\ \frac{q(V - R \times I)}{nk_BT}\ \left[1 - exp\ -\frac{q(V - R \times I)}{k_BT}\right] \qquad (2.13)$$

where R is the bulk resistance, n the ideality factor that provides information on the metal/semiconductor interface quality (if n is close to unity, then the rectifier can be considered as ideal) and I_s the saturation current:

$$I_s = A^* S T^2 exp\ -\ \frac{q\varphi_{SBH}^0}{k_BT} \qquad (2.14)$$

2.2 Metal-semiconductor field effect transistors

Metal-semiconductor field effect transistor (MESFET) is a unipolar device that uses a majority carrier conducting channel positioned between a source and a drain contacts. Figure 2.3-a is a schematic structure of a p-type channel MESFET. Both source and drain are Ohmic contacts. When applying a negative bias V_D to the drain with respect to the source, holes flow from source to drain. The gate is a Schottky rectifier that modulates the thickness of the conducting channel (and hence the current between source and drain) thanks to the depletion region formed by the Schottky junction. If the depletion region allows a current flow when no bias on the gate is applied, then the MESFET is called normally-on transistor and works under the depletion mode process to turn off the device.

Typical current-voltage *I-V* characteristics of a MESFET is shown in figure 2.3-b, where the drain current as a function of drain voltage for different fixed gate voltages is plotted. The drain *I-V* characteristics can be divided into three regions [69]: The linear region

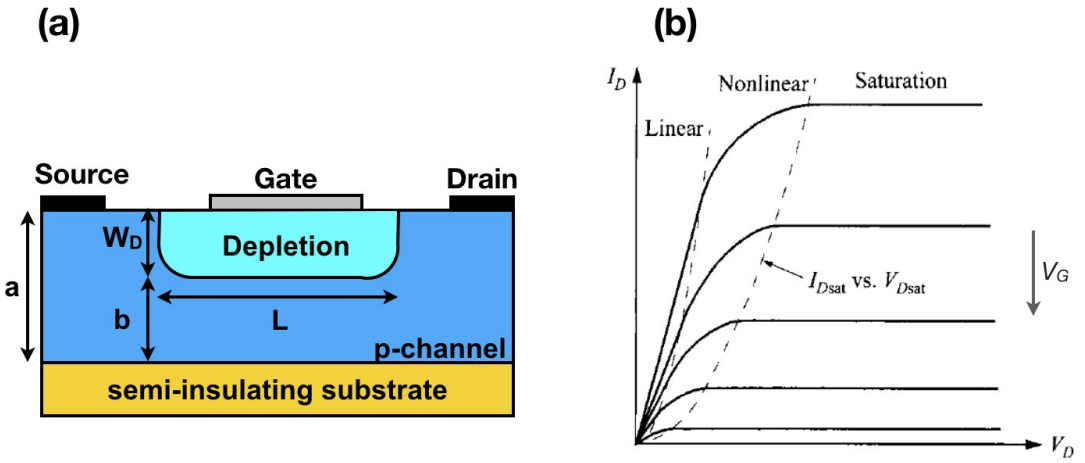

Figure 2.3: (a) Schematic cross-sectional structure of a p-type channel MESFET where the net channel opening is controlled by the depletion width W_D created by the gate Schottky junction. L is the channel (or gate) length, a is the channel depth, and b is the net channel opening. (b) General *I-V* characteristics of a p-type normally-on MESFET with the commonly observed three regions: Linear, Nonlinear and Saturation.

at small drain bias where the drain current I_D is proportional to the drain bias V_D; The nonlinear region, which encloses the pinch-off of the channel; and the saturation region where the current remains constant independently of V_D.

2.2.1 Space charge region

Additional to the space charge region (SCR) created by the gate Schottky contact, it also exists an SCR in the p-type diamond epilayer induced by the p-n junction at the substrate/epilayer interface. The substrate used to fabricate MESFETs is a semi-insulating diamond substrate with a high amount of nitrogen (N) assumed to be 3×10^{19} cm^{-3} [74]. The expected depletion width within the epilayer at the interface between the substrate and the epilayer can be calculated using:

$$W_{epi} = 2\sqrt{\frac{E_0 E_s k_B T}{2q^2 N_D} \frac{1}{(1+N_A/N_D)} ln\frac{N_A N_D}{n_i^2}} \tag{2.15}$$

where N_D is the nitrogen donor concentration in the substrate, N_A is the boron acceptor concentration in the epilayer, n_i is the intrinsic carriers concentration. Figure 2.4-a schematizes the two SCRs created in a MESFET. The SCR spreads in quasi-totality in the p-channel due to a high activation energy of nitrogen dopants. Using equation 2.15 and an assumed nitrogen concentration of 3×10^{19} cm^{-3}, under the condition that $N_A \ll N_D$, the extension of the SCR in the p-type diamond as a function of acceptors concentration is given in figure 2.4. It is expected that the SCR will influence the channel current due to a reduction of the net channel opening to an effective channel opening b'. The MESFET characteristics such as threshold voltage and on-resistance will also be influenced.

One of the interests of the threshold voltage which is a cause of the Schottky gate elec-

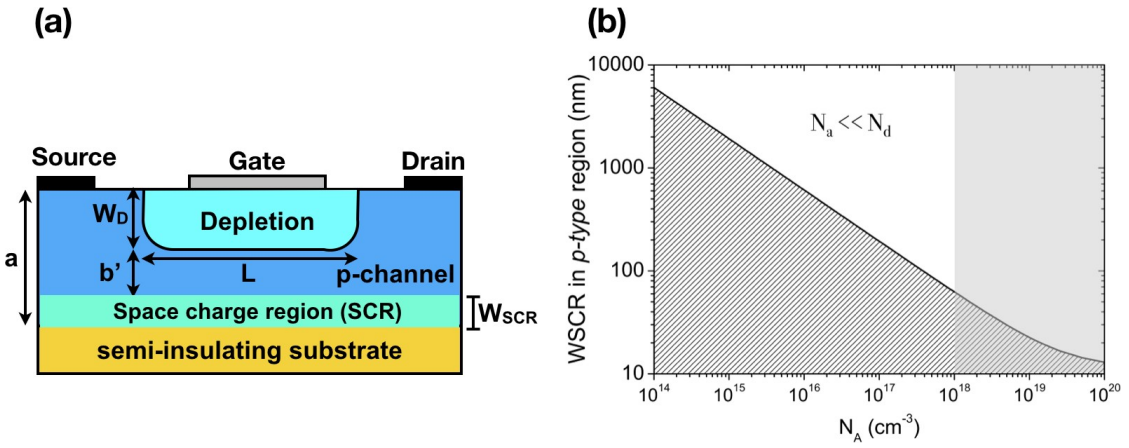

Figure 2.4: (a) Cross-sectional structure of a MESFET showing the space charge region (SCR) induced by the p-n junction at the substrate/epilayer interface. (b) Extension of the SCR in p-channel diamond due to p-n junction between the substrate and the epilayer as a function of boron acceptors concentration. Nitrogen concentration was assumed to be 3×10^{19} cm^{-3} — courtesy to Chicot's Ph.D. thesis [74].

trode depletion width is the acceptor concentration extracted. For MESFET, a simplified expression of current in saturation region can be written as [69]:

$$I_{Dsat} = \frac{G}{4V_p}(V_G - V_{TH})^2 \tag{2.16}$$

where G, V_p, V_G and V_{TH} are the conductance, the pinch-off gate voltage and the gate threshold voltage around which the MESFET is turned ON and OFF, respectively. Extrapolation of $I_{Dsat}^{1/2}$ vs. V_G by linear curve gives V_{TH}, the value of V_G at which pinch-off point is reached ($V_G = V_{TH}$). Then, from the gate threshold voltage expression $V_{TH} = V_{bi} - V_p$ with pinch-off voltage V_p expressed as follow,

$$V_p = \frac{q[B]_{V_{TH}} a^2}{2E_0 E_s} \tag{2.17}$$

where a is the epilayer thickness and $[B]_{V_{TH}}$ is the non-compensated acceptors' concentration extracted by V_{TH} technique. Acceptor concentration expression becomes:

$$[B]_{V_{TH}} = \frac{2E_s(V_{bi} - V_{TH})}{qa^2} \tag{2.18}$$

2.2.2 Channel current

Under the assumptions of (1) a uniform channel doping, (2) a gradual-channel approximation (electric field in the x-direction is negligible as compared to the one in the y-direction), (3) an abrupt depletion layer and (4) a negligible gate current, the charge density in the channel Q_p at any distance x that permit the current conduction is proportional to the net channel opening b, and is given by

$$Q_p(x) = qN_A(a - W_D) \tag{2.19}$$

The depletion layer width at any distance x from the source can be approximated to:

$$W_D(x) = \sqrt{\frac{2E_0E_s(V_{bi} - V_D(x) - V_G)}{qN_A}} \tag{2.20}$$

Then, the channel current is the channel charge density multiplied by the carrier velocity and the depth of the channel opening Z, which leads to:

$$I_D(x) = ZQ_p(x)v(x) \tag{2.21}$$

The drain current is independent on the x position within the device.

2.2.3 Saturation velocity/Field mobility

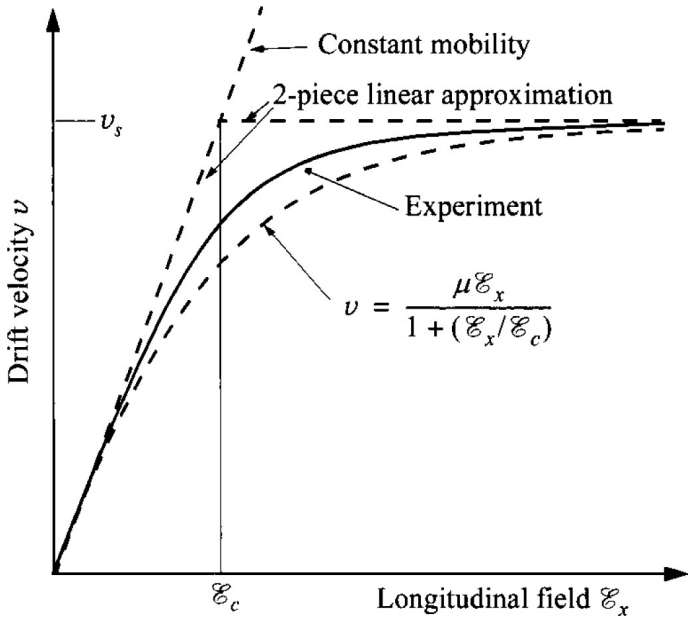

Figure 2.5: Explanation of the drift velocity as a function of electric field. The empirical model of high-field mobility gets close to the experimental characteristics of semiconductors that do not have transferred-hole (or electron) effect [69].

Field effect transistors with short channels have shown discrepancies between basic theory and experiment [69]. The short channel is considered when the channel length is of the same order of magnitude as the depletion layer width of the source and drain. Hence, the devices that will be presented later are only long-channel devices for high voltage application. For long-channel transistors, at a low electric field, the carrier velocity is assumed to be proportional to the field. It is referenced as a constant mobility region (figure 2.5). In this region, the drift velocity increases linearly with increasing the field. However, at higher electric fields, the carrier velocity deviates from the linear dependence

and saturates to a saturation velocity v_s, as presented in figure 2.5 [69]. Diamond drift velocity at saturation reaches 1.1×10^7 cm.s^{-1} and 2.7×10^7 cm.s^{-1} for holes and electrons, respectively.

The field-dependent mobility to explain field effect transistor at high field (and also implemented in the simulation numerical models) follow an empirical formula that has a smooth transition between the constant-mobility regime to the saturation velocity regime. The equation is of the form,

$$\mu_{n,p}(E) = \mu_{n0,p0} \left[\frac{1}{1 + \left(\frac{\mu_{n0,p0} E}{v_{s(n,p)}} \right)} \right] \tag{2.22}$$

where E is the parallel electric field, $\mu_{n0,p0}$ is the low-field electron n0 or hole p0 mobility. The low-field mobility is explained in the next section with J. Pernot's empirical model [66].

2.3 Simulation numerical models

Simulation tools have played and continue to play an essential role in the research and development of power semiconductors. With simulation, straightforward devices, as well as newly designed devices, can be tested without wasting time and money with a new architecture test fabrication. The advantages of the simulation are the ability to automatically optimize the device parameters (architecture or material) and easily visualize the expected physical properties if the right physical models are implemented. This section will introduce the physical models implemented in Silvaco finite element simulation software. In any semiconductor, Poisson's equation that relates the electrostatic potential to the space charge density and the carrier continuity equation can describe the main physics. Depending on the material, appropriate models need to be implemented. In this section, models dedicated to diamond such as incomplete ionization of dopants, temperature and concentration-dependent hole and electron mobility used in the simulation tools will be presented.

2.3.1 Band gap temperature dependence

The band gap formed by the energy difference between the bottom of the conduction band and the top of the valence band determine the electronic properties of a semiconductor. Varshni *et al.* [75] have reported an empirical expression (cf. equation 2.23) of the band gap as a function of the temperature:

$$E_g(T) = E_g(300K) + a\frac{300^2}{\beta + 300} - a\frac{T^2}{\beta + T} \tag{2.23}$$

The band gap energy of semiconductors tends to decrease with increasing temperature. A temperature increase induces an increase of the atomic vibrations amplitude. A. Marechal *et al.* have fitted the experimental diamond data reported by C.D. Clark *et al.* [76] using the equation 2.23 and hence have extracted a and β coefficients for diamond as 1.01007

eV.K^{-1} and 3.951 98 × 10^6 K, respectively. The band gap of diamond at 300 K was set at 5.46 eV.

2.3.2 Incomplete ionization model of impurities

One of the distinguishable characteristics of diamond semiconducting material is its incomplete ionization at room temperature as compared to Si, GaN or SiC due to the deep impurities activation energies as seen in figure 2.6. At 300K the ionization ratio is of one thousandth for boron (B) doping and one millionth for phosphorus (P) doping. These large activation energies of dopants in diamond have pushed the community in exploring specific architectures such as delta-doping [77] to overcome an extremely high series resistance or the use of a hydrogen-terminated surface for surface conduction to reach high current densities [78, 79]. These large ionization ratios are a problem for numerical simulation at room temperature since they lead to convergence problems due to low carrier densities.

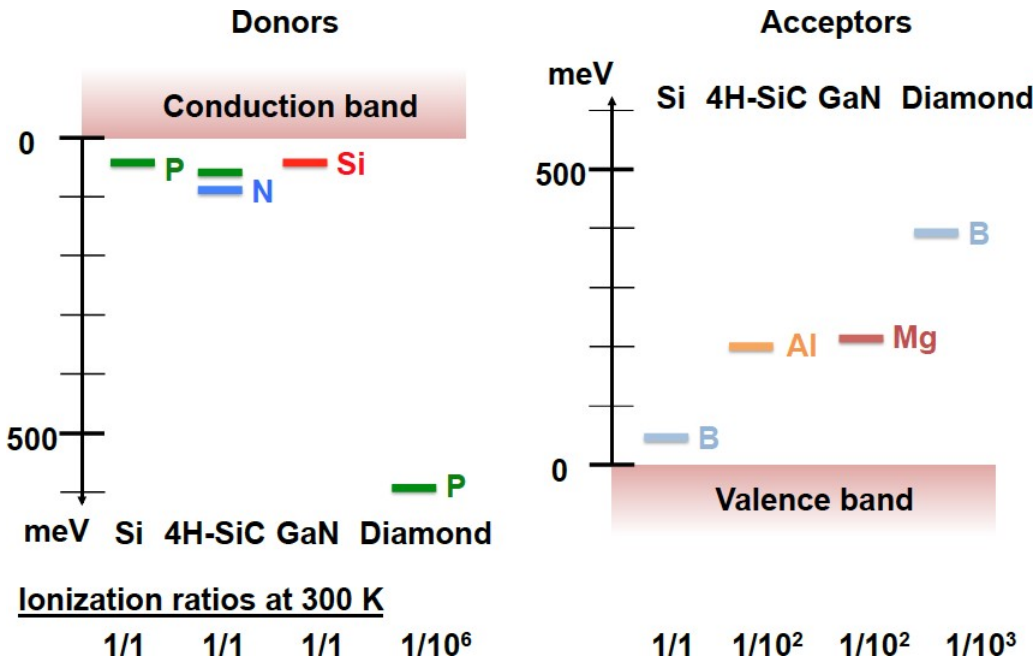

Figure 2.6: Schematic diagram showing the ionization energies of the dopants for Si, 4H-SiC, GaN and Diamond for both donors (n-type) and acceptors (p-type). The ionization ratios are also presented — courtesy to A. Marechal's Ph.D. thesis [80].

From the charge balance equations and the neutrality equation between the number of positive charges and the number of negative charges, the free hole concentration p and the free electron concentration n can be determined using the Fermi-Dirac distribution. Therefore, for a p-type material the free hole concentration p is expressed as:

$$p = \frac{1}{2}(\varphi_a + N_D)\left(-1 + \sqrt{1 + \frac{4\varphi_a(N_A - N_D)}{(\varphi_a + N_D)^2}}\right) \tag{2.24}$$

Similarly, for an n-type material, the free electron concentration is given by:

$$n = \frac{1}{2}(\varphi_d + N_A)\left(\sqrt{1 + \frac{4\varphi_d(N_D - N_A)}{(\varphi_d + N_A)^2}} - 1\right) \tag{2.25}$$

$$\text{where} \quad \varphi_{a(d)} = g_{h(e)}.N_{V(C)}\exp\left(-\frac{E_{a(d)}}{k_B T}\right) \tag{2.26}$$

with $E_a = E_A - E_V$ for the acceptor thermal activation energy and $g_h = 1/g_A = 1/4$ the degeneracy factor for hole, and $E_d = E_C - E_D$ for the donor thermal activation energy and g_e=2 the degeneracy factor for electron [69].

N_A and N_D are the total densities of acceptors and donors, respectively.

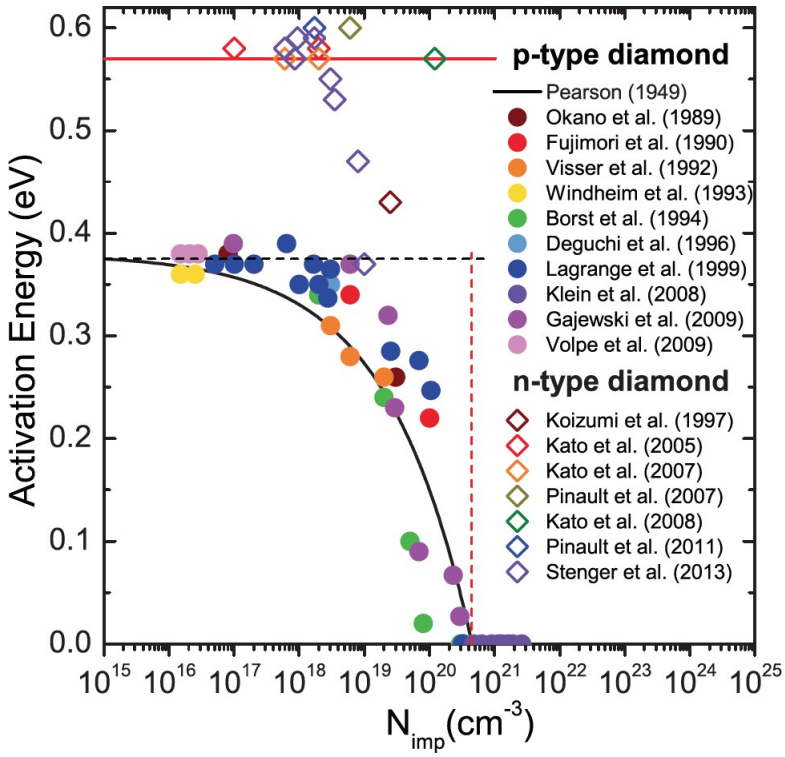

Figure 2.7: Activation energy as a function of the impurity concentration for p-type and n-type diamond. The experimental data for boron activation energies are reported in [81, 82, 83, 84, 85, 86, 87, 88, 89, 90]. The ones for phosphorus were reported by [91, 92, 93, 94, 95, 96, 97]. Solid line for p-type is a fitting curve following Pearson and Bardeen expression [98]. For the n-type, a constant value was assumed — courtesy to A. Marechal [80]

As seen in equation 2.24, the free hole concentration depends strongly on main dopant activation energy and concentration as well as on the compensation concentration. The main dopants in diamond which are boron, phosphorus, and nitrogen have exhibited activation energies of 380 meV, 570 meV and 1.7 eV, respectively. It has been determined that the thermal activation energy of boron dopant decreases when the density of impurities (borons) increases as seen in figure 2.7. Based on an empirical law reported by Pearson

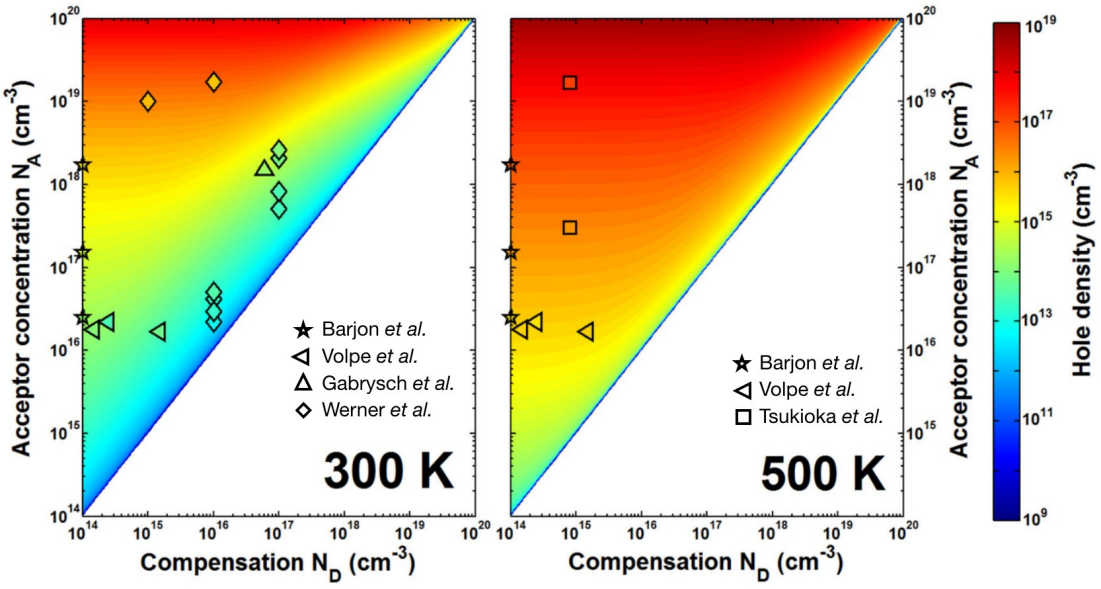

Figure 2.8: Hole density as a function of acceptor concentration (boron) and compensation concentration at 300 and 500 K. Experimental data from [99, 90, 100, 101, 102] were added [103].

and Bardeen [98], experimental reported data for p-type diamond have been fitted leading to the following expression for boron acceptor:

$$E_a(eV) = 0.38 - 4.7877 \times 10^{-8} \times N_A^{1/3} \tag{2.27}$$

In figure 2.7, it is also observable that newly reported experimental data showed that the thermal activation of phosphorus dopant decreases when increasing impurities concentration. It starts to be noticeable thanks to improvement in phosphorus incorporation within diamond enabling to n-type layers with good characteristics [97]. Nevertheless, a constant thermal activation energy of phosphorus donor E_d was set equal to 0.57 eV.

Traore *et al.* [103] have highlighted the importance of compensation percentage in determining the free hole concentration (figure 2.8). Indeed, depending on the compensation ratio, the mobility can be considerably reduced. The percentage of donor compensation is ranging from 1% to 10%. As 10% of donor compensation induces a mobility twice lower, it is crucial to control the impurities during the growth (especially foreign impurities) and to keep the compensation as low as 10%. For a fixed boron doping concentration and a fixed compensation, the hole density increases about one order of magnitude from 300 K to 500 K.

2.3.3 Holes and electrons mobilities model

Hole and electron mobility empirical model that take into consideration temperature and doping concentration was also implemented to the simulation tool. Volpe *et al.* and Pernot *et al.* have suggested an adapted empirical model for diamond that fits the experimental data. The model is for a low-field regime and covers a wide range of doping concentration, extending from 10^{14} cm^{-3} to 10^{21} cm^{-3}. The transition to metallic of diamond boron

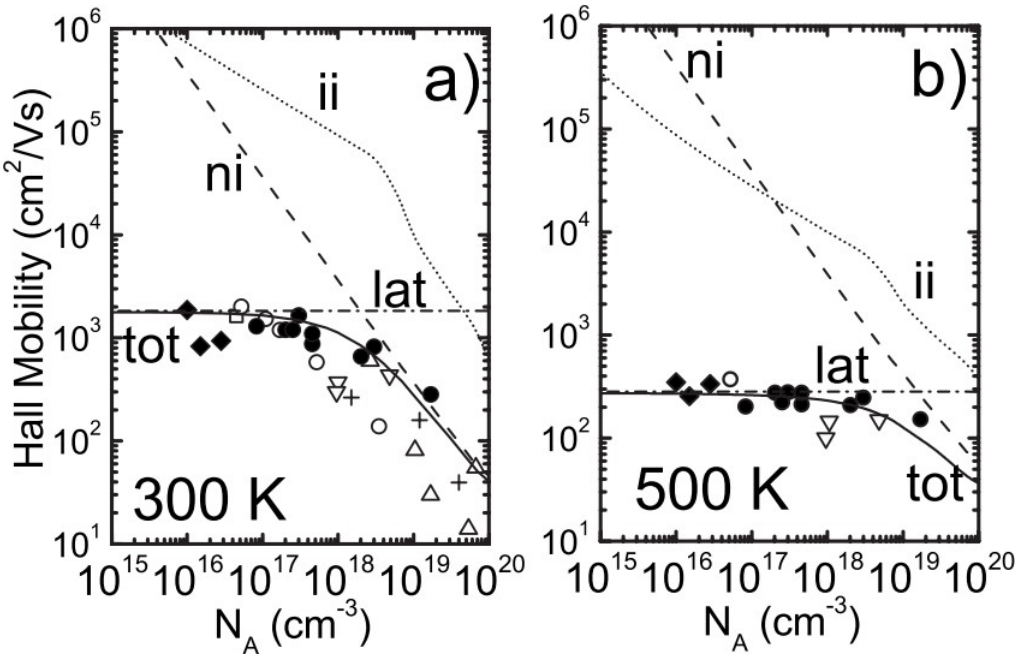

Figure 2.9: Hole Hall mobility as a function of doping level in homoepitaxial diamond at (a) 300 K and (b) 500 K. The model is in good agreement with reported data. Information on symbols experimental data can be found in [66].

doped is at 5 × 10^{20} cm^{-3} [104]. At the lowest doping concentration, the mobility for hole and electron is 2016 $cm^2.V^{-1}.s^{-1}$ and 1030 $cm^2.V^{-1}.s^{-1}$, respectively. The proposed equation consider only phonon and dopants scattering [90]:

$$\mu(T, N_{imp}) = \mu(300, N_{imp}) \times \left(\frac{T}{300}\right)^{-\beta(N_{imp})} \tag{2.28}$$

where $N_{imp} = N_A + N_D$ represents the total concentrations of both acceptors and donors. $\beta(N_{imp})$ and $\mu(300, N_{imp})$ were extracted independently. The expression for $\beta(N_{imp})$ is as follow:

$$\beta(N_{imp}) = \beta_{min} + \frac{\beta_{max} - \beta_{min}}{1 + \left(\frac{N_{imp}}{N_\beta}\right)^{\gamma_\beta}} \tag{2.29}$$

where $\beta_{min} = 0$ for highly doped n-type or p-type diamond, $\beta_{max} = 3.11$ for hole and $\beta_{max} = 2.17$ for electron in a pure material, $N_\beta = 4.1 \times 10^{18}$ and $N_\beta = 3.75 \times 10^{17}$ for hole and electron, respectively. For boron-doped diamond, $\gamma_\beta = 0.617$ and for phosphorus doped, $\gamma_\beta = 0.585$. And finally, the concentration dependence of the mobility at 300 K:

$$\mu(300, N_{imp}) = \mu_{min} + \frac{\mu_{max} - \mu_{min}}{1 + \left(\frac{N_{imp}}{N_\mu}\right)^{\gamma_\mu}} \tag{2.30}$$

with $\mu_{min} = 0$ $cm^2.V^{-1}.s^{-1}$ for highly doped diamond for both hole and electron. At this

high doping diamond, hopping phenomena occurs. The high-field mobility model for field effect transistors was described in the previous section.

2.3.4 Avalanche mechanism

The two main processes that limit the device operation at the off-state are a breakdown due to an important amount of leakage current and an avalanche breakdown phenomena. The leakage current can be induced by the presence of defects within the layer or due to process fabrication [105]. The breakdown by avalanche mechanism can be obtained if a specially designed structure is used to distribute the electric field within the semiconducting material. When the leakage current increases, the power dissipation increases as well. It is then essential to use a designed structure that creates the high electric field inside the drift layer. Edge termination devices are one of the power devices that are designed to withstand high voltages within a depletion layer. In this depletion region, an electric field is produced due to the applied voltage. Any electrons or holes that penetrate the depletion layer are swept out. By increasing further the electric field, the carriers gain sufficient kinetic energy to interact with the lattice atom to create electron-hole pairs. The excited electrons will move from the valence band to the conduction band. The first electron-hole pair generated, is dissociated and accelerated under the electric field which ends with the creation of other electron-hole pairs. This impact ionization that created electron-hole pairs undergoes a multiplicative phenomenon which terminates in an avalanche event. The avalanche generation rate G_{av} is expressed as follow:

$$G_{av} = a_n.n.\upsilon_n + a_p.p.\upsilon_p = \frac{1}{q}(a_n j_n + a_p j_p) \tag{2.31}$$

υ_n and υ_p are the drift velocities at which travel electrons and holes, respectively. j is the drift current. At high electric field, only drift current is considered, the current from diffusion is neglected. In the simulation presented later, the implemented model uses the Chynoweth's law [106]:

$$a_{n,p} = A_{n,p}\, exp^{\left(-\frac{B_{n,p}}{E}\right)} \tag{2.32}$$

where $a_{n,p}$ is the impact ionization coefficients for electron (n) and hole (p). A and B are material and temperature dependent constants. For diamond, no accurate impact ionization coefficients were reported at room temperature and none as temperature de- pendent. An analysis of diamond impact ionization is given in Chapter 5. Based on this study, impact ionization coefficients reported by Watanabe *et al.* [107] and extracted by Hiraiwa *et al.* [108] are used in simulation to characterize the reverse state of the devices.
The parameters for the impact ionization coefficients are $A_n = 4.62 \times 10^5$ cm^{-1} and $B_n = 7.59 \times 10^6$ V.cm^{-1} for electrons, and $A_p = 1.93 \times 10^5$ cm^{-1} and $B_p = 4.41 \times 10^6$ V.cm^{-1} for holes. The constants are temperature independent. The choice of these coefficients gives a low limit of the device expected characteristics in reverse state since no accurate coefficients are reported.
The number of electron-hole pairs generated in the depletion region due to one electron-hole pair initially created is given by [109, 110]:

$$M(x) = 1 + \int_0^x a_n M(x)dx + \int_x^W a_p M(x)dx \tag{2.33}$$

with W the width of the depletion region. A solution to this equation is

$$M(x) = \frac{\exp\left[\int_0^x (a_n - a_p)dx\right]}{1 - \int_0^W a_p \exp\left[\int_0^x (a_n - a_p)dx\right]dx} \tag{2.34}$$

M(x) is the multiplication coefficient. One of the condition to consider avalanche breakdown is when the multiplication coefficients tend to infinity, meaning that ionization integral equal 1 as follow:

$$\int_0^W a_p \exp\left[\int_0^x (a_n - a_p)dx\right]dx = 1 \tag{2.35}$$

Additionally to the numerical models that suit for diamond, diamond intrinsic parameters such as a positive electron affinity (EA) of 1.7 eV corresponding to an oxygen-terminated diamond surface was also set.

2.4 conclusion

In this chapter, the underlying physical theory behind the unipolar devices was described. The strength of unipolar devices is their ability for a fast switch and low power loss due to the only presence of majority carriers as compared to bipolar devices where minority carriers injection is required. The current transport in the forward and reverse state of a Schottky diode is now well established and explained by thermionic emission (TE) for the on-state. For the off-state, TE and in some cases TE plus thermionic field emission (TFE) is required to understand the leakage currents. Metal-semiconductor field effect transistor (MESFET) which is a complementary power switch also important for commutation cells, is modulated by a Schottky gate electrode that can explain the reverse current mechanism of the MESFET.
To predict the device performances and to visualize the physics within the device, simulation tools are of great importance. But it is doable only with the appropriate models that fits diamond material. In that aim, non-negligible models such as bandgap temperature dependence, incomplete ionization of impurities, concentration and temperature dependence mobilities for electrons and holes as well as high-field mobility model for transistors and avalanche mechanism were implemented in numerical simulation.

Chapter 3

Micro-fabrication process engineering and characterization tools

Contents

This chapter is the base of the next generation diamond device development. Devices must fulfill several requirements in order to reach the material limits. It has been shown in the previous chapter that being able to anticipate the architecture and electrical properties of a device are one of the requirements for a successful device. The obvious step following the simulation is the process fabrication that is complementary with the characterization tools.
In the first part, all the steps lived by the devices from wafer growth to metal deposition will be presented. In the second part, facilities used in France and in Japan to characterize the samples are described.

3.1 Diamond birth

When we talk about diamond, the first words that come in mind are a gemstone, jewel, luxury, expansive and so on. But diamond is more than that. So, what is diamond?
In the atomic scale, a diamond is a perfect organization of carbon (C) atoms, as seen in figure 3.1-b. It has a face-centered cubic (fcc) lattice with four carbon atoms as tetrahedral position (labeled in red in figure 3.1-c). Each atom is bonded covalently with four other carbon atoms organized as an sp^3 hybridization - The lattice of diamond count 8 C atoms per unit cell. It is formed from two diamond fcc cells shifted by a quarter of its diagonal and have 0.357 nm for the lattice parameter. The shortest distance between two consecutive atoms (nearest neighbors) is of 1.54 Å. Owing to this strong bonding, the high energy required to separate the strong covalent bonds make diamond one of the hardest material. Additionally to the strong covalent bonds, its low phonon scattering make diamond a perfect thermal dissipator material (high thermal conductivity).

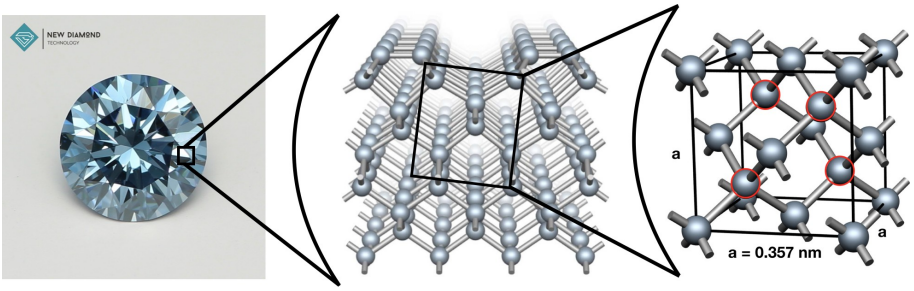

Figure 3.1: Diamond from macroscopic to nanoscopic scale. a) Picture of a polished diamond for jewelry from New Diamond Technology [111], b) atomic geometries organization of carbon atoms (extracted from [112]) formed by several c) face-centered cubic diamond lattices.

3.1.1 Diamond in nature

Before being artificially created, diamond was (and is still) created by nature. It is formed under Earth's mantle and emerges at the surface through a volcano. It can also be formed when meteorites strike with the ground, referring to the detonation process. In both cases, severe conditions are needed and especially extreme pressure and temperature. As represented in the carbon phase diagram in figure 3.2, diamond is a metastable form of carbon. It can rapidly convert to graphite which is the most stable phase, i.e. following an

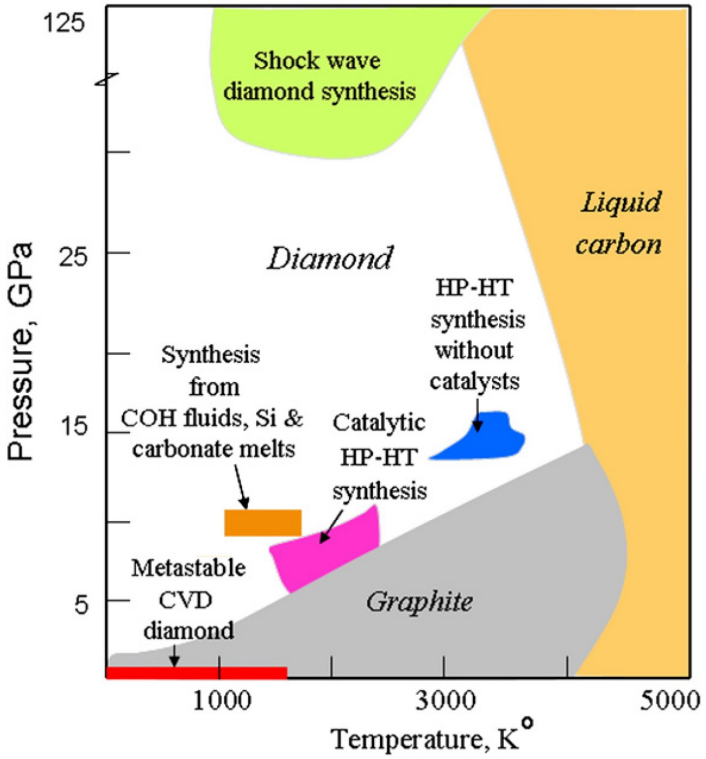

Figure 3.2: Carbon phase diagram. High pressure and high temperature are the key parameters of diamond fabrication [113].

sp^2 hybridization. Diamond can be found with some impurities in within. Nitrogen (N) and Boron (B) are the most common ones. A classification was established (figure 3.3) taking into account the type of impurities and their arrangement. Such a classification exist only for minimum detectable impurities (using infrared IR technique). Impurities can take an interstitial or substitutional position. This possible replacement of a carbon atom by a foreign atom makes diamond a semi-insulating material, that can be either insulating or conducting.
We distinguish two main types: I and II. Type I contains nitrogens and type II, borons. Then, depending on the organization, these types are sub-differentiated.

3.1.2 Diamond for electronic purpose

At the end of 1954, Tracy Hall (from General Electric) reported the first synthesized diamond using the catalytic HPHT synthesis [115]. Since this year, synthetic diamond has known a significant improvement. We entered "the age of Diamond". Two ways are now offered to synthesize diamond:

3.1.2.1 High-Pressure High-Temperature (HPHT)

This technique, also known as temperature gradient process, reproduces the natural condition at which diamond is obtained. It uses a molten catalyst to dissolve the carbon source (such as a small diamond seed or graphite), then transforms this dissolved carbon to a diamond crystal by forcing the precipitation. The pressure ranges from 5 to 6.5 GPa

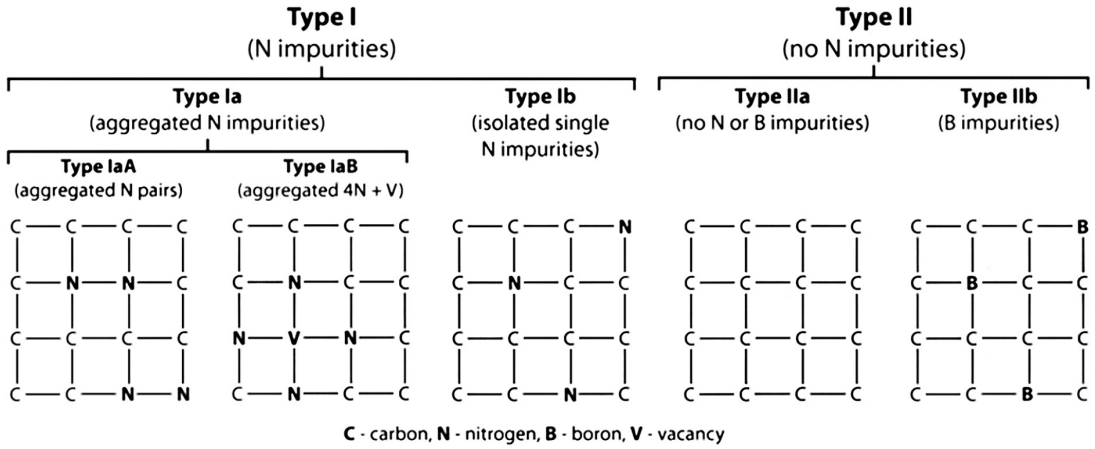

Figure 3.3: Conventional classification of the different discovered diamond. It exists two main types (I and II). Type I encloses N impurities and type II has no N impurities [114]. Type Ib and IIb are mainly used for power electronic device fabrication.

and the temperature from 1300°C to 1700°C [116]. HPHT diamond production requires huge facilities which can turn to be rapidly restrictive and expansive. Generally, they are produced by companies such like Sumitomo Electric Industries, Ltd., Element Six Synthetic Industrial diamond, TISNCM, New Diamond Technology, etc. and preferentially used as a base substrate for diamond grown by chemical vapor deposition.

In this study, synthesized HPHT type Ib (diamond substrates with isolated single N impurities) and type IIb (diamond substrates containing high boron impurities amount) were used. All substrates provided by Sumitomo Electric Industries Ltd. and TISNCM had 3x3 mm^2 size and were sent polished using an abrasive process (Scaife polishing).

3.1.2.2 Chemical Vapor Deposition (CVD)

As it is said in its title, the desired film is grown by a reaction at the substrate surface of different gas precursors. Compared to HPHT synthesis, CVD growth occurs in principle at low pressure - i.e., from 25 to 65 kPa - and low temperature - i.e., from 700°C to 950°C (figure 3.2) controlled by a plasma. A wafer is needed to use the CVD technique. Generally, HPHT substrate wafers are the best base for high-quality film production. This technique is used to grow polycrystalline diamond film (such as for coating purpose) or to grow homoepitaxial single-crystal diamond films. Nowadays, it exists more than ten types of CVD technique. Here are the two main methods:

- **Microwave Plasma CVD (MPCVD)**
- **Hot-Filament CVD (HFCVD)**

Doping concentration and thickness are well mastered in MPCVD and HFCVD. The advantages of CVD systems is their low cost for solid film fabrication owing to affordable facilities. The main problem that is on the way to be solved is the high dislocation density obtained after CVD growth. Recently, DiamFab, a promising startup develops epitaxial layers grown by MPCVD with good control of doping level and thickness as well as low dislocation densities. S. Ohmagari *et al.* reported a reduction of dislocation density

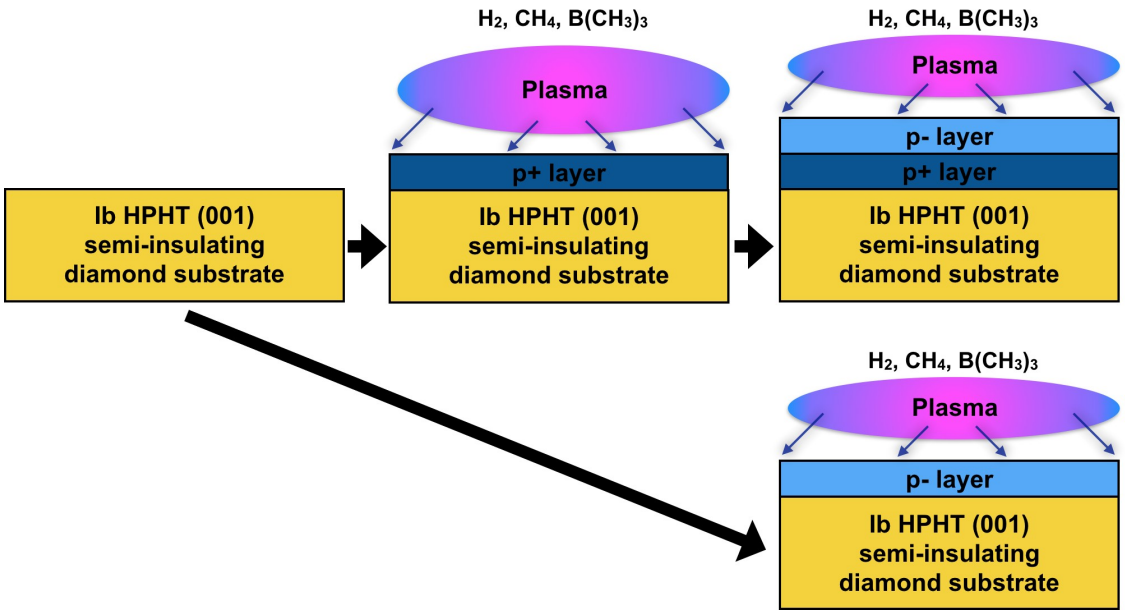

Figure 3.4: Schematic cross-sectional growth of diamond epilayers by chemical vapor deposition. Stacks p^+/p^- on Ib HPHT diamond were used for Schottky diodes, and p^- on Ib HPHT diamond was used for field effect transistors.

going from 10^6 cm^{-2} (for substrate) to 10^4 cm^{-2} (for epilayer) when using HFCVD technique explained by incorporation of tungsten W atoms that may suppress the propagating dislocations [117].

3.1.3 Homoepitaxial layers growth

Two main steps are required before the first layers growth by CVD: A re-polishing and a chemical acid cleaning of the diamond substrates. The HPHT substrates were sent to Syntek Co. Ltd. for the polishing process. Syntek Co. Ltd. is a Japanese company that provides an accurate polishing (roughness of about 0.3 nm) as compared to the received polished HPHT substrates (roughness of about 1.6 nm). The obtained atomically flat surface (close to the atomic size) reduces the defect formation at the epitaxial layer which generally starts at the epi-layer/substrate junction. Then, several steps of different acid mixtures were performed at different temperatures and waiting times. Sulfuric acid H_2SO_4, nitric acid HNO_3, hydrochloric acid HCl, hydrogen peroxide H_2O_2 and hydrofluoric acid HF were the main manipulated acids. The acid treatment process has the target to remove strong organic contamination, any residual metal contamination and graphitized formed a layer at the surface. All the substrates have a misoriented angle θ between 2° and 2.5° along with (110) determined by X-Ray Diffraction (XRD) analysis. The high misorientation angle enhances lateral growth and permits to grow a hillocks-free heavily doped diamond layers [118]. The diamond epi-layers used were grown using Seki-ASTeX type reactors MPCVD provided by Seki Diamond Systems (a unit of Cornes technologies Ltd.). Some of the layers were grown by Dr. Yukako Kato and Dr. Masahiro Ogura from AIST Tsukuba (Japan) and others by Dr. Hitoshi Umezawa from AIST Kansai (Japan). Depending on the final design needed, it is possible to start either by a heavily

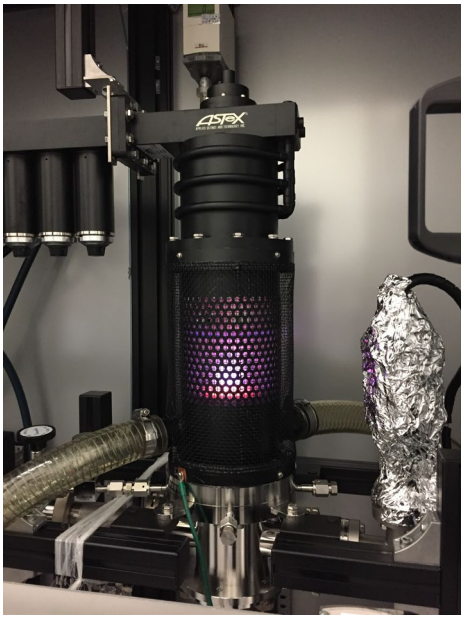

Figure 3.5: Picture of a reactor chamber during growth realized at AIST - Japan. The plasma is observable.

layer	CH_4/H_2 [%]	B/C [%]	O/C [%]	Pressure [Torr]	Power [W]	Growth rate [$\mu m/h$]
p^-	2-4	0	0.4-0.6	120	3900	1.5 - 2.5
p^+	4	1.6	0	25	700	0.14

Table 3.1: Growth parameters of lightly (p^-) and heavily (p^+) boron-doped diamond layers. The layers were grown at AIST in Japan.

doped boron layer (p^+ layer) or by a lightly doped boron one (p^- layer), as represented in figure 3.4. Basically, the stack p^+/p^- on Ib HPHT diamond is used for Schottky diodes fabrication and the p^- layer directly on the semi-insulating Ib HPHT diamond is used for field effect transistors. A picture showing the plasma in the reactor chamber was taken during growth (see figure 3.5). The diamond boron doping was achieved using trimethyl boron ($B(CH_3)_3$) precursor gas.

Unfortunately, I had no opportunities to realize epilayers growth at DiamFab [119] (Start-up of Institut Neel/CNRS) due to a limiting time. DiamFab proposes excellent layers quality and good control of layer parameters.

Table 3.1 encloses the typical epilayers growth parameters realized in Japan. A maximum thickness of 1 μm for the heavily doped boron layer was set to avoid dislocation propagation of the p^+ towards the drift layer.

3.2 Post-growth characterization

In this section, an introduction of the apparatus used to characterize the samples, and some obtained results are presented. Only some typical results are shown since they are similar to the obtained one for the other samples.

3.2.1 Surface morphology

• Optical microscope

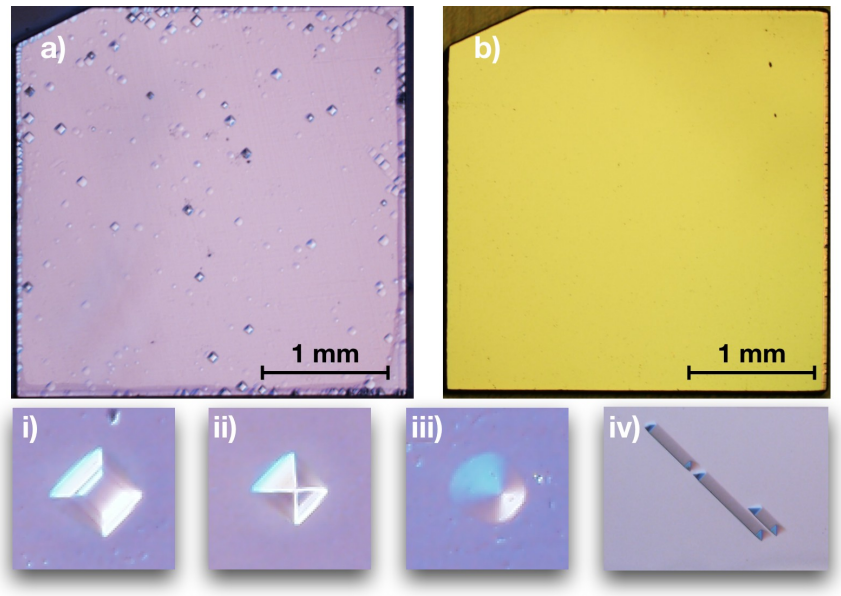

Figure 3.6: Surface images of two different samples after last layer growth showing a) eventual defects observed with i) Flat-topped hillocks, ii) Pyramidal hillocks, iii) Round hillocks and iv) Linear type substrate threading dislocation; and b) a flat surface with no noticeable dislocations.

The first straightforward characterization realized after layers growth is the observation of the surface by an optical microscope. Figure 3.6 shows the top surface images of two substrates after growth exhibiting an eventual surface defect in some cases. Figure 3.6-b represents a well-controlled growth with no propagating hillocks and no visible surface defect. However, it happens, when the growth parameter is not controlled, or a substrate is not correctly prepared (polishing and/or acid washing) or even when the chamber growth is contaminated to notice surface defects. Figure 3.6-a is an example of an epilayer exhibiting different kinds of defects such as i) flat-topped hillocks, ii) pyramidal hillocks, iii) round hillocks or iv) linear type dislocation. Some of them are threading dislocations spreading from substrate to the surface of the homoepitaxial layer; others are generated during CVD growth and ones are originated from substrate surface due to polishing defects. To reduce or remove defects induced by the polishing process, oxygen plasma etching and(/or) H_2/O_2 plasma etching prior to growth can be applicable [120, 121].

• Optical Profiler

Optical profilometry is another way to characterize the surface morphology. Additional to surface information, such like defect type, an optical profiler gives information on surface roughness. Compared to atomic force microscopy (AFM), optical profiler surface characterization technique is a high-speed system. It is also possible to have large area roughness characterization which is less accessible in case of AFM. Figure 3.7 obtained using a Veeco 3D ContourGT is a typical surface topography of post-grown p^- layer. This optical profiler has a vertical resolution of about 0.1 nm and a lateral resolution of about 0.5 μm. The average roughness for this sample is 12.1 nm.

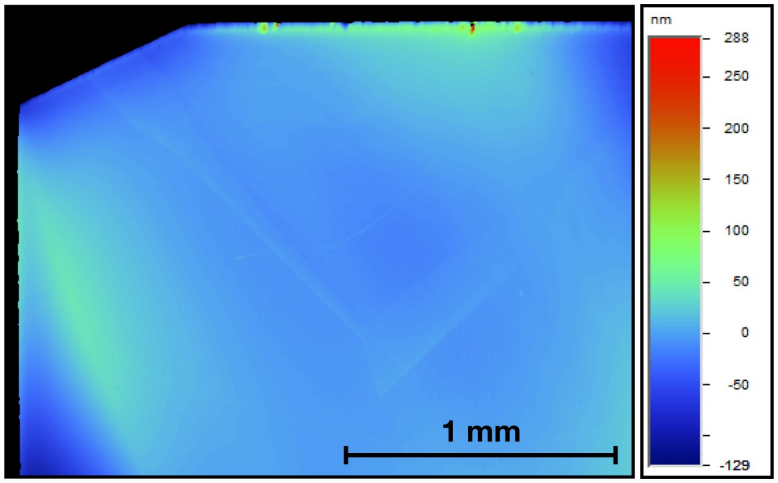

Figure 3.7: Typical surface image obtained by optical profilometry. Information on surface roughness and possible defect presence are given. The average roughness is of 12.1 nm. A growth sector is also observable at the diamond surface.

3.2.2 Doping and thickness

3.2.2.1 Secondary Ion Mass Spectroscopy (SIMS)

Secondary ion mass spectroscopy (SIMS) is a technique that analyses physical impurities in solids. With the help of an ion beam as sputtering, materials are removed from the solid. The sputtered ionized atoms are analyzed by an energy filter and a mass spectrometer that can detect all kind of species. The method is a destructive process since a hole (crater) is created to count the total of impurities that are incorporated in the solid for a given surface and depth. Since then, the level of impurities extracted is the total concentration (in substitution and interstitial positions) and not the electrically active impurity concentration. Figure 3.8 is the atomic concentration of boron B, silicon Si, hydrogen H and nitrogen N impurities for 2 different samples labeled RB-MESFET#1b, 2b as a function of depth. MST Co. Japan performed all the SIMS measurements. A CAMECA IMS-4f instrument and a Cs^+ incident ion beam with an acceleration energy of 14 keV were used. The company provides the background level (B. L.) and detection limit (D. L.), and they depend on the ion used as a beam. When using a low energy beam measurement, especially a beam of O_2^+ with an energy of 3 keV, the sensitivity is improved and can reach a dopant density detection as low as 10^{14} cm^{-3}. SIMS method provides at the same time the atomic concentration and the thickness of the epilayers.
The Ib HPHT substrate is well characterized by the presence of N atoms. Nitrogen concentration is about 2×10^{19} cm^{-3}. Also, a boron peak at the junction substrate/p- type homoepitaxially grown appears. This rise of boron concentration at the beginning of the p-type layer may be due to the memory effect of the growing chamber. Sample RB-MESFET#1b have shown a high silicon doping level of 5×10^{15} cm^{-3}. During the growth, the plasma was not centering and hence was touching the quartz tube which is why Si impurities were detected. The concentrations extracted from SIMS curves are mean values since relatively important fluctuation can be noticed.

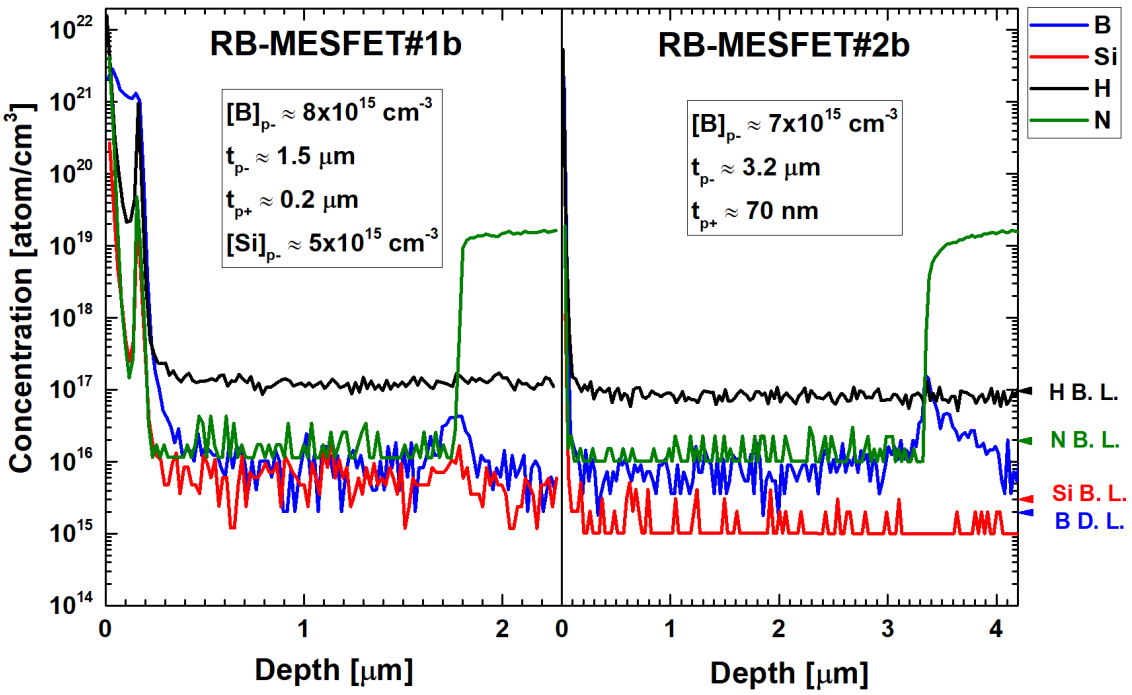

Figure 3.8: Typical SIMS results obtained for 2 samples (RB-MESFET#1b, RB-MESFET#2b) used to fabricate field effect transistors. B. L. corresponds to the background level, and D. L. is the detection limit. RB-MESFET refer to Reverse-Blocking metal semiconductor field effect transistor. More details will be given at the end of this section. SIMS, *Secondary Ion Mass Spectroscopy*.

3.2.2.2 Cathodoluminescence (CL)

A second method to extract doping concentration is the cathodoluminescence (CL) analysis. At the opposite of SIMS method, CL technique is a non-destructive and a contactless method. The sample is excited by an electron beam, and a light is collected and analyzed. It is generally used to study defects and but also dopants in semiconductors. The light collected comes from electron-hole pairs or exciton created by the accelerated electron beam that undergo radiative recombination (photons). To extract the doping level, excitonic energy region (between 5 and 5.5 eV for diamond) is considered. Van der Waals interactions (Bound Exciton BE) of neutral impurities to the Free Exciton (FE) are the keys to have information on doping level. In general case, CL measurement is performed at a low temperature (5 K) to enhance the BE exciton radiation. Diamond has an indirect gap, hence FE and BE are assisted by phonon as seen in figure 3.9 [73].

TO stands for transverse optic, LO for longitudinal optic, TA for transverse acoustic and LA for longitudinal acoustic. They are the main phonons interactions involved in the diamond excitonic transitions [122]. The energies of the phonon involved in excitonic recombination BE^{TO} and FE^{TO} are 5.215 eV and 5.268 eV, respectively. F. Omnes *et al.* have proposed an empirical linear relationship between boron concentration [B] and CL intensities ratio $I_{BE^{TO}} / I_{FE^{TO}}$ for a doping level ranging from 10^{16} cm^{-3} to 10^{18} cm^{-3} as follows [123]:

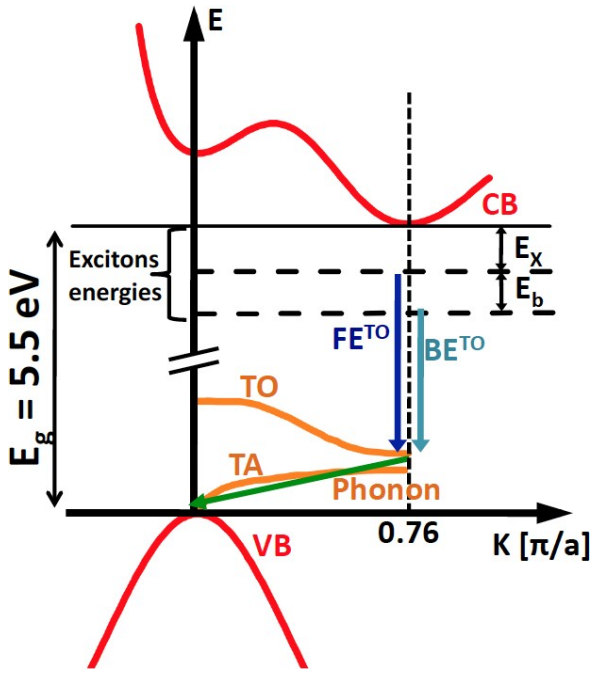

Figure 3.9: Diamond band diagram. It has an indirect gap as seen with the shift of the extrema of the conduction (CB) and valence (VB) bands. FE and BE transitions are assisted by phonon — courtesy to A. Traore's Ph.D. thesis [73].

$$[B]_{CL}\ (cm^{-3}) = 3.5 \times 10^{16} \times \frac{I_{BE^{TO}}}{I_{FE^{TO}}} \tag{3.1}$$

Mr. Sylvain Finot, an internship student, has realized CL spectroscopy on sample RB-MESFET#1b to confirm the boron doping level extracted by SIMS. Figure 3.10 shows a CL intensity for a wide range of energy and a zoomed window at the two main peaks (BE^{TO} & FE^{TO} in dashed lines) that are important to determine the doping concentration. Analyzing the sample at several areas and using equation 3.1, a boron doping level mapping was obtained. The minimum $[B]_{min}$ and maximum $[B]_{max}$ extracted doping levels were 5×10^{15} cm^{-3} and 6.9×10^{15} cm^{-3}, respectively. It concluded an average value $[B]_{mean}$ of 6.2×10^{15} cm^{-3}. The values have an estimated minimum error (on measurement, on acquisition time and on extracted coefficient in the formula given in equation 3.1) of 6.9×10^{14} cm^{-3}.

3.2.2.3 Other methods

Other methods to determine epilayers doping concentration and thicknesses are Capacitance-Voltage C(V) and threshold voltage measurement. They are post-fabrication device method characterization. Both of them relies on the dependence of the space-charge region (SCR) on the reverse bias and assume a uniform doping profile. Since the depletion region is solicited, and hence the presence of the electric field, only electrically active borons are extracted which we will call acceptors concentration (N_A - N_D). Donors compensate these acceptors with a concentration N_D. The theory behind the two methods is given in chapter

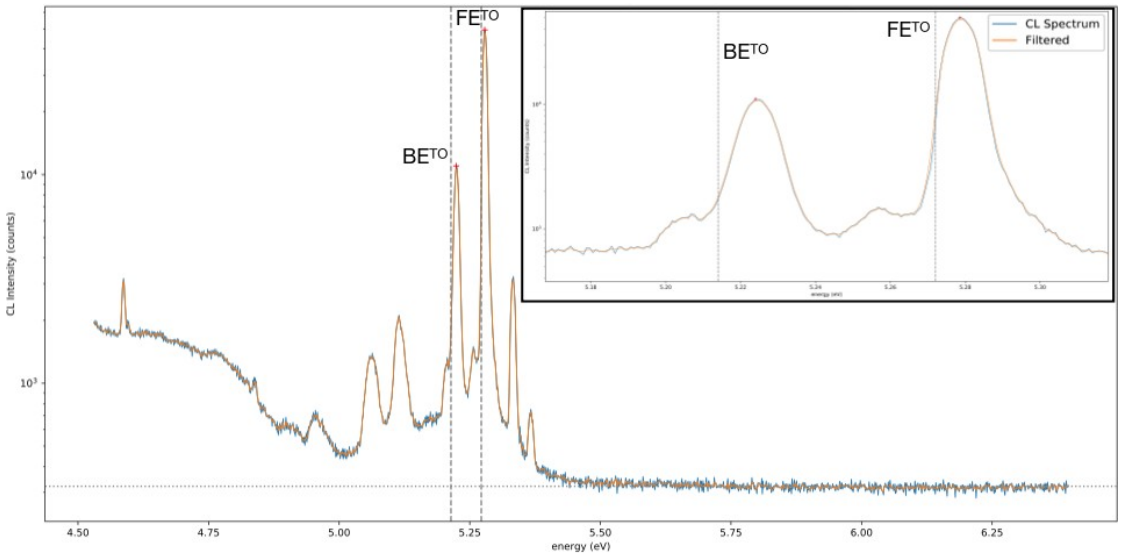

Figure 3.10: 5K cathodoluminescence spectrum for sample RB-MESFET#1b with energy ranging from 4.5 eV to 6.3 eV . Dashed lines are reference energies for BE^{TO} and FE^{TO}. The top right window is a zoomed region near the main peaks.

2. Other approaches to characterize doping concentration and epilayer thickness such like in-situ (or ex-situ) ellipsometry or infrared (IR) spectroscopy exist.

As discussed below, SIMS method gives a boron atomic concentration of all impurities electrically active or inactive and can be summarized as $[B]_{SIMS} = [B]_S + [BH] + [BV\ complex]$. Since CL is based on phonon emission, it gives information on substitutional boron as well as electrically inactive passivated boron by hydrogen (BH pairs) because the energy to dissociate them is high enough and hence, $[B]_{CL} = [B]_S + [BH]$. Finally, the acceptor concentration extracted by C-V or threshold voltage measurement gives the concentration of only the electrically active impurities which are not compensated $[B]_{CV} = [B]_S - N_D = N_A - N_D$.

Table 3.2 summarize all the samples processed with parameters such as doping concentrations and thicknesses, as well as the technique used to characterize them.

3.3 General process fabrication

In this section, a standard process fabrication is described. As different types of devices were fabricated, only some steps will change among the various structures even if the general idea remains the same. The technological manipulation requires an extremely clean environment to avoid contamination and failure.

3.3.1 Diamond device structures

In this work, different types of structures were used depending on the purpose and the device we intended to fabricate. Figure 3.12 presents a schematic of these structures where A corresponds to a pseudo-vertical type, B the vertical type and C the lateral one. As seen

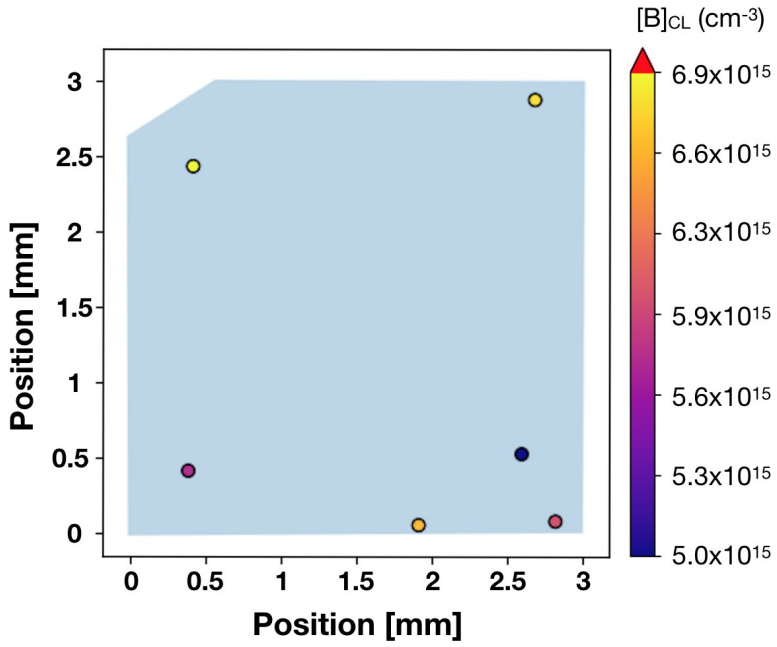

Figure 3.11: Boron doping level mapping of sample RB-MESFET#1b extracted by CL. $[B]_{min}$ was 5×10^{15} cm^{-3}, $[B]_{max}$ was 6.9×10^{15} cm^{-3}, an average value $[B]_{mean}$ was determined to be 6.2×10^{15} cm^{-3}.

in the figure, a pseudo-vertical structure uses a stack of homoepitaxially grown heavily boron doped (p^+ layer) and lightly boron doped layers (p^- layer) on an Ib HPHT semi-insulating diamond substrate. The vertical structure has only one grown active layer since the substrate is a heavily doped boron diamond. As for the lateral structure, the active layer (p^- layer) is directly grown on the Ib HPHT diamond substrate. A and B were used to fabricate Schottky diodes, and C was used for MESFETs fabrication.

A pv-SBD will induce an extra p^+ resistance depending on the distance between the Schottky and the Ohmic contact and hence, SBDs will have a varying total on-resistance which depends on their location. However, the total resistance is equivalent for all SBDs fabricated on a vertical structure [124].

3.3.2 Ohmic contact formation

Ohmic contacts were achieved by forming a carbide at the Ti/p-type diamond junction. The titanium carbide (TiC) formed induces poor interface quality and increases tunneling of the carrier through the small barrier (about 0.63 eV) [125]. Prior to any fabrication process, the samples were cleaned by chemical solvent (acetone, ethanol, and isopropanol (IPA)) to remove any residual organic or dust particles. This part of fabrication was realized at AIST - Tsukuba.

- **For pseudo-vertical structure**

Figure 3.13 summarizes the steps for Ohmic process fabrication in case of a pseudo-vertical structure. Using a photolithography process and a lift-off technique, a titanium (10 nm)/gold (200 nm) (Ti/Au) mask was deposited by electron beam (e-beam) evap-

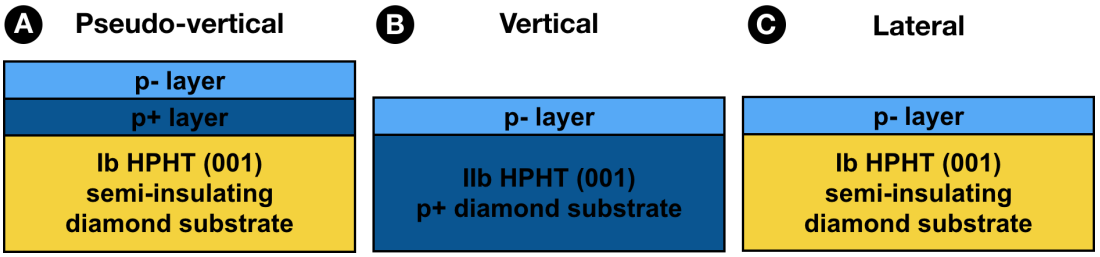

Figure 3.12: Schematic cross-sectional views of the structures used to fabricate the devices. Structures obtained after diamond growth and before any metal deposition. Pseudo-vertical (A) and vertical (B) structures were used for Schottky diodes fabrication and lateral structure (C) for MESFETs.

orator leaving free access to diamond surface at the four corners of the sample. Then, unprotected diamond areas were etched by inductively coupled plasma (ICP) technique to reach the buried highly conductive layer. After the etching, Ti/Au mask was removed by hot acid mixture and 300 μm circular Ohmic contacts deposited at the etched regions using a hard metal mask. A stack of Ti(30 nm)/Pt(30 nm)/Au(100 nm) was deposited by an e-beam evaporator. To get the Ohmic characteristics, the substrates were annealed at 450°C for 60 minutes under argon (Ar) atmosphere using a rapid thermal annealing (RTA) system working with an electrical lamp. The annealing promotes TiC formation at the interface Ti/p-type layer by strengthening the Ti-C covalent bonds and hence reducing the barrier height.

- **For vertical structure**

Ohmic contact formation for vertical structures needs fewer steps than the pseudo-vertical structure where access to the buried p^+ layer is required. As shown in schematic figure 3.14, the samples were fixed into a unique diamond holder and leaving access to the backside substrate. Then, same metal deposition and annealing system, as described above, were used. In Ti/Pt/Au, Ti is the main contact, Pt plays the role of a barrier to avoid Ti and Au migration. And finally, Au was added to prevent metal oxidization by the air.

- **For lateral (planar) structure**

Lateral (or planar) type devices have the Ohmic contact at the top of the active layer. A 400 nm Ti mask was obtained by lift-off technique after the photolithography process. This metal mask was used for the selectively grown heavily doped boron layer. The growth conditions are summarized in table 3.1. Six samples were set simultaneously for the growth. To remove the Ti mask, a hot acid mixture (as described earlier) was used. Then, a second photolithography process was realized, and a Ti(30 nm)/Pt(30 nm)/Au(100 nm) layers were deposited on the previously selectively grown p^+ layer. To get the Ohmic behavior, the samples were annealed with RTA system (similar process as above). For a long time growth, the usual Ti/Au mask does not suit anymore because of Ti atoms diffusion in Au film observed in our experiments [126, 127].

To confirm the absence of TiC at the surface after hot acid mixture treatment, X-ray photoelectron spectroscopy (XPS) was performed with the help of Dr. Yukako Kato from AIST - Tsukuba. XPS analysis had shown neither TiC (281.8 eV) nor Ti (454.7 eV) contamination at the surface [128], as presented in figure 3.16. Only C1s and O1s peaks

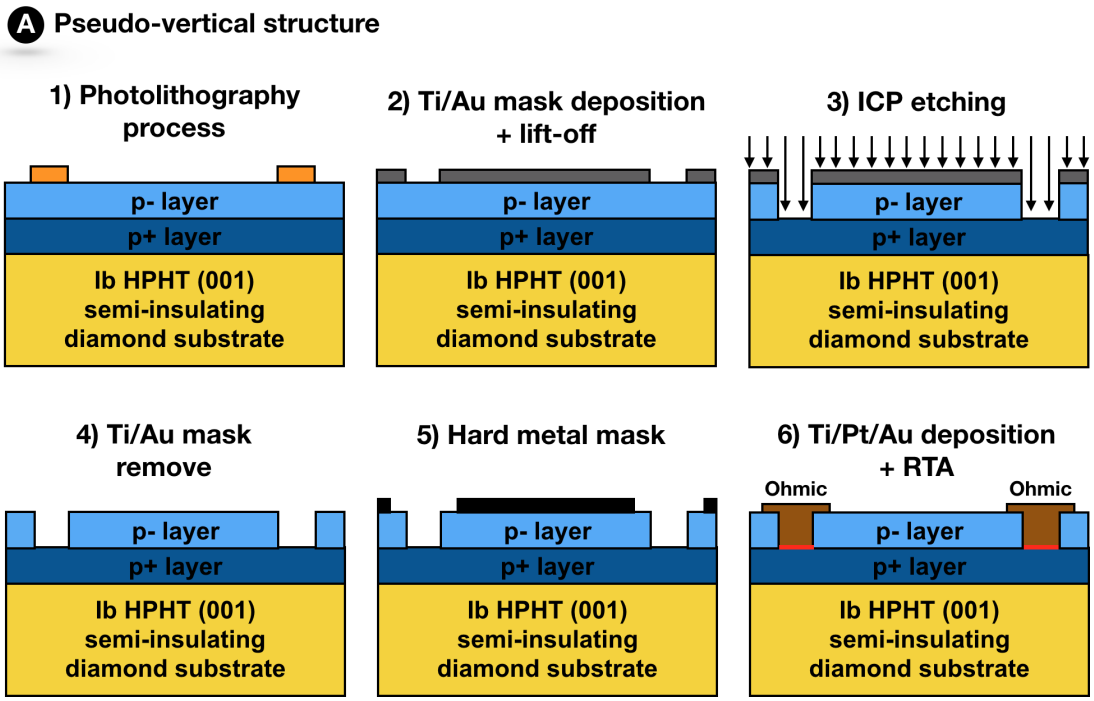

Figure 3.13: Main process steps for Ohmic contact fabrication in case of pseudo-vertical structures. TiC (represented in red) is formed at the last step after RTA.

were noticed at 284.5 eV and 531 eV, respectively [129, 130].

3.3.3 Schottky electrode design

Schottky contact formation is equivalent for all kind of devices fabricated here since unipolar layers were prepared. The difference lies in designing the edge termination for the Schottky barrier diodes. In the following subsections, a description of each edge termination architecture fabrication and the gate MESFETs will be given. The general idea of Schottky formation was kept similar to all of them using the main steps such as an oxygenated diamond surface and a deposition of molybdenum (Mo) metal for Schottky barrier formation. O-terminated diamond can be obtained either by mixed hot acid treatment (H_2SO_4 and HNO_3 at 200°C) [131], or by ultraviolet (UV) ozone treatment using oxygen [132].

3.3.3.1 Floating Field Rings Edge termination

The floating field rings (FFR) edge termination type for SBDs were developed at Institut NEEL - CNRS. Figure 3.17 shows the successive steps realized to form the FFR SBDs. Before the lithography process, diamond surface was terminated by oxygen using vacuum ultraviolet light (VUV) system for 120 min [133]. The VUV system uses an Excimer 172 nm light source under 500 $mbar$ O_2 gas to form ozone (O_3) atmosphere. The ozone surface treatment removes the surface conductive layer (hydrogen (H)-terminated surface) and replaces it by O atoms. Carbonyl (C = O), hydroxyl (C - OH), ether (C-O-C) and peroxy

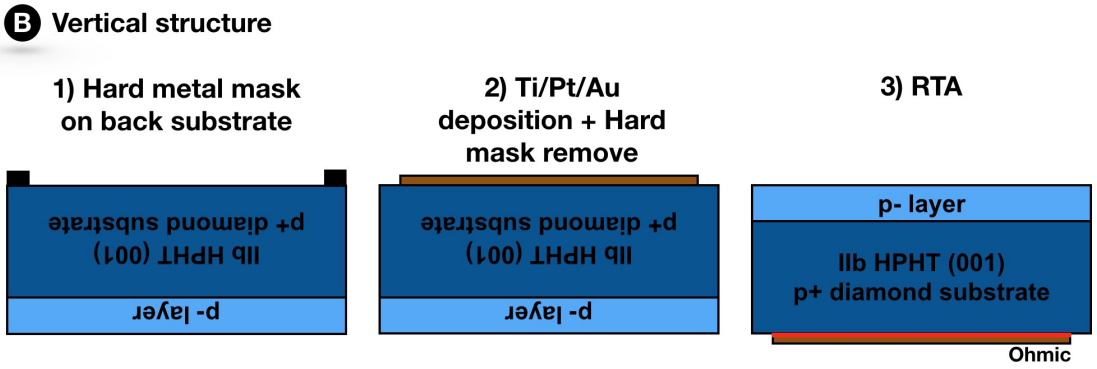

Figure 3.14: Steps for Ohmic contact fabrication in case of vertical structures. TiC (represented in red) is formed at the last step after RTA. Ohmic fabrication for the vertical structure is light as compared to the pseudo-vertical structure.

(C-O-O-C) species are formed at the surface [129, 134]. E-beam lithography process was then done using a NanoBeam nB5 system which permits a delicate and complex design. Mr. Thierry Crozes from Nanofab - Institut NEEL (CNRS) realized this part. Finally, FFR SBDs and simple SBDs were obtained by evaporating Mo(30 nm)/Pt(20 nm)/Au(20 nm) layers using lift-off method and VUV/O_3 used again to passivate the surface. Same steps are required for the pseudo-vertical structure to fabricated the devices.

3.3.3.2 Field Plate Oxide Edge termination

Similar to FFR-SBDs fabrication, diamond active layer surface was first exposed to a UV light (185 nm, 3.7 mW.cm^{-2}) under ozone atmosphere for 18 hours. Using this system, Umezawa *et al.* reported an oxygen surface coverage of more than 90% verified by XPS [135]. The stable oxygen termination and contribute to uniform interface quality between metal/p-type diamond and aluminum oxide (Al_2O_3)/p-type diamond [136]. The next step was the field oxide deposition by the lift-off method. 5 nm Al_2O_3 deposited by atomic layer deposition (ALD) followed by 995 nm of lanthanum aluminum oxide ($LaAlO_3$) deposited by physical vapor deposition (PVD) sputtering were realized at MANA (NIMS - Tsukuba) with Dr. Jiangwei Liu's help. Then, a second photolithography process was done and, field plate (FP) SBDs, as well as simple SBDs, were obtained by lift-off technique after Mo(500 nm)/Pt(50 nm)/Au(100 nm) stack evaporation. Figure 3.18 exhibits the main steps realized to fabricate the FP SBDs with a final top view picture of the devices.

3.3.3.3 Unterminated Schottky Gate electrode

The term unterminated here signify that no particular architecture like edge termination was used. After Ohmic source and drain formation, the samples were exposed to UV/O_3 treatment during 18 hours (as described in the previous part). Second ozone treatment was realized after photholitography process following by Mo(30 nm)/Pt(30 nm)/Au(100 nm) layers deposition and a lift-off of the resist. Finally, a third and final ozone treatment was performed.
The ozone treatment was performed every time a reactive ion etching (RIE) was used to

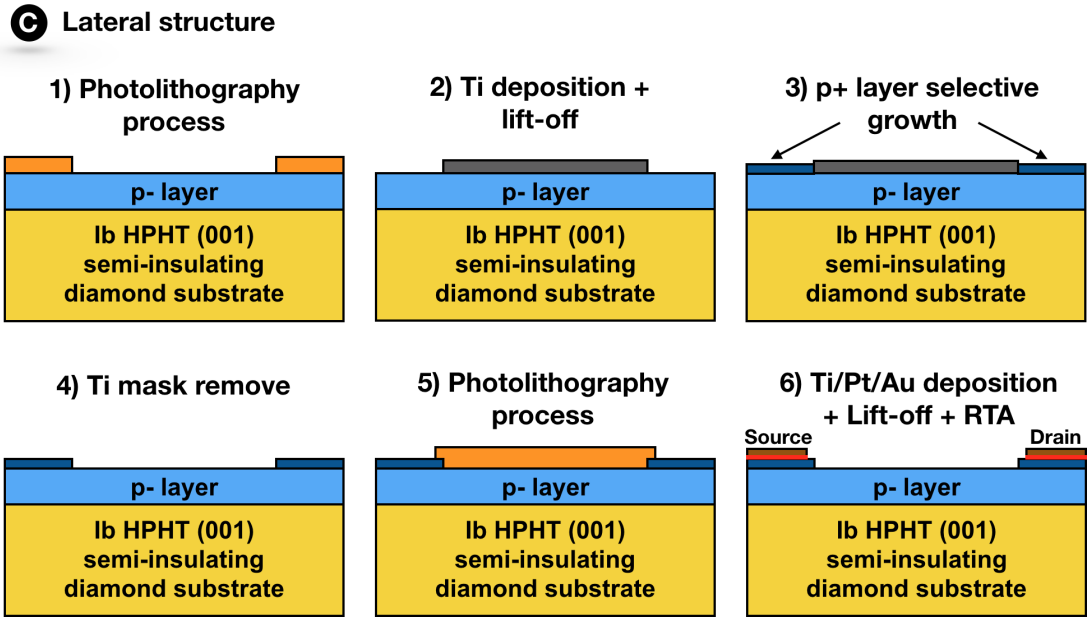

Figure 3.15: Steps of top Ohmic contact fabrication for lateral structures achieved by selective growth of a heavily doped boron layer.

remove the residual resist. The O_2 plasma used in RIE may physically attack the diamond surface and hence change the passivation. To be sure of the O-terminated surface a UV/O_3 was used again.

Device	ID	$[B]_{p+}$ $[cm^{-3}]$	t_{p+} $[\mu m]$	$[B]_{p-}$ $[cm^{-3}]$	t_{p-} $[\mu m]$	Technique	Structure
Schottky Barrier Diodes							
FFR	#1	2×10^{20}	1	1×10^{16}	0.95	SIMS	pv-SBD
	#2	2×10^{20}	Subst	1.58×10^{16}	1.5	C-V	v-SVD
FP	#2	2×10^{20}	Subst	1×10^{15}	5.4	SIMS	v-SBD
Field Effect Transistors							
MESFET	#1a	1×10^{21}	0.2	8×10^{15}	1.5	SIMS	Planar
	#2a	1×10^{21}	0.07	7×10^{15}	3.2	SIMS	Planar
RB-MESFET	#1b	1×10^{21}	0.2	8×10^{15}	1.5	SIMS	Planar
	#2b	1×10^{21}	0.07	7×10^{15}	3.2	SIMS	Planar

Table 3.2: Device fabricated parameters summary for FFR-SBDs, FP-SBD, MESFETs and RB-MESFETs.

3.4 Experimental setup

This last section deals with the characterization tools used to measure and analyze the fabricated devices. Facilities settled in France and Japan were complementary for this work. First, platforms for electrical characteristics are presented, then a powerful analysis technique to map the electric field and extract semiconductor material parameters is described.

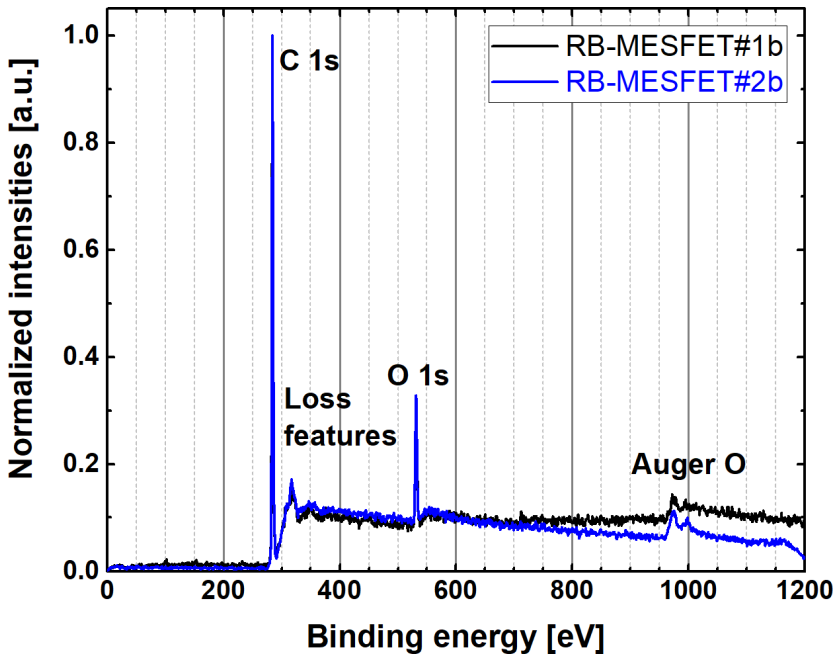

Figure 3.16: Full range XPS analysis results showing no Ti (454.7 eV) or TiC (281.8 eV) peaks on RB-MESFET#1b and #2b

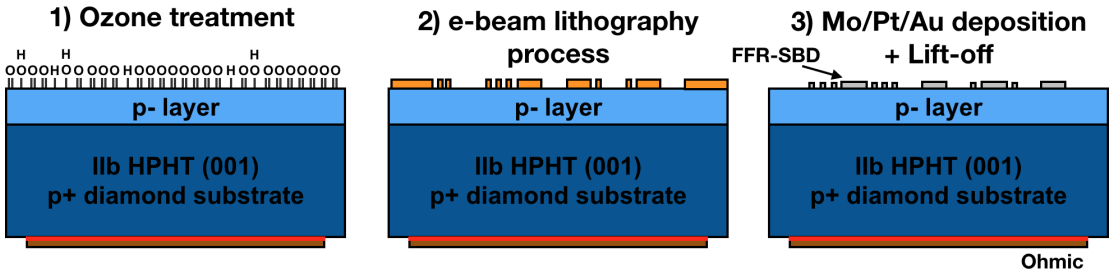

Figure 3.17: Floating field rings edge termination Schottky barrier didoes fabrication steps. SBDs with various rings and no rings were designed.

3.4.1 Electrical measurement facilities

The samples fabricated and summarized in table 3.2 were characterized by several source measurements units (SMU) settled in different places (sometimes for the convenience of the equipment). Figure 3.20 contains the pictures of all probe stations used in Japan and France. A single channel Keithley SMU 2601A and a double channel Keithley SMU 2636A were used for current-voltage I(V) measurements for both Schottky diodes and FETs at AIST Tsukuba facility (3.20-a). The mobile probes (manually controlled) were set in a small chamber allowing a high vacuum level. The SMU 2601A in DC measurement mode has a bias ranging from -40 V to 40 V was used to characterize device forward state because of its 1 A maximum current capability and a current detection limit of 10^{-12} A. The bias range of the SMU 2636A is ± 200 V, and its current detection limit is 10^{-12}. Reverse states of some devices were performed at AIST - Kansai (3.20-b). The Agilent B1505A was used selecting a high voltage SMU (HVSMU) with 10 nA current range (current resolution

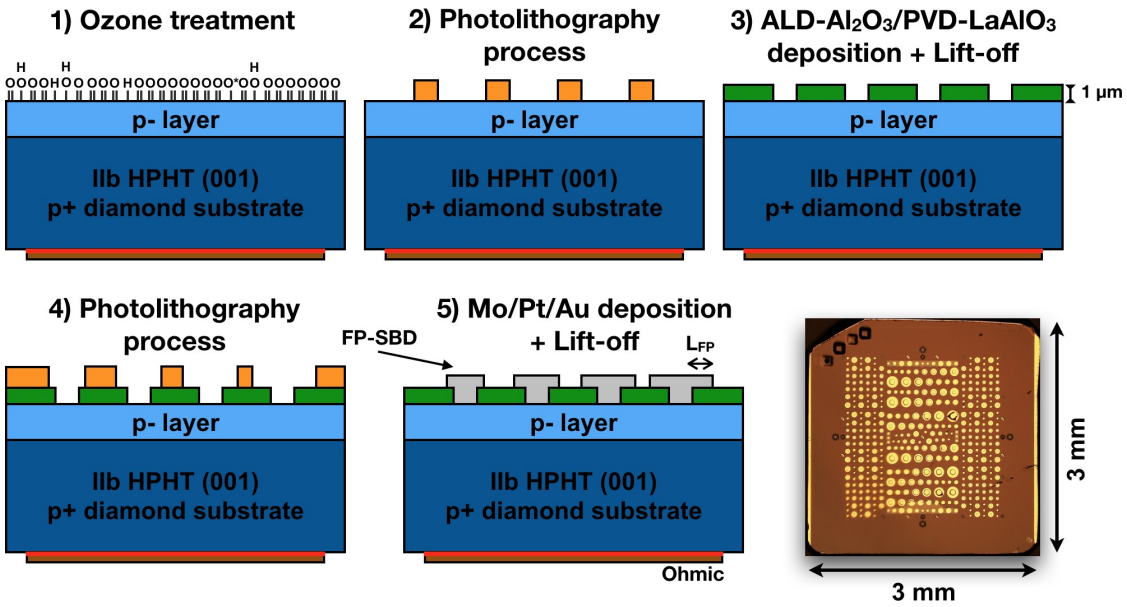

Figure 3.18: Schematic cross-sectional field plate Schottky barrier diode process fabrication main steps and a picture of the final sample is represented.

of 100 fA) and a high power SMU (HPSMU) with 1 nA current range (current resolution of 10 fA). The bias voltage range of the HVSMU is ± 3kV. The tips were moved manually and adjusted with the help of a camera.
The electrical characterizations performed at Institut NEEL - France (Figure 3.20-c) were done in a home-made vacuum probe station using a Keithley SMU 2636A and a single channel SMU 2410 for I(V) measurements and a ModuLab XM MTS Solartron analytical system for capacitance - voltage C(V) characteristics. The SMU 2636A is similar to the one described earlier. The SMU 2410 was used to investigate rectifiers in reverse state because of its 1100 V of maximum applied bias voltage and 10^{-9} of current detection limit. Regarding the Solartron, the typical AC signal frequency is ranging from 1 Hz to 1 MHz (with a possible DC bias ranging from -8 V to 8 V), and the AC signal voltage amplitude was 30 mV. The AC signal frequency can go as lower as 10 μHz. The probes station uses a binocular microscope and a piezoelectric micro-manipulators for accurate control of the tips when approaching the metal contact. The temperature of the samples was controlled by a Linkam cooling system (ranging from -196°C to 600°C) using liquid nitrogen flowing across the sample holder. When devices exhibited reverse characteristics with blocking voltages more than 1100 V, CARAPACE platform at the G2Elab was used (Figure 3.20- d). The vacuum probe station uses 6 manually movable tips, one of which is reserved for optical pulse excitation. An Agilent B1505A for high voltage electrical measurement is installed. All measures were realized under vacuum and dark to avoid electrical arcing and/or premature breakdown and effects due to optical excitation, respectively.

3.4.2 Electron beam induced current technique

Electron beam induced current (EBIC) is one of the most useful semiconductor analysis technique to investigate junctions, defects or even minority carrier properties. It is also used to study regions of high electric field in the material and device failure owing to its

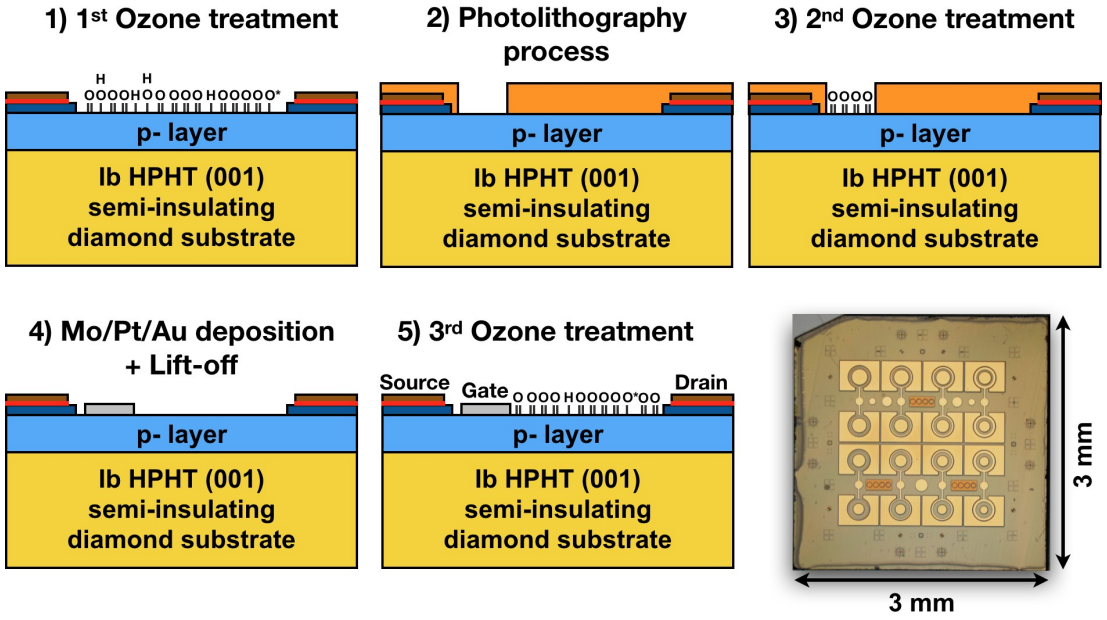

Figure 3.19: Schematic representation of the process fabrication steps realized to obtained MESFETs. A picture of one final sample is shown.

spatial resolution [137]. The EBIC system uses a scanning electron microscope (SEM) chamber and either a current pre-amplifier or a current collector apparatus. Similarly to cathodoluminescence (CL), EBIC is based and depends on the creation of electron-hole pairs (EHPs). Figure 3.21 shows a picture of the CL and EBIC system. CL and EBIC system use the same SEM chamber. The carriers, EHPs, are generated when the electron beam from the SEM hits the material. An energy E_{EHP} of 13.1 eV is required to generate one EHP in diamond material [138]. The accelerated electrons impinge with the lattice electrons of the sample and create EHPs. The number of EHPs generated per second ΔN can be estimated from the following equation [40]:

$$\Delta N = \frac{I_{eb}}{q} G \tag{3.2}$$

with

$$G = \frac{V_{acc}}{E_{EHP}} (1 - \beta) \tag{3.3}$$

where I_{eb}, V_{acc}, q, E_{EHP} and β are the electron beam current, the acceleration voltage, the elementary charge, the energy to generate one electron-hole pair, and average fraction of the primary electron energy beam leaving the sample by backscattering, respectively. Assuming a sphere-shaped carrier generation distribution, then the density of the excess minority carrier per second can be expressed as follows:

$$\Delta n = \frac{\Delta N}{V} \tag{3.4}$$

where V is the interaction volume. An estimation of the interaction volume is calculated from Kanaya-Okayama diameter D_{K-O} defined as follow [139]:

$$D_{K-O} = \frac{27.6 \times A \times (V_{acc})^{1.67}}{Z^{0.89} \times d} \quad [nm] \tag{3.5}$$

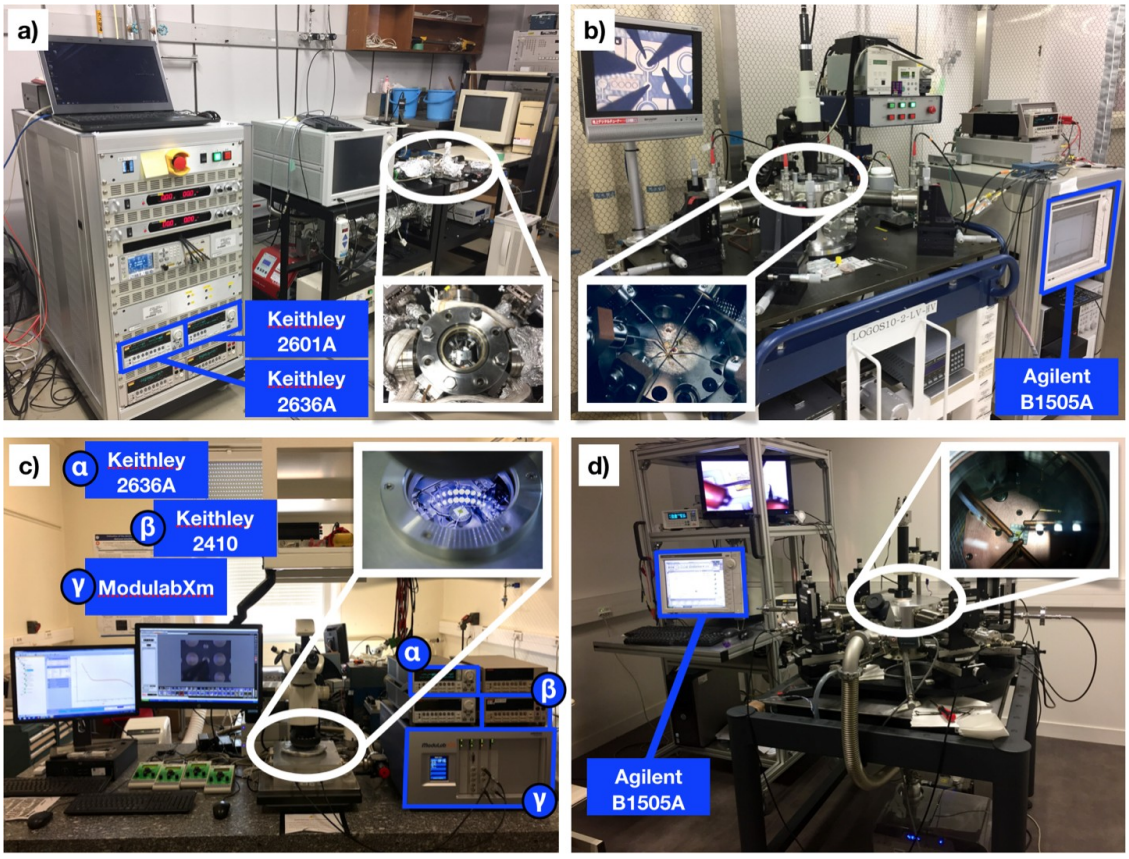

Figure 3.20: Pictures of the different probe stations used for the forward characterization at a) AIST - Tsukuba & c) Institut NEEL and for reverse characterization at b) AIST - Kansai & d) G2Elab using CARAPACE platform.

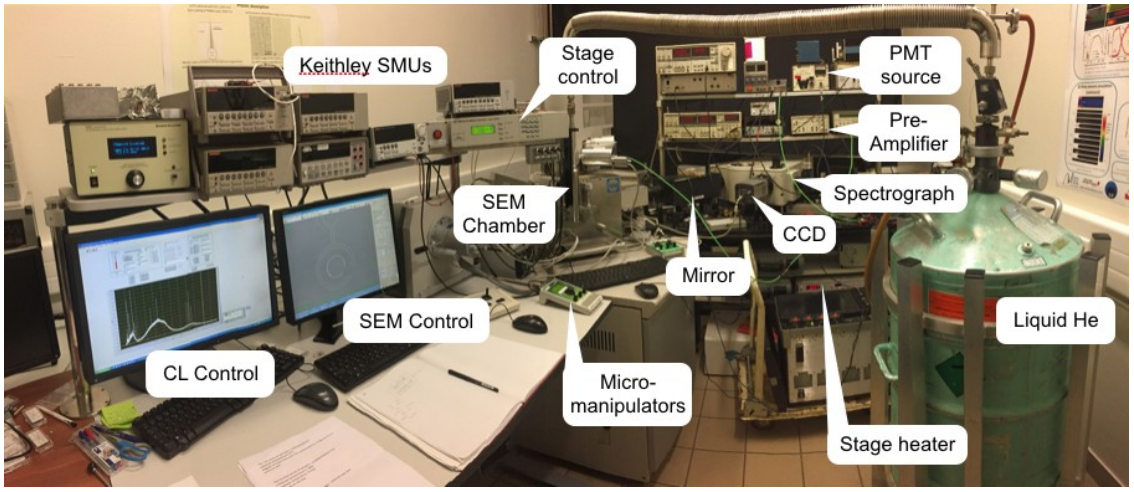

Figure 3.21: Pictures of CL and EBIC system used. CL, *Cathodoluminescence*; *EBIC, Electron beam induced current*

where A is the mean atomic mass in g/mol, Z mean atomic number and d the material density in g/cm^3. Finally, with the minority carrier (electron) lifetime τ_e, the mean excess minority carrier density is derived:

$$n_{ex} = \Delta n \times \tau_e \tag{3.6}$$

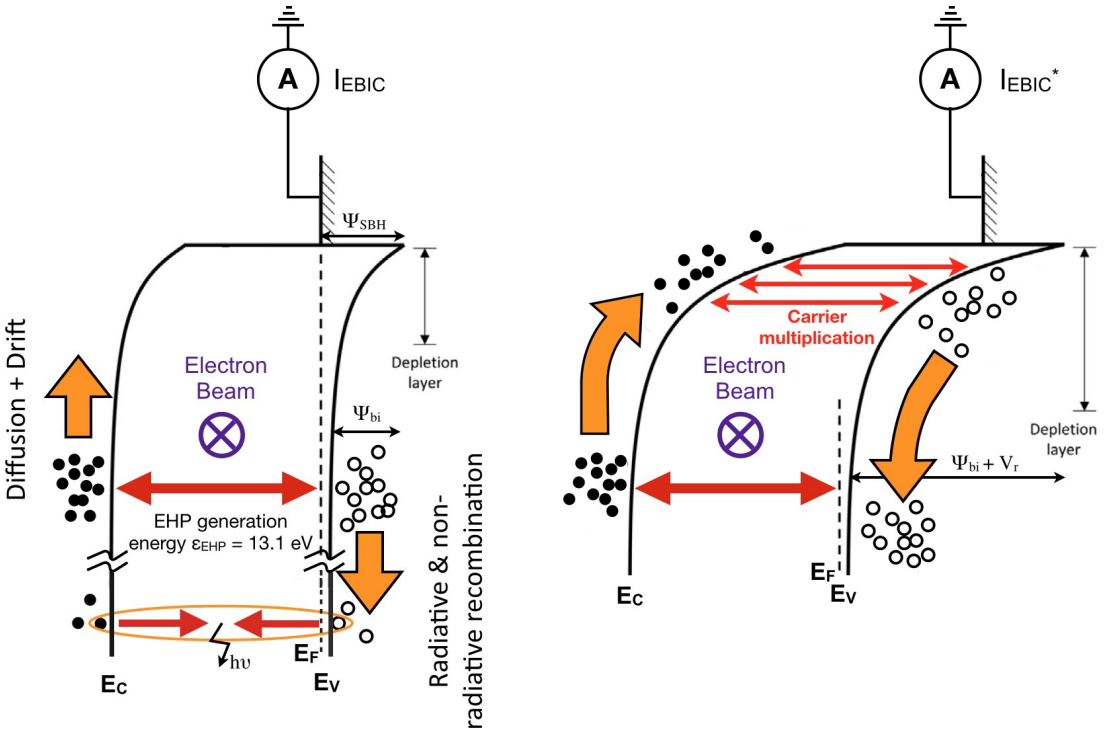

Figure 3.22: Band diagrams of diamond with Schottky junction at equilibrium (left) and under reverse bias (right). Electron beam induced current is based on minority carrier collection and cathodoluminescence on radiative (photon) recombination.

If the sample contains an internal electric field - generally located at the junctions, the EHPs will be separated and will drift at opposite directions. At equilibrium, in the case of a Schottky contact (metal/semiconductor junction) with a p-type semiconductor, the built-in potential created (due to Fermi level alignment and hence the downward band bending) will block the holes and electrons will be collected allowing a minority carrier electrons current flow. Basically, from the built-in potential, the electric field inside the depletion region is 30 - 100 kV/cm which is high enough to diffuse and drift them towards the Schottky contact. Under high reverse bias at the Schottky contact, a high electric field take place in the depletion layer, and the electrons within this layer are multiplied because of the increasing velocity of the carriers that generate other carriers and so on, as represented in figure 3.22. The collection of the minority carriers can be a direct process (”true EBIC”), and hence a Keithley 6485 picoammeter is used. A second method, much more visual, consists in amplifying the minority carrier current collected using a pre-amplifier Stanford Research System (Model SR570) and then through a computer monitor reproduce the EBIC image. Figure 3.23 is a schematic of the EBIC experimental setup. The amplifier discretizes the current in a gray level (16 bits corresponding to 65536 gray levels) within ± 1 V range of the apparatus video card. With the amplifier, it is possible

to set the sensitivity and the offset to have a good EBIC image contrast. From the obtained EBIC image profile intensity, one can go back to the EBIC signal (”true EBIC”) by applying the following expression

$$I_{EBIC} = a_{sens}\left(\frac{2 \times Intensity}{65536} + 1\right) \_ I_{offset} \tag{3.7}$$

In equation 3.7, $((2 \times Intensity)/65536) - 1$ gives the voltage value in the video card range ($\pm$ 1 V). The term $a_{sens}(((2 \times Intensity)/65536) - 1)$ convert the voltage value in current (sensitivity in A/V). And finally, an offset current I_{offset} (in A) set in the amplifier is subtracted to found the EBIC signal.

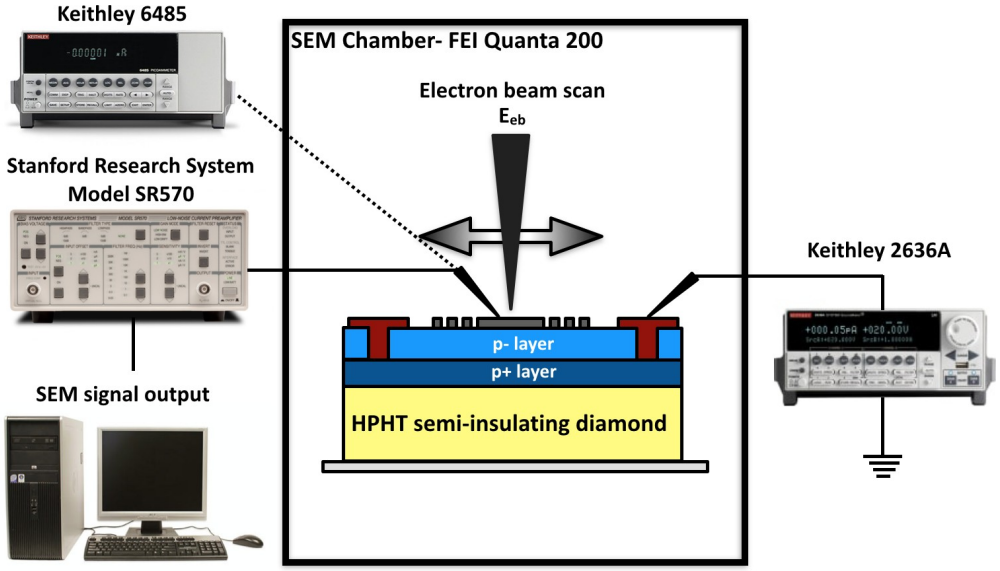

Figure 3.23: Schematic of the experimental setup used for electron beam induced current analysis. The collection of minority carrier is done either with a Keithley 6485 picoammeter which provides a better resolution of the measured current or through a pre-amplifier which offers an image with the gray level. As an example, FFR SBD was represented for the device under test. FFR SBD, *floating field ring Schottky barrier diode*

When carrier multiplication occurs at high reverse bias, the collected current I^*_{EBIC} can be described as [140]

$$I^*_{EBIC} = \frac{GI_{eb}}{1 - \int_0^d a(x)dx} \equiv \frac{GI_{eb}}{1 - a\exp(-\frac{b}{E}).d} \tag{3.8}$$

where d is the effective distance traveled by the electron and a the impact ionization parameter in Chinoweth’s equation form.

3.5 Conclusion

In this third chapter, we have seen the full road of the device from growth to characterization going through fabrication. Precision, rigor and an extremely clean environment

are required for successful device fabrication. Characterization tools help to understand the failure step that can be solved. The limited size of diamond wafers makes device fabrication challenges. As compared to Si wafers were the size varies from 1 to 12 inches, diamond wafers to be used for power devices have a maximum size of 1x1 cm^2. One of the powerful analysis technique was also described. Electron beam induced current method can be used to detect dislocations, for device failure, to visualize the surface electric field distribution and to extract material physical parameters.

Chapter 4

Edge termination Schottky barrier diodes and metal-semiconductor FETs evaluation

Diamond is becoming an active research area with its potential to be used in high voltage and high thermal applications. The promising results obtained on unipolar devices [3, 11, 31, 6, 65], make Schottky diodes (rectifiers) and metal-semiconductor field effect transistors (switches) the perfect candidates to be commercialized and integrated into commutation cells.
This chapter is focusing on the results and discussions on floating field ring and field plate edge termination Schottky diodes as well as on the switch metal-semiconductor field effect transistor. Electrical characterizations together with electric field mapping will be discussed.

4.1 Edge termination Schottky barrier diodes

For high voltage devices, edge termination structures play an extremely crucial role in improving the device breakdown voltage. A device without edge termination will reduce the breakdown voltage and hence the breakdown field to below the ideal limit due to a premature breakdown at the main Schottky contact edges because of an electric field crowding [141, 46]. To be able to reach the best device performance, the electric field crowding at the edges has to be minimized.

4.1.1 Limits of a non-optimized diode

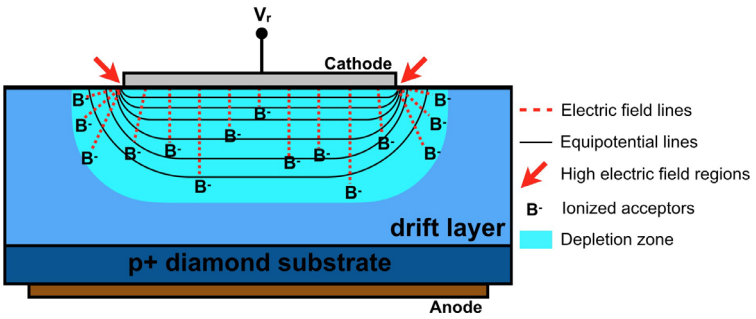

Figure 4.1: Schematic cross-sectional view of a simple Schottky diode under high reverse bias. Electric field crowding occurs at the edges.

A surface architecture always limits a diode operation in reverse state. Figure 4.1 schematize the main phenomenon happening in the reverse condition. When applying a reverse bias (positive) at the diamond Schottky electrode, majority carriers (holes) are pushed away from the cathode leaving a zone where only ionized acceptors remain. The area created is the depletion region. Under the cathode, parallel to the contact, equipotential lines are formed inside the drift layer. According to Poisson's Equation, perpendicular to the equipotential lines, electric field lines (EFL) are also formed, and they link the cathode and the ionized acceptors. The created depletion region expands inside the drift layer in depth and laterally.

Furthermore, EFL between the edge of the cathode and lateral ionized acceptors are also formed. Mainly because of the high density of EFL, an electric field crowding phenomena occurs at the electrode edge. Therefore, the electric field is uniform under the center of the main contact and higher at the border. The ratio between the edge electrode electric field

peak E_{peak} and the center electrode maximum electric field E_{max} generally varies between 1.5 and 2.5.

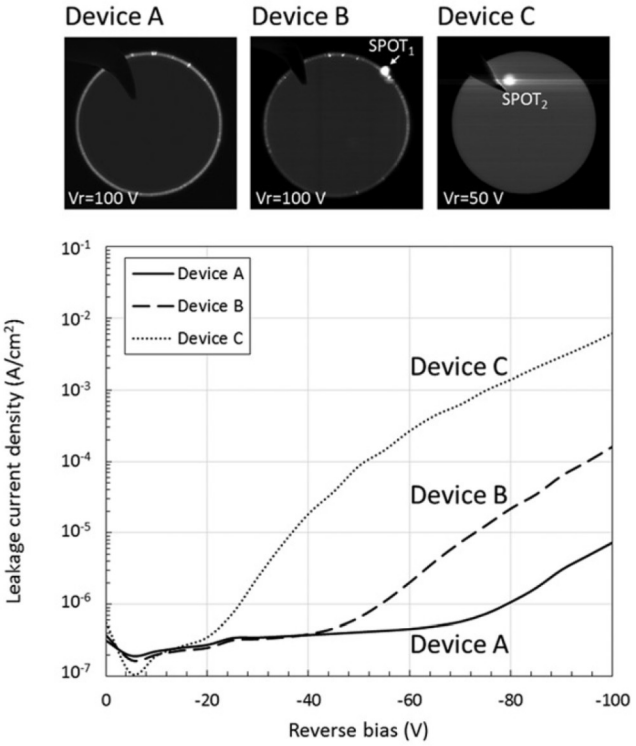

Figure 4.2: Leakage current densities for devices A, B and C with corresponding EBIC images. Hotspots induce leakages of the devices [105].

Simulation work showed that the leakage current occurs at the edge where the electric field is maximal. Recently, Umezawa *et al.* showed that the electric field crowding does not degrade only the breakdown voltage but also contributes to the increase of the leakage current (Hotspots) [105]. In fact, for the first time, precise observation of the defects and field enhancement on leakage current enhancement was performed using EBIC method (figure 4.2). Defects and presence of hotspots affects a lot the leakage current and hence the device operation. The appearance of the spots could be related to processing fabrication, especially the lift-off technique that induces roughness due to metal tearing. When observing the regions where hotspots were seen, a roughness of the electrode edge was also noticed for the most cases. The presence of the bright spot inside the Schottky electrode could be linked to killer defects that increase the leakage current [142].

A predictable phenomenon when the device reaches its limit is represented in a typical scanning electron microscope (SEM) image in figure 4.3. After a breakdown of the device, sometimes the electrode is damaged, and metal melting seems to occur in some located areas. In this case, we talk about a hard breakdown — Basically, the electrode damages when the temperature gets high enough to evaporate the metal (principally due to high current density flows in a tiny area).

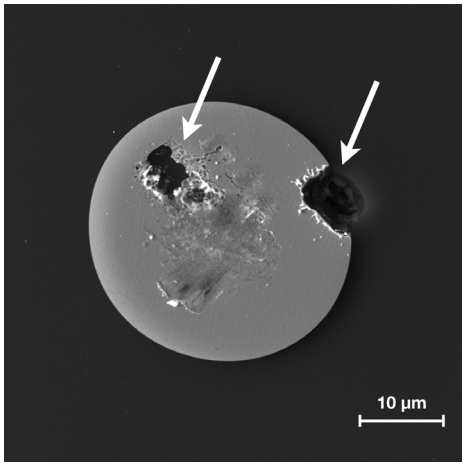

Figure 4.3: Typical diode damaged after a hard breakdown

4.1.2 Floating metal field rings structure

In this part, we will discuss the first floating field rings (FFRs) edge termination SBDs fabricated using diamond material. Edge termination FFRs are well known in Si, GaN or SiC communities. Before developing buried p+ guard rings as edge termination using ion implantation technique [143, 51], devices were first studied using deposited surface floating metal rings [39, 52, 50, 144]. Two approaches are presented. For the first one, FFRs ET-SBDs were fabricated with different ring distances and rings numbers following Sarah Rugen's simulation work. Then, a second approach based on obtained first results, a newly designed structure was investigated and proposed. FFR#1 was fabricated based on Sarah Rugen's work [49]. Details of the samples can be found in chapter 3.

4.1.2.1 Principle work and design of floating field rings SBD

Floating field rings structure reduces and can even suppress the electric field crowding at the edge of the main Schottky contact. In fact, as explained above when a reverse bias is applied the depletion expands laterally with a width $w \propto \sqrt{V_r/N_A}$.
For a floating ring positioned closest enough to the main junction, the laterally expanded depletion layer overlap the ring. The ionized acceptors at the mid-way between the main contact and the ring create an intimate EFL. This sharing of EFL between the edge of the main contact and the first ring diminishes the crowding of the electric field at the main contact edge and permits to apply an even high reverse bias on the diode cathode. Using the same principle to the second, the third and the nth ring, the highest reverse bias can be applied to the diode. This highest reverse bias will be now limited by the intrinsic material properties and not the architecture.
Figure 4.4 is a 2D TCAD Sentaurus simulation study done by Sarah Rugen a Ph.D. student of Bremen University (German) [49]. It shows a comparison of simulated electric field distribution at the diamond/metal junction for both a vertical SBD with (w/) 8 rings and without (w/o) field rings. A simple SBD, without FFRs, has a peak electric field at the edge of the main contact of 9.5 MV/cm and a maximum electric field a the center of the cathode of about 5 MV/cm. While using FFRs, the peak electric field is reduced to about 6.3 MV/cm. An optimized structure is when the peak electric field of the main contact edge and the peak electric field at the edge of the last ring have a nearly equivalent

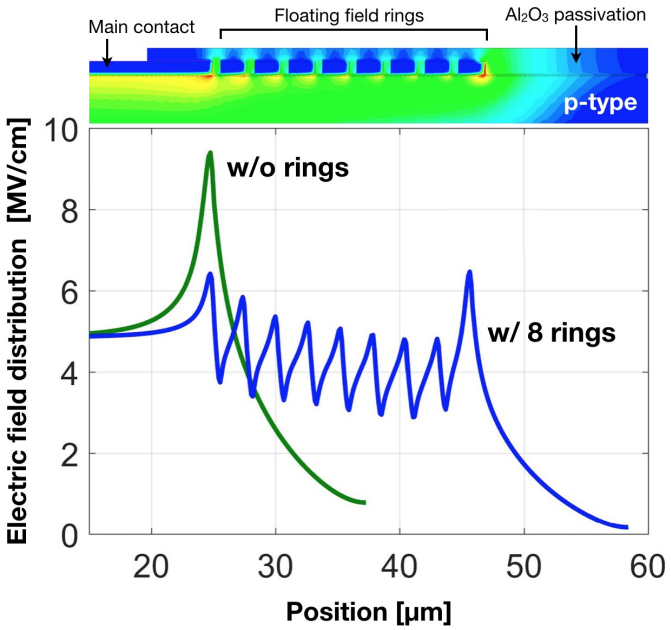

Figure 4.4: Surface electric field as a function of position for an SBD w/o floating ring and w/ 8 floating rings. Electric field peak is reduced when FFR is used [49].

value. An investigation of the distance of field rings and number of rings has led to figure 4.5. When the gap between two consecutive rings gets too large, the rings do not relax the electric field at the edge of the main contact edge, and hence the peak electric field is shifted. Conversely, when the gap gets too short, the peak electric field reduces at the main contact edge and increases at the edge of the last ring if the number of the ring is insufficient. A trade-off between the distance of field rings and number of rings exist.

Based on this simulation work sample FFR#1 was fabricated with SBDs without rings and with different ring number and gap. Table 4.1 encloses the details of these devices. The width of the field rings was kept constant and equal to 2 μm. Experimental results on the effectiveness of FFR on SBDs will be discussed in the following paragraphs.

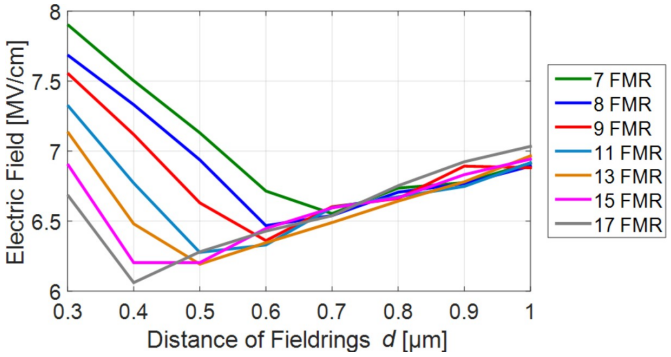

Figure 4.5: Maximum electric field peak as a function of the distance of field rings for various ring numbers. For each fixed ring number it exists an optimized field ring distance [49].

Schottky diodes FFR#1						
Device type	A	B	C	D	E	F
Gap W_s [nm]	None	800	600	500	400	300
Ring number	None	4	9	13	17	21

Table 4.1: Information on the type of FFR Schottky diode fabricated

4.1.2.2 Electric field mapping

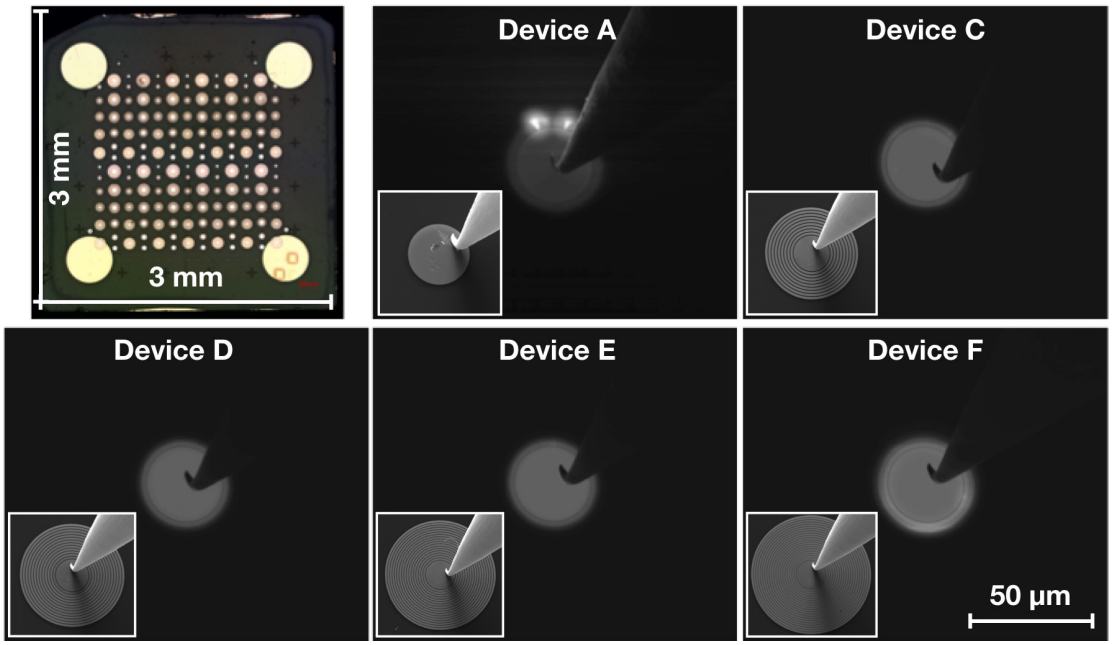

Figure 4.6: Top view of the fabricated sample FFR#1 and EBIC images of devices A, C, D, E and F under 120 V applied reverse bias and corresponding SEM images. The contrast of the EBIC images was enhanced for a better view. The main contact diameter is 30 μm.

To correctly understand the introduction effect of ET FFR, EBIC analysis was undertaken. Reverse bias of 120 V was applied to the different devices listed in table 4.1. Figure 4.6 is a picture of the sample fabricated and EBIC images of various devices with their corresponding SEM images. The main contact has a diameter of 30 μm. These images give information on surface electric field distribution. Device A is a simple SBD without FFR and from device C to F are the SBDs with FFR reported in table 4.1. For device C, D and E, only the first ring is bright. Whereas, for device F, the two first and a beginning of the third ring is observable.Therefore, we will focus on devices A (w/o FFR) and device F (FFR with 300 nm for the distance between the field rings and 21 rings).

The EBIC profiles of device A and the device F are shown in figure 4.7. The profiles were obtained by analyzing EBIC images reported in figure 4.6. Device F exhibited the best EBIC profile compared to the others FFR-SBDs. As the EBIC technique is based on the collection of minority carrier induced by the presence of electric field, the observed EBIC signals give information on surface electric field position and distribution. The collected total EBIC signal is higher when the beam is located above the Schottky metal compared to a beam positioned on a free diamond surface.

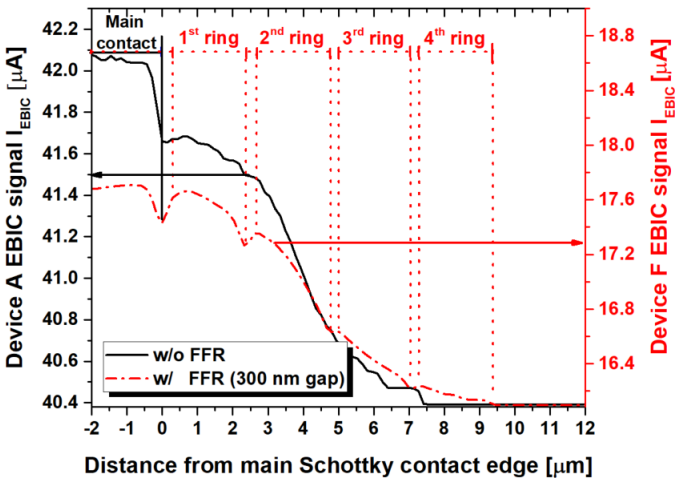

Figure 4.7: EBIC signal as a function of the distance from the edge of the main Schottky contact extracted from EBIC images of device A and F shown in figure 4.6. The signal includes a dark current observed when the beam was located far away from the contact, in the neutral region.

As a consequence of the Schottky metal thickness and the high electron beam energy (30 keV), parts of injected electrons penetrate the diamond beneath the contact inducing an EBIC current in the diamond electric field. Other electrons are also backscattered or reflected. The absorbed electrons by the metal contribute to a current flow. Additionally, a dark current was observed far away from the junction, in the neutral region. The effect of field rings is visible in figure 4.7. The EBIC intensity extends over long distances from the contact edge, suggesting that the electric field is distributed over a wider area. However, this field extension is only significant over the first 4 rings. The field vanishes at the 5th field ring which makes the 17 following rings unimportant. This weak improvement could be associated with a non-constant potential underneath each ring. This potential variation that reduces field extension might be related to the non-uniform interface as suggested by the variation of the ideality factor n [**?**]. A non-optimized ring spacing may also be the cause. For this doping concentration and active layer thickness, spacing less than 300 nm could further improve the surface electric field distribution of the device. Indeed, for the same applied reverse bias (120 V), FFR-SBDs with spaces greater than 300 nm exhibited a surface field distribution $\leq$ 2 rings as seen in figure 4.7. Based on the EBIC analysis of sample FFR#1, ring spacing influences surface field distribution, but the ring number induces no influence. Indeed, two peaks should be observed for an optimized ring spacing: one at the main Schottky contact and the other at the last ring edge. It suggests that the structure is still non-optimized. Therefore, the lowest ring spacing (300 nm) needs to be reduced since the peak EBIC signal remains located at the main Schottky edge.

A post-fabrication 2D simulation study was performed using TCAD Sentaurus finite element software and implementing the FFR#1 sample details. Figure 4.8 presents the electric field distribution within the FFR SBD when using 500 nm and 300 nm gap W_s. Solid lines represent the equipotential distribution for a reverse bias applied of 220 V. The width of the rings is 2 μm, similar to the fabricated one. The FFR SBD with W_s of 500 nm (figure 4.8-a) exhibits a peak electric field concentration at the edge of the main contact edge as compared to the FFR SBD with W_s of 300 nm (figure 4.8-b) were the concentration of the electric field is located at the same time at the edge of the main

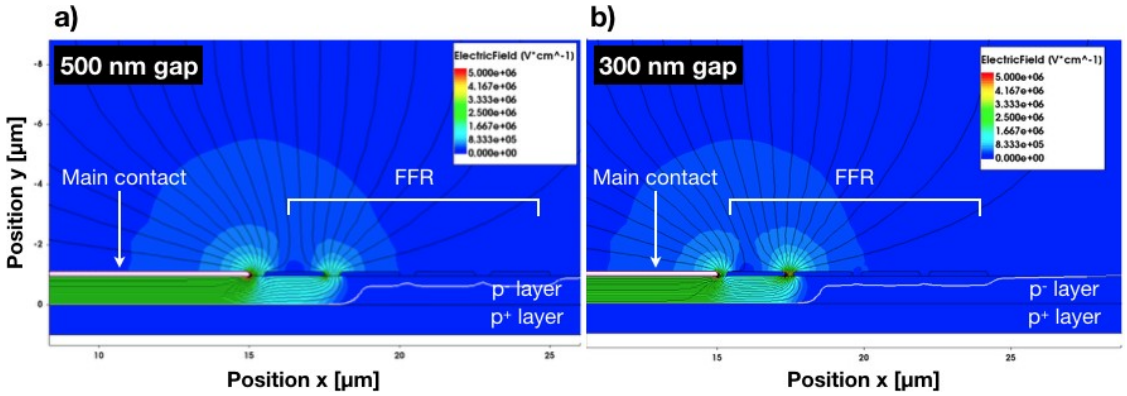

Figure 4.8: Comparison of 2D electric field distribution simulated by TCAD Sentaurus between (a) an FFR#1 SBD with a gap W_s of 500 nm and (b) a gap W_s of 300 nm. Simulation made with 4 rings of 2 μm width each. The applied reverse bias was 220 V.

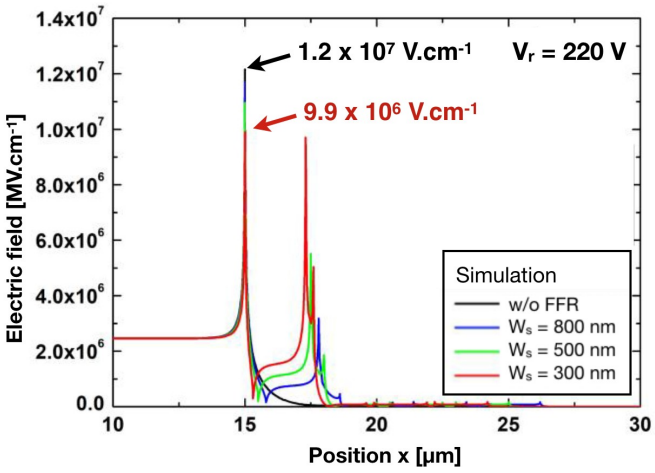

Figure 4.9: 2D surface electric field profile at the metal/p-type junction for SBD without FFR and FFR SBDs with 800 nm, 500 nm and 300 nm gap W_s. The applied reverse voltage was 220 V. The electric field peak reduces when decreasing the gap to 300 nm.

contact and at the edge of the first FFR. Figure 4.9 encloses the maximum electric field profile at the metal/diamond junction as a function of the position for different devices. Position x = 15 μm represent the edge of the main contact. The electric field peak for an SBD without FFRs reaches 12 MV/cm and is located at the main contact edge. When using FFR with 300 nm gap between the field rings, two peaks appear, one at the edge of the main contact and the second one at the edge of the first field ring. The peak electric field at the edge of the main contact is reduced to 9.9 MV/cm, and the peak electric field at the first field ring reaches 9.8 MV/cm. For gap W_s in between no FFR and 300 nm gap, the peak of the electric field is greater than 10 MV/cm. The use of FFRs ET slightly improves the relaxation of the electric field crowding at the main contact edge when using 300 nm gap between the field rings. However, only the first ring seems efficient enough. The same remark was made for the experimental part in figure 4.7.

Implementing the doping concentration (1×10^{16} cm^{-3}) and the thickness (1.5 μm) of sample FFR#2's drift layer in TCAD simulation, new results have been obtained. Sample

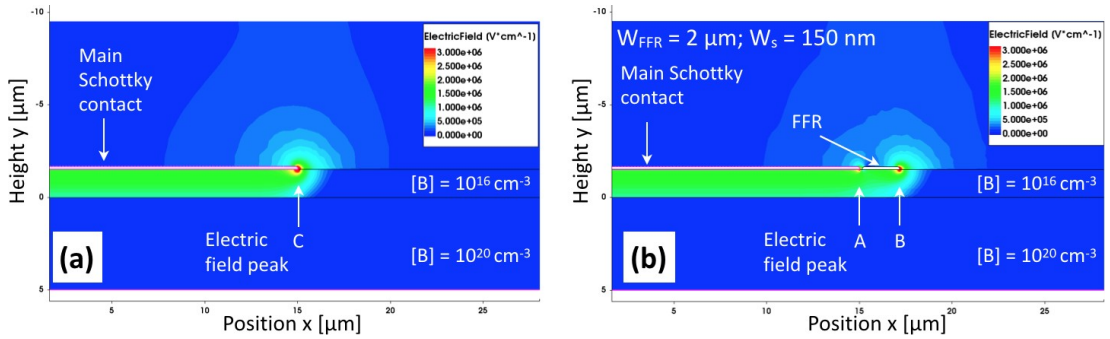

Figure 4.10: Simulated 2D electric field distribution at a reverse bias of 200 V for (a) a simple SBD and (b) an FFR-SBD with 1 ring of 2 μm width and 150 nm spacing for sample FFR#2.

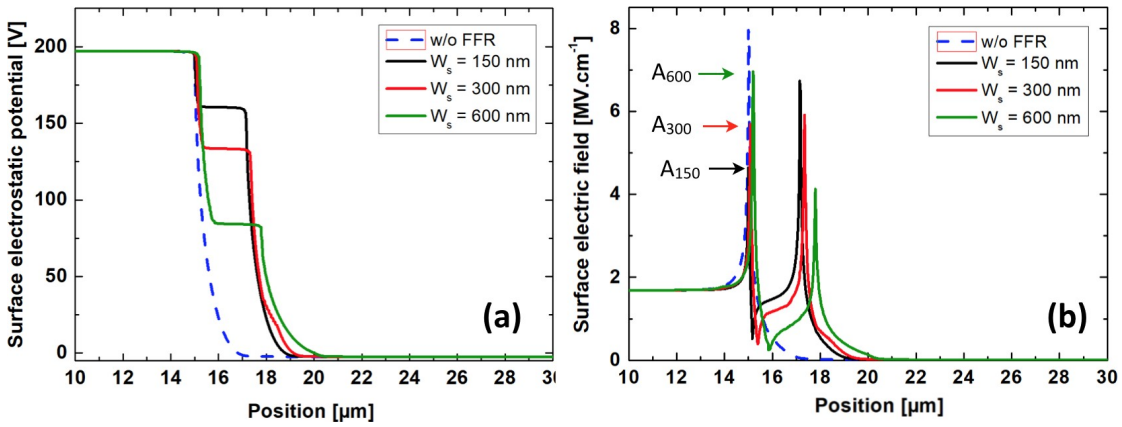

Figure 4.11: Diamond (a) surface potential and (b) electric field for FFR#2 device simulated for simple SBD and FFR-SBD with 150 nm, 300 nm, and 600 nm ring spacing.

FFR#2 has almost the same doping concentration as sample FFR#1 and a slightly thicker layer (about 500 μm). Indeed, the change in sample parameters may change the depletion region distribution. However, it should not be massive changes. Since the effectiveness of the first ring was observed in figure 4.8, only one ring was designed with 2 μm width for a gap of 600 nm, 300 nm, and 150 nm. The device fabrication process becomes a real challenge for large devices and narrow gap such as 150 nm. Figure 4.10 shows the electric field distribution results obtained for simulated sample FFR#2 for simple SBD and FFR-SBD with 150 nm gap between the main contact and the ring. A device without FFR edge termination exhibited one peak electric field (labeled ”C” in figure 4.10-a) and as expected a device with one floating ring 2 peaks. Both simulated devices are presented for an applied reverse bias of 200 V. The observed steep decrease of the surface potential (figure 4.11-a) of a device without edge termination implies a high electric field of about 8 MV/cm (figure 4.11-a). In figure 4.11-b, where a surface electric field plotted as a function of the position, we can see the importance of having a right gap. In fact, when the ring has a large gap (600 nm) the maximum peak electric field appears at the edge of the main Schottky contact (labeled ”A”) and when it has a short gap (150 nm) the maximum peak electric field appears at the outer edge the ring (labeled ”B”). An optimized gap (300 nm) has a maximum peak electric field less than 6 MV/cm appearing in ”A” and

"B" position. The simulation performed for both FFR#1 and FFR#2 did not take in consideration the surface potential or the fixed charge at the metal/diamond interface that can change the depletion region and hence the electric field distribution which may end by a non-optimized gap. In that, it is not straightforward to compare the simulation results and the obtained experimental results.

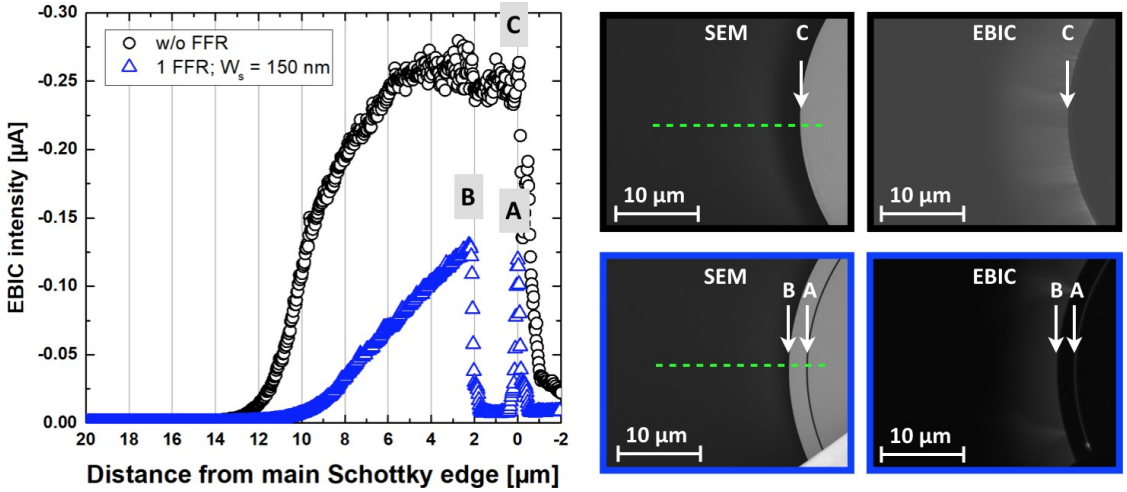

Figure 4.12: EBIC intensity as a function of distance from the main Schottky edge for a simple diode and a diode with one ring. The effectiveness of edge termination is highlighted here. The EBIC intensity, which is a consequence of the presence of electric field, drops by about 50% when using a ring spacing of 150 nm.

Figure 4.12 shows the EBIC line scan of an SBD without edge termination and an SBD with 150 nm ring space and 2 μm ring width. A 5 keV beam energy was set so that the metal thickness (50 nm) of the Schottky electrode prevents the beam from passing through. In that, only qualitative information on the edge electric field is observable. The figure shows SEM images together with a corresponding EBIC images. The applied reverse bias is 60 V. The use of a floating field ring edge termination with a gap of 150 nm reduces about 50% the EBIC intensity at the edge of the diode. The effectiveness of floating field rings is here pointed out. A closer view of the EBIC line scan exhibit a peak EBIC intensity slightly higher at the outer edge of the ring as compared to the peak at the main Schottky contact for the FFR-SBD with a spacing of 150 nm. It is in correlation with what was observed by simulation in figure 4.11-(b).

4.1.2.3 I(V) characteristics

• Forward state

Figure 4.13 shows typicals obtained characteristics for the on-state. SBDs with and without FFRs having a main contact diameter of 30 μm and 50 μm were fabricated for FFR#1 and 50 μm and 100 μm for FFR#2. Figure 4.13-a is a typical linear plot of the current-voltage obtained for SBDs without FFR and with 300 nm gap (Device type F) for both diodes with 30 μm and 50 μm main contact diameter. An irregularity on the linear part (Ohmic regime) of all the devices was noticed. A change in the slope reflects the irregularity, and hence in the diode serial resistance since $\Delta I = \Delta V / R_s$. From figure

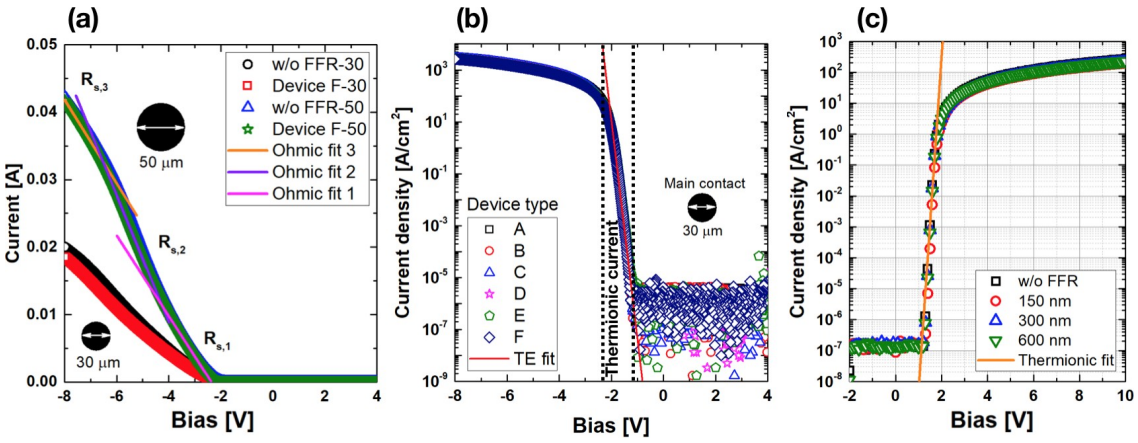

Figure 4.13: Forward characteristics are showing (a) a comparison between a 30 μm and a 50 μm device diameter for devices w/o FFR and w/ 300 nm gap and 21 rings. (b) Current density for all type of devices with main contact diameter of 30 μm for FFR#1. (c) Current density as a function of bias applied on Ohmic contact for FFR#2 for the different SBD fabricated. The main Schottky contact has a diameter of 100 μm

4.13-b&c, a specific on-resistance $R_{ON}S$ of 1.8 mΩ.cm^2 and a maximum current density J_{max} of 2830 A.cm^{-2} at -8 V were obtained for all the characterized devices for FFR#1. Diodes fabricated on FFR#2 exhibited a maximum current density J_{max} of 300 A.cm^{-2} at -10 V. Fitting the curves by thermionic emission model [145], the ideality factor and the saturation current were extracted. The ideality factor n varies from 1.5 to 2 for devices on FFR#1 and was about 2.5 for devices fabricated on FFR#2. This variation was independent of the device type (simple SBD or FFR-SBD). The interface quality at the metal/diamond junction is not homogenous and may affect the reverse state. From the saturation current, a Schottky barrier height (SBH) about 1.7 eV and 1.5 eV were found for FFR#1 and FFR#2, respectively.

- **Non-uniform doping profile**

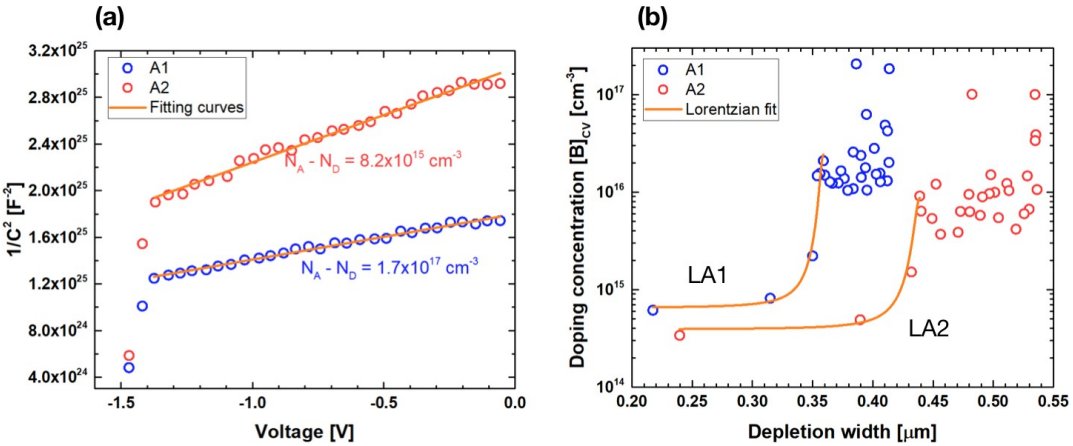

Figure 4.14: (a) Doping concentration extracted by C(V) measurement for two devices positioned far away from each other. (b) Doping profile fitted by Lorentzian equation. A non-uniformity of the doping is noticed.

Although the doping concentration was firstly extracted by the SIMS method, the obtained results (boron doping concentration and profile) give information for only a localized region and not the whole sample. To investigate the noticed diodes serial resistance change, a C-V measurement was performed on several devices of the same architecture (device type A) to have an idea about the doping profile of the drift layer. Here, two simple SBDs labeled A1 and A2 and localized far away from each other are shown as an example. SBD A1 and A2 were situated at the sample center and close to the sample border, respectively. Non-uniform doping was noticed as seen in Figure 4.14-a. The boron doping concentration was varying between 7.6×10^{15} cm^{-3} and 1.7×10^{17} cm^{-3} using C(V) method. The doping concentration was not uniform in the xy plane (parallel to the diamond surface). A straightforward 1D calculation has allowed extracting the boron doping profile as a function of the depletion width and hence the depth of the drift layer. Additional to the uniformity discovered in the xy plane, uniformity of the boron doping concentration was also noticed in the z-axis (depth of the p^- layer). Figure 4.14-b is the boron doping concentration as a function of the depletion width for the A1 and A2 SBD. The boron doping concentration distribution on beneath the diodes is equivalent for both regions. The doping concentration is almost constant (3-7 $\times$ 10^{14} cm^{-3}) for a certain depth, then it increases sharply up to 1-2 $\times$ 10^{16} cm^{-3}. Then, a second increase occurs up to 2 $\times$ 10^{17} cm^{-3}. The depth at which the doping concentration is constant is not uniform for the entire sample. For example, it is more frofound for A2 region than for A1 region with about 80 nm difference. Both of the doping concentration profiles can be fitted by a Lorentzian distribution as represented in figure 4.14-b by LA1 and LA2. The equation used is of the form

$$[B]_{CV} = [B]_{surface} + \frac{2A}{\pi} \frac{w}{4(x - x_c)^2 + w^2} \tag{4.1}$$

where $[B]_{surface}$, A, w and x_c are boron doping concentration near the surface, the area under the curve, the full width at half maximum (FWHM) and depth at which [B] is maximum, respectively. This non-uniformity of the doping concentration extracted by C(V) measurement could be related to the growth condition or to the surface interface charge which influences the depletion region.

• Reverse state

Figure 4.15-a exhibits the limit operation of the different FFR SBDs in the reverse state. A compliance on the current density of 10 A.cm^{-2} was set which corresponds to about 300 for rectification ratio. This decided limit was considered as the breakdown of the device since the leakage current will reach the current densities close to the forward state. All the Schottky diodes (w/ or w/o FFR) had high leakage current, and furthermore, avalanche breakdown was not observed. At 250 V, all the presented SBDs have reached the compliance except the device F where its current density is about 0.3 A.cm^{-2}. Based on the assumed limit for BV, device F seems to have a BV greater than 250 V (>2.6 MV.cm^{-1}). Thereby, 300 nm spacing between the rings for FFR SBDs is the most optimized distance among of the studied ring-to-ring distances in FFR#1. However, the obtained >2.6 MV.cm^{-1} breakdown field remains lower compared to diamond breakdown field. It has been noticed that the curves have the same shapes following the thermionic field emission (TFE) mechanism but starting at different reverse bias values [146].

It has been noticed that the leakage current for small distances of the field rings was higher than the SBDs without FFR or with 800 nm gap. The lower the ring distance, the ear-

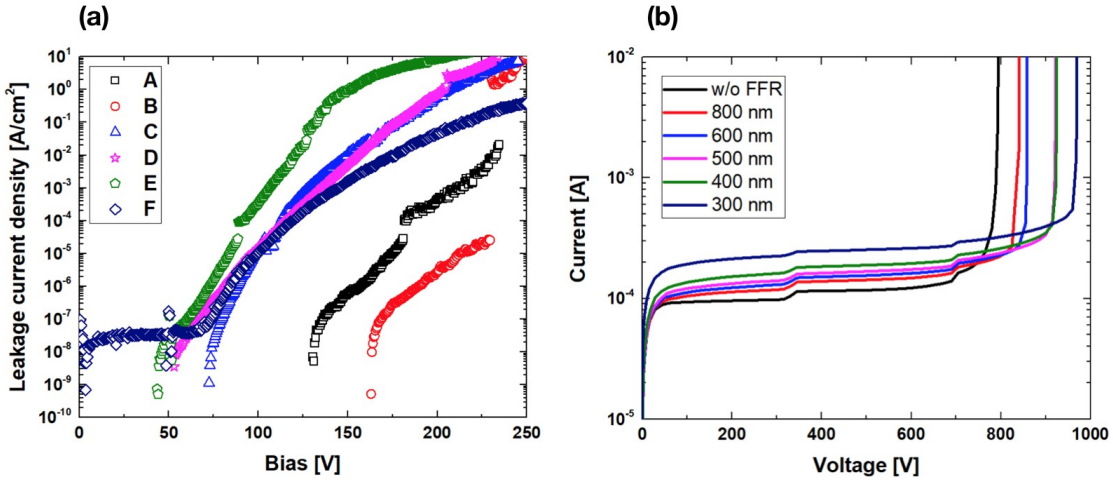

Figure 4.15: Reverse characteristics obtained (a) experimentally and (b) by simulation for all type of device fabricated on FFR#1. Leakage current increase and gap are linked. Simulation performed in Bremen University — acknowledgment to S. Rugen and Prof. N. Kaminski.

lier the leakage current starts to increase. Figure 4.16 summarizes the voltages at which the leakage current start to increase as a function of the field rings distance. When the leakage current of the device reaches 10^{-6} A.cm^{-2} the bias is reported in figure 4.16. The reverse leakages and their differences in the starting points could be due to arcing that takes place between the rings at high bias. Even by performing the measurements under vacuum, the reduction of the gap between the rings promotes the formation of a possible electric arc. The leakage current increase as a function of the gap was also observed in the simulated device (figure 4.15-b). Indeed, a simple SBD without FFR exhibited a leakage current lower than an FFR SBD. Moreover, leakage current tends to increase when the gap is reduced (for a fixed bias). Nevertheless, the highest breakdown was obtained by the FFR SBD with 300 nm gap. Passivation layer with oxide could take rid of the arcing and might improve the stability of the reverse leakage current. However, care must be taken with fixed charges that could change the surface potential of diamond. In the simulation results presented above, no fixed charge or diamond surface potential was implemented. These phenomena may change the electric field distribution at the surface of diamond and hence shift the optimized distance of field rings. Reverse state for SBDs fabricated on sample FFR#2 is shown in figure 4.17 were a simple SBD and an FFR-SBD with 150 nm gap. The BV of an unterminated Schottky diode was 82 V and the one with one floating ring and with 150 nm spacing was 125 V (0.8 MV/cm). An improvement of about 50% was obtained. The leakage current of SBDs fabricated on sample FFR#2 was more stable than the ones fabricated on FFR#1. Nevertheless, leakage current for fabricated devices may be originated from surface contamination due to process fabrication or hotspots as we will see it in the following section.

4.1.2.4 Device hard breakdown

Bright spots have been observed for almost all the characterized devices on both samples FFR#1 and FFR#2, as seen in figure 4.18. These hotspots are located at the edge of the

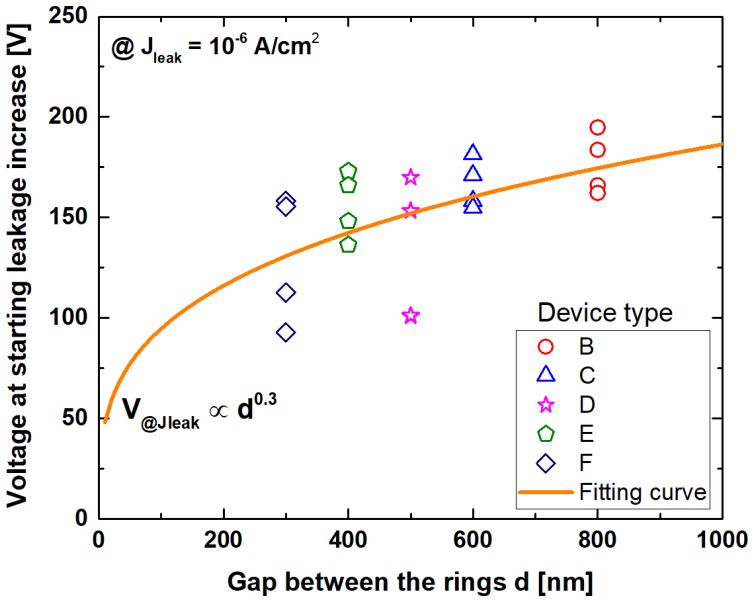

Figure 4.16: Influence of the leakage current increase by the gap between the rings for FFR SBDs characterized.

main Schottky contact and indicate regions with high electric field concentration. They are one of the causes of the high leakage current increase as discussed in 4.1.1, and hence are limiting the reverse operation of the device. A closer view of the metal edge indicated a high local roughness; indeed induced by the lift-off process used to fabricate the metallic contact, and that could produce a spike effect. Image 4.19 is a device that had shown extreme bright spot after the tip touched the edge of the main contact and changed the roughness. We can see in the zoomed SEM picture that there is metal removed from the electrode surface but still linked to the electrode (red dashed circle). The brightness starts from the apex of this metal formed. This apex is a discontinuity point where crowding of the EFL occurs and causes an extreme peak electric field, even more, higher than the main contact electrode edge. It is thought that similar phenomena happen with roughness $\leq 1\ \mu m$ at the edge of the main contact. The hotspots combined with the short distances between the rings enhance the arcing and hence imply a high leakage current increase that was observed in figure 4.15-a.

To go deeper in the analysis, we went up to the hard breakdown and damaged a few devices. Figure 4.20 shows EBIC pictures with hotspots location and SEM pictures with the located damaged places for device type C and D. The melting metal at the damaged regions (normal arrow labeled X) occurred after 1 W power applied on the devices. A correlation between hotspots and damaged regions was already observed [147]. Static EBIC measurements allow the premature breakdown location within the device. However, some devices had not shown melting metal damage at all the hotspots location. The dashed arrows (labeled X') shows one example of the undamaged region that exhibited hotspots. When applying a fixed reverse bias for a sufficiently long time, it has been noticed a change in spots location. Some bright regions were relaxed, and others created. It can be explained by the increase of the temperature at these located points that allow a change in the roughness at the edge. In fact, when the leakage current concentrates at a small region, the temperature becomes not negligible due to the high current density level. This rise of the temperature evaporate the metal at this precise point and hence smooth the

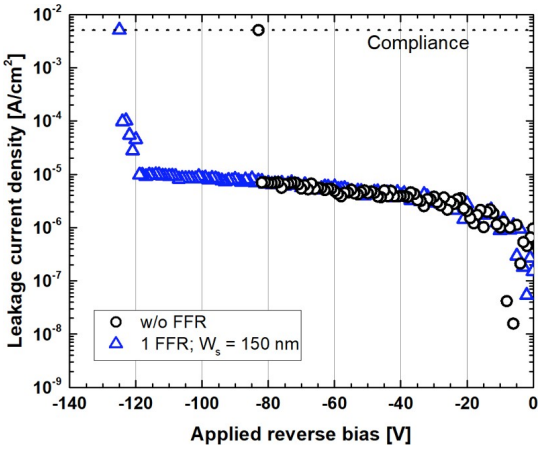

Figure 4.17: Leakage current density as a function of the applied reverse bias for FFR#2. The BV increased by about 50% when using a floating ring with a gap of 15, nm.

edge and slightly relax the electric field.

Further study is needed for a better understanding of this mechanism. Nevertheless, even if the hotspots limit the reverse operation of the SBDs, introducing FFR ET improve the surface field distribution. But, the process fabrication needs to be upgraded to avoid the roughness at the edge of the main electrode and hence a premature device breakdown.

4.1.3 Field Plate Schottky barrier diodes

A second edge termination investigated is the field plate (FP) structure. The field plate architecture uses a metal overlapping an oxide at the edge of the main Schottky electrode. The purpose, like other edge termination, is to diminish or suppress the electric field crowding that occurs at the main Schottky contact under high reverse bias. When designing the field plate termination structure, care must be taken to avoid premature breakdown at the oxide side. For that, the choice of the oxide, as well as the length of overlapping metal/oxide (FP length), are crucial.

4.1.3.1 Device design optimization

Figure 4.21 shows the 2D electric field distribution difference between an unterminated SBD and a field plated (FP) SBD. Models implemented to simulate the devices are described in chapter 2. When no FP oxide is used, a peak electric field appears at the main Schottky contact. However, when using an FP oxide, the depletion region spreads out in the oxide (and in diamond) contributing in the creation of two more electric field peaks (3 in total). These two additional electric field peak that appear relax the peak that is at the metal/diamond interface. Thus, for a fixed applied reverse bias the maximum electric field peak is decreased when using FP edge termination. Ikeda *et al.* [44] have reported on the importance of using a high-k material such as aluminum oxide (Al_2O_3) insulator for FP SBDs. An oxide of 1 μm was set for the simulation due to a process fabrication limitation. As explained in chapter 3, the oxide film obtained by lift-off technique become

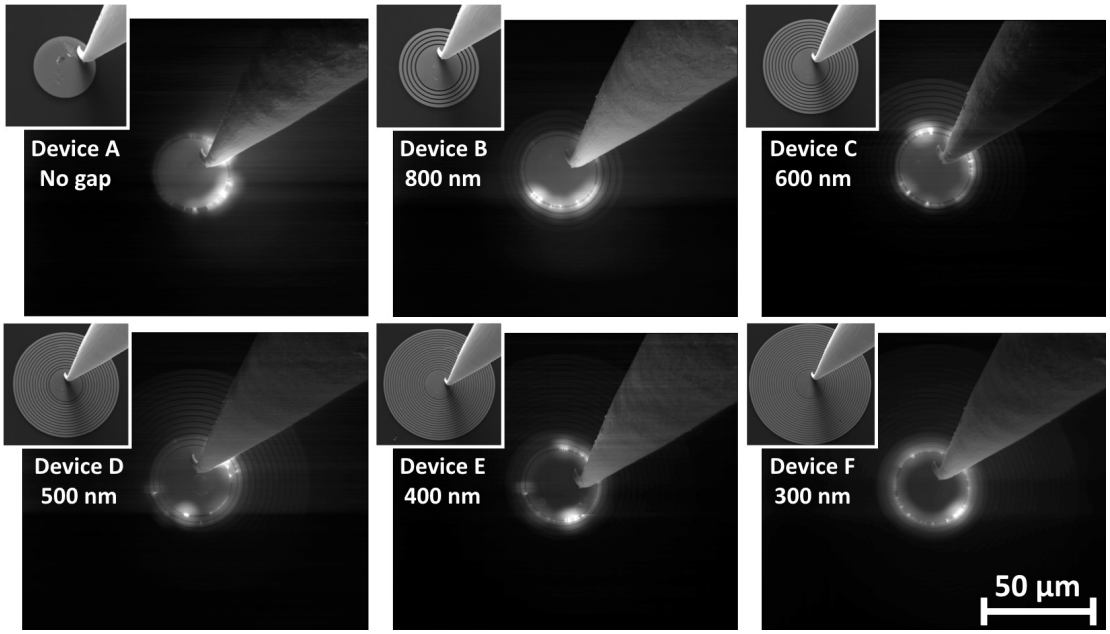

Figure 4.18: EBIC images of devices A to F and corresponding SEM images. Brighter localized regions (hotspots) observed in most of the characterized diodes.

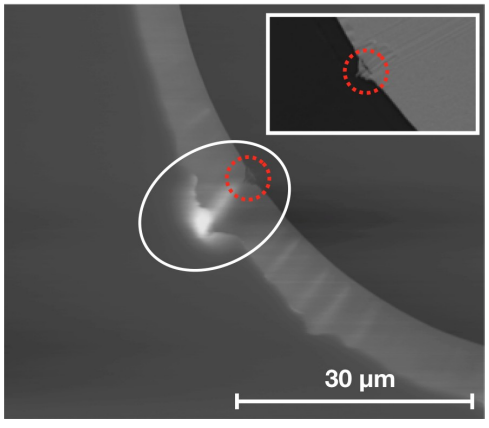

Figure 4.19: EBIC image of a simple Schottky diode with its SEM image. The hotspot region observed by EBIC is the place where an important roughness was noticed.

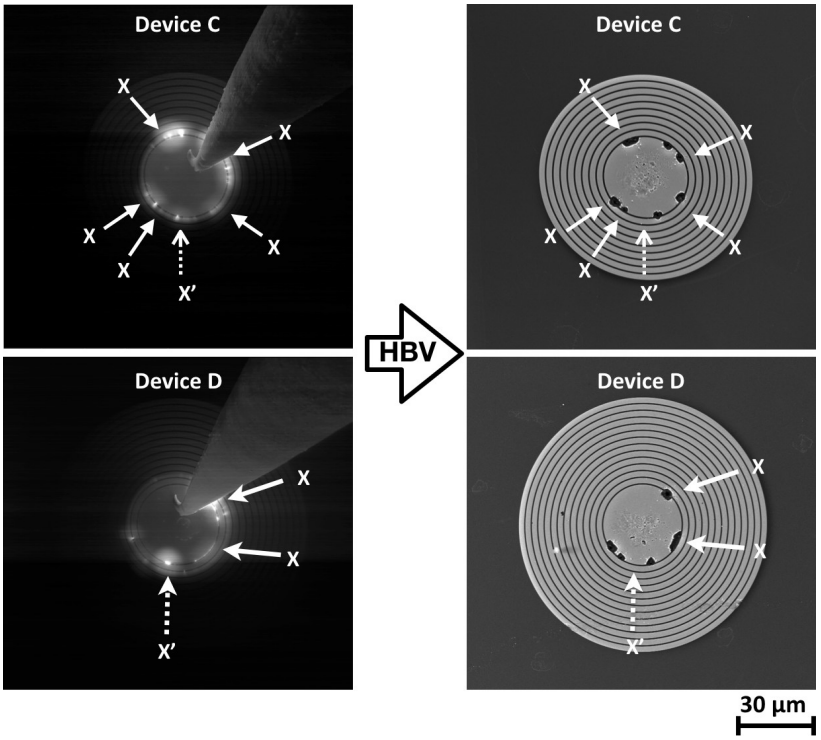

Figure 4.20: Typical EBIC images before and after hard breakdown voltage (HBV) of device C and D. After the HBV, regions where hotspots appeared were damaged. A significant leakage current flow may increase the temperature and evaporate the metal.

difficult to realize when the oxide thickness is increased. Therefore, the simulations were done by varying the FP length and keeping a constant oxide film.

4.1.3.2 Forward and reverse electrical characterization

Figure 4.22-a presents a typical forward current density as a function of applied bias for an SBD without (w/o) FP and SBDs with different FP lengths. The diodes characteristics have almost reproducible characteristics independent of the presence or absence of edge termination. The maximum current density is of about 300 $A.cm^{-2}$ at -8 V for all the diodes. The current exhibited a TE mechanism current with ideality factors ranging n from 1.6 to 2. The specific-on resistance extracted was 30 $m\Omega.cm^2$.

In figure 4.22-b, reverse states of the diodes are presented. The reverse characteristics using FP edge termination did not exhibite a huge improvement in the blocking capabilities. Only a maximum improvement of 34% was observed. The highest breakdown field was not exceeded 0.55 MV/cm. The leakage currents were too high leading to a premature breakdown. So far, no real improvement was observed depending on the FP length. Even though the leakage current acts like some TE and TFE leakage currents, a leakage current through the oxide remains possible. Additional to the mentioned process, the dislocations could induced by the leakage current originated from the heavily doped boron p+ substrate used. Temperature dependence up to 300°C of the reverse characteristics was also investigated, but no change was noticed.

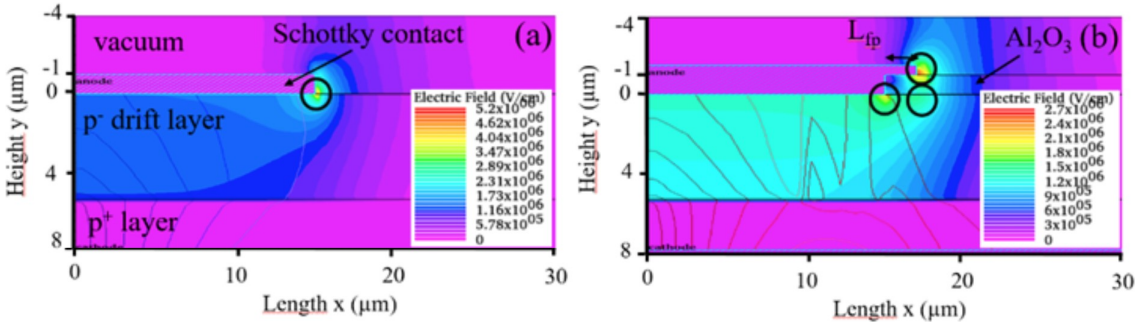

Figure 4.21: Comparison of the 2D electric field distribution between (a) a surface unterminated SBD and (b) a field plate SBD. Aluminum oxide (Al_2O_3) was used as field oxide. The circle shows the position of the electric field peaks.

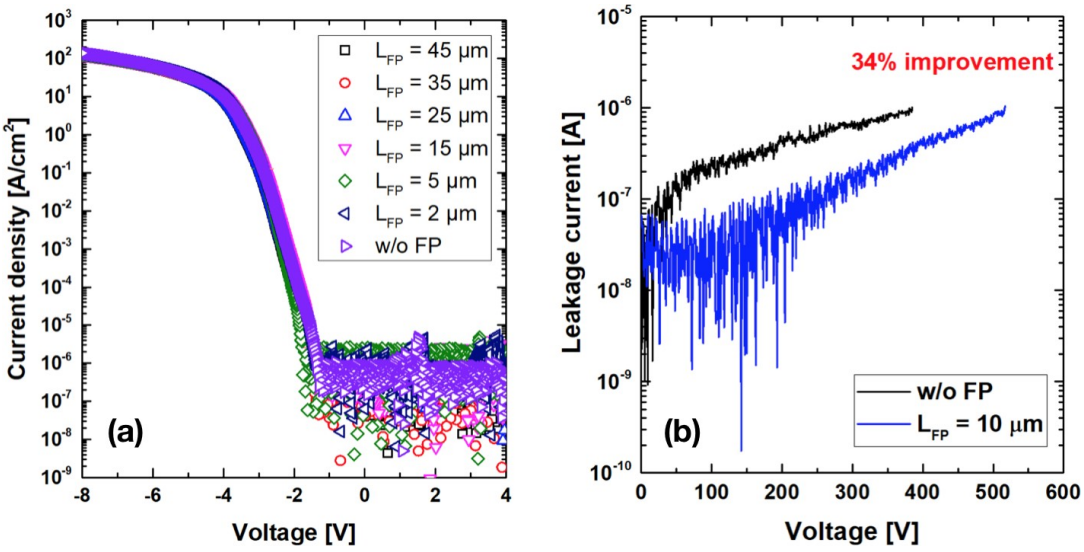

Figure 4.22: Typical (a) forward current density and (b) reverse leakage current as a function of the applied voltage for SBD w/o FP and SBDs w/ various FP lengths. The reverse characteristics exhibit only device w/o FP and w/ 10 μm FP length.

The device's hard breakdown was constantly taking place at the metal edge within the oxide film independently of the FP lengths. It is a damaging process. The reasons for these hard breakdowns at the oxide may be related to high leakage current through the oxide due to a poor oxide quality.

4.1.3.3 Qualitative electric field distribution

A qualitative surface electric field distribution is shown in figure 4.23. A reverse bias of 200 V was applied. An accelerated beam voltage of 30 kV was set. EBIC images and corresponding SEM pictures are presented. The SBD without (w/o) field plate exhibited one extended lateral region. As for the SBD with FP in some cases one ring and in some cases two rings were observed.The inner circle corresponds to the place where diamond metal and oxide are in contact. The outer circle is the edge of metal over the oxide. This

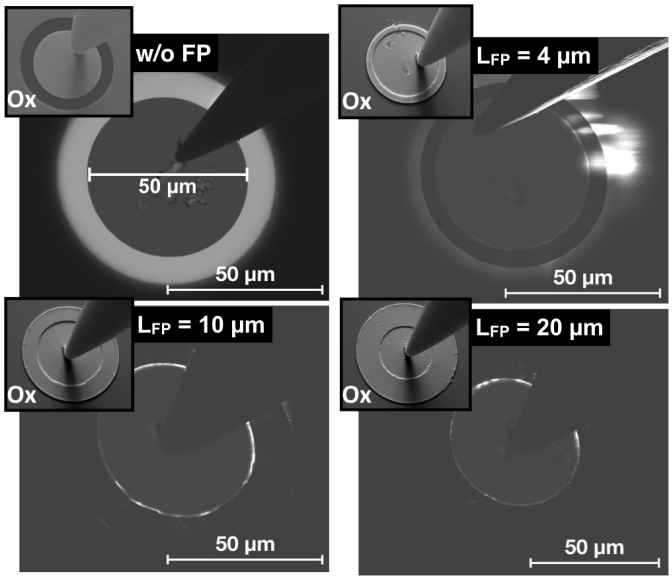

Figure 4.23: EBIC images obtained for a diode without field plate (FP) and diodes with FP edge termination. The field plates have 4 μm, 10 μm and 20 μm. The applied reverse bias was 200 V. Hotspots are observable also as well as a non-uniform inner circle.

figure shows the field plate length L_{FP}. When L_{FP} is too long then the outer ring does not appear meaning that the electric field is not relaxed (e.g., for L_{FP}=20 μm). Another unoptimized field plate length is presented when L=4 μm. We can see that the outer circle is brighter than the inner one. The maximum electric field peak is located in the oxide. However, a field plate length of 10 μm looks approaching the optimized length because two circles are present. The inner was brighter than the outer. Charging effect on the oxide was noticed during the analysis. The oxide thickness is 1 μm, and hence the oxide traps the electrons. For these reasons, an in-depth analysis of the field plate SBD were not investigated. Nevertheless, we see that the inner circle shows important oxide/metal edge interface roughness. In fact, the oxide film was obtained via lift-off lithography process. An improvement of the process fabrication is required.

4.1.3.4 Investigation of process optimization

Optimization of the process fabrication was started to be investigated. Instead of a lift-off of the oxide that stresses the thick oxide film, wet etching was selected. Figure 4.24 shows results obtained when an optimized wet etching is performed. Buffer hydrofluoric acid (BHF) was used.

4.2 Metal-semiconductor field effect transistors - MESFET

Metal-semiconductor field effect transistors have demonstrated a good capacity for potential radio frequency application [148] as well as for high voltage [11]. In this second section of the chapter, results on transistor fabricated will be presented and discussed. Transistors for high voltage application in order to get high BV were investigated.

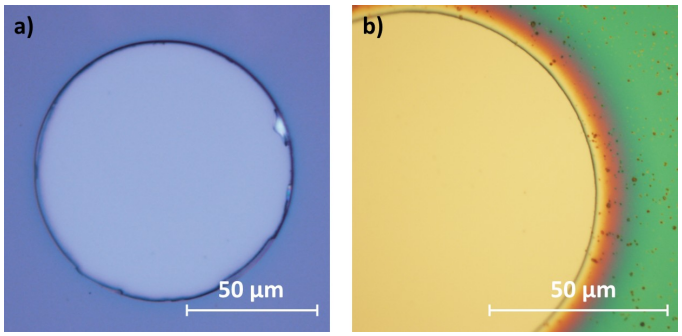

Figure 4.24: (a) Oxide film results after the lift-off process. Important roughness was induced. (b) Oxide edge after wet etching explored. The edge is smoother, and a gradient of color appeared corresponding to a gradual increase of the thickness.

4.2.1 MESFET background

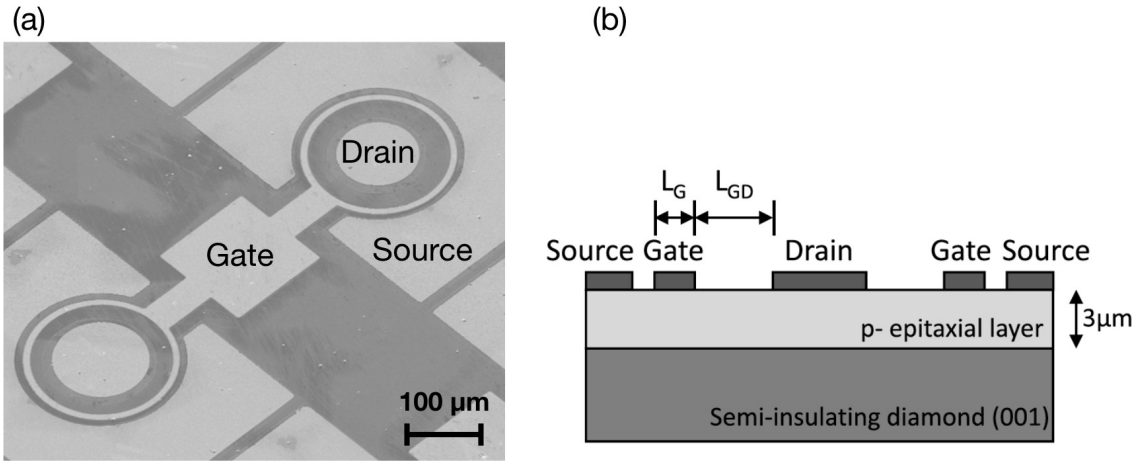

Figure 4.25: Top view and cross-sectional view of the MESFETs fabricated and reported by H. Umezawa *et al.* [11]

Diamond MESFETs were already investigated and reported for surface conduction through H-terminated diamond surface [149, 10, 58]. However, the first diamond MESFET properly bulk conduction was introduced by Umezawa et al. [11]. Figure 4.25 shows the top and the cross-sectional view of the reported diamond MESFETs. The ON-state current density obtained at room temperature (RT) was -0.06 mA/mm. Due to activation of acceptors at high temperature, the ON-state current density was multiplied by about 20.5 and reached -1,23 mA/mm at 300°C. Similarly, the estimated intrinsic transconductance at 300°C of 143 μS/mm was 4.9 times higher than that at RT. The highly resistive contact resistance limited the on-state current. As represented in the cross-sectional view, the source and drain were directly deposited on the lightly boron doped layer. Matsumoto [40] have summarized the specific contact resistances reported in the literature as a function of boron concentration and outputted the figure 4.26. The data include samples with and without post-thermal annealing (carbide formation). The essential step in achieving a low specific contact resistance is a well-controlled boron concentration, that is to say, a heavily doped boron layer under the Ohmic source and drain contacts. The dashed line

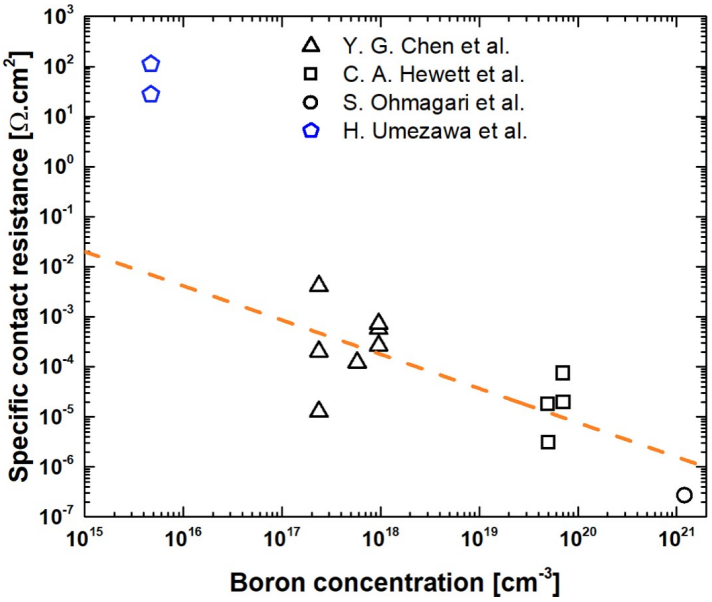

Figure 4.26: Optimized specific contact resistance as a function of boron concentration. Experimental data [150, 151, 152, 153, 11] extracted by Matsumoto [40]. Experimental data for H. Umezawa *et al.* [11] were added.

gives a trend of the curve evolution. The source and drain specific contact resistances (include parasitic resistance) estimated from the reported values of Umezawa et al. were added to compare them with the optimized one. The MESFET is limited by the contact resistance and a heavily doped boron layer under the source and drain contacts could improve the current densities. For the OFF-state, the transistor achieved ≈1.5 kV of breakdown voltage and has shown a gate to drain length dependency.

In this study, the fabricated MESFETs has the same Corbino-type geometry (circular) as the one mentioned above. The circular architecture was preferred to the squared one owing to the absence of angles. In the aim to reduce the contact resistance, a selectively grown heavily boron doped layer was added beneath the source and drain contacts as described in the previous chapter. MESFETs with gate length L_G of 10, 15, 20, and 30 μm, gate to drain L_{GD} of 20, 30, 40 and 50 μm, and a fixed source to gate L_{SG} of 3 μm were successfully obtained. Figure 4.27 is a picture of all the fabricated MESFET and RB-MESFET. L_G varied in lines, widening from 1 to 4 in X position for a fixed Y position, and L_{GD} ranges in a column, extending from 1 to 4 in Y position for a fixed X position.

4.2.2 High-breakdown voltage MESFET

4.2.2.1 ON-state characteristics

Typical drain current-voltage density J_{DS}-V_{DS} is shown in figure 4.28 (a) for experimental data and (b) simulated one for MESFET#1a. The current is modulated by the gate biased in the reverse condition. We observe the linear, non-linear (knee) and saturation regime. In some cases, the saturation part is not a ”plateau”, this modification in the shape is

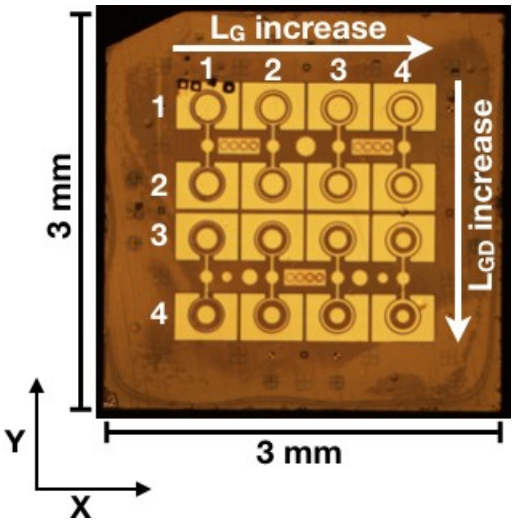

Figure 4.27: Microscopic top view image showing the design of the MESFETs fabricated. They were identified following a matrix Y and X axis; Y corresponds to lines and X to columns with the convention corner cut at the top left.

attributed to short channel effect or to the potential difference drain-gate that becomes higher than gate-source and hence shifting the depletion layer pinch-off. A maximum current density of -0.067 mA/mm and -1.09 mA/mm were obtained at V_{GS} = 0 V and V_{DS} = -40 V for experimental and simulation part at room temperature, respectively. The highest current density was observed for the shortest L_G (10 μm) and L_{GD} (20 μm). A discrepancy between the experimental and simulated level of the drain current density was noticed. Indeed, current density obtained by simulation was about 18 times higher than the one measured experimentally. Several points that they were not taken into consideration in simulation tool such as the contact resistance of source and drain electrodes (it will be treated in the next subsection) that could be not negligible compared to sheet resistance, the space charge region (SCR) induced by the p-type/n-type diamond substrate that could reduce the channel thickness. Anyway, for both simulation and experiment, the maximum current density is dependent on the gate length and gate to drain distance. Indeed, by reducing the distance between the gate and the drain or the gate length, the resistance of the channel is also reduced. 30 V for the gate reverse bias is required to fully deplete the drift layer and close the channel for the simulated part as compare to eh experimental one where only 8 V are needed. This difference is due to some points that were not taken into consideration here, that is to say, the SCR extension in the p-type region (about 0.7 μm) that reduces the channel thickness, a doping concentration with compensation and the contact resistances.

From the linear part (Ohmic regime), when the drain bias is small, the linear on-resistance R_{ON}l can be extracted. For a uniform doping concentration and thickness of the active layer, the linear ON-resistance is strongly dependent on gate length and gate to drain distance. The lowest extracted on-resistance was 4.2 kΩ.cm (corresponding to a specific ON-resistance of 0.63 Ω.cm^2) for L_G = 10 μm and L_{GD} = 20 μm. The MESFET reported by Umezawa et al. with no selective p^+ added on the source and drain contacts exhibited a Schottky behaviour at low drain voltage and an estimated linear ON-resistance R_{ON}l of 150 kΩ.cm (corresponding to a R_{ON}S about 45 Ω.cm^2) at room temperature which is about 36 times higher than the linear ON-resistance determined for the characterized

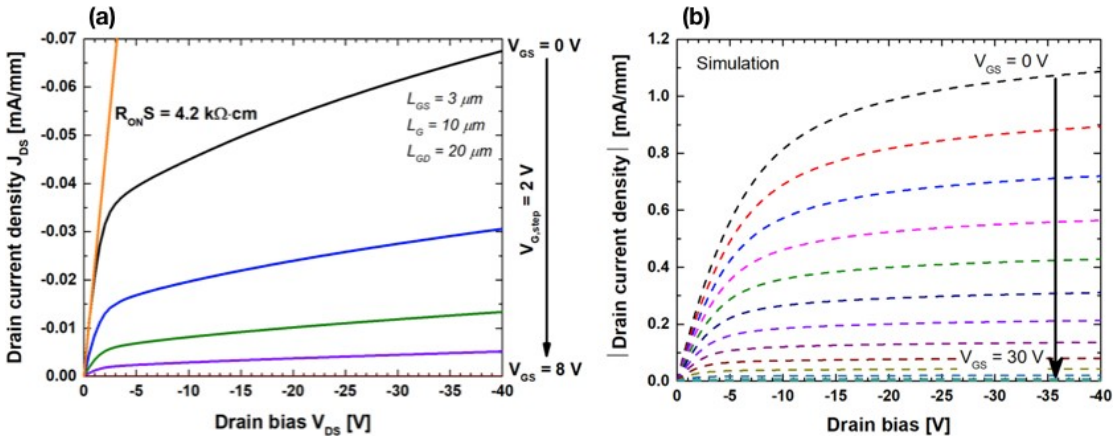

Figure 4.28: On-state static characteristics showing the drain current density as a function of drain bias for different applied gate reverse biases obtained (a) experimentally and (b) by simulation.

MESFET#1a. Umezawa et al. had also reported a linear ON-resistance of about 1.4 kΩ.cm at 300°C which was 107 times higher than the one at RT. The MESFET#1a was not characterized at high temperature, and hence we cannot make a comparison. However, based on the values reported by Umezawa et al. we can predict a linear ON-resistance of about 39 Ω.cm at 300°C. The integration of a selectively grown heavily doped layer contributes in considerably improving the linear ON-resistance. Figure 4.29 shows the evolution of the linear ON-resistance as a function of the gate length L_G for a different gate to drain distances L_{GD}.

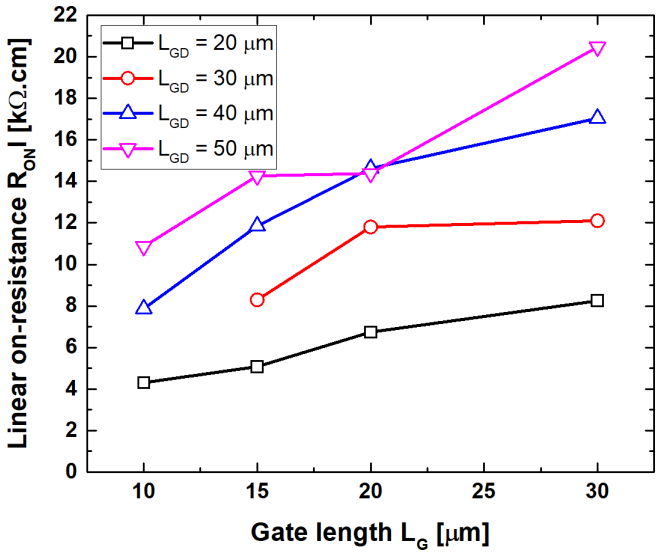

Figure 4.29: Linear on-resistance extracted experimentally for MESFET#1a as a function of gate length for a different gate to drain lengths.

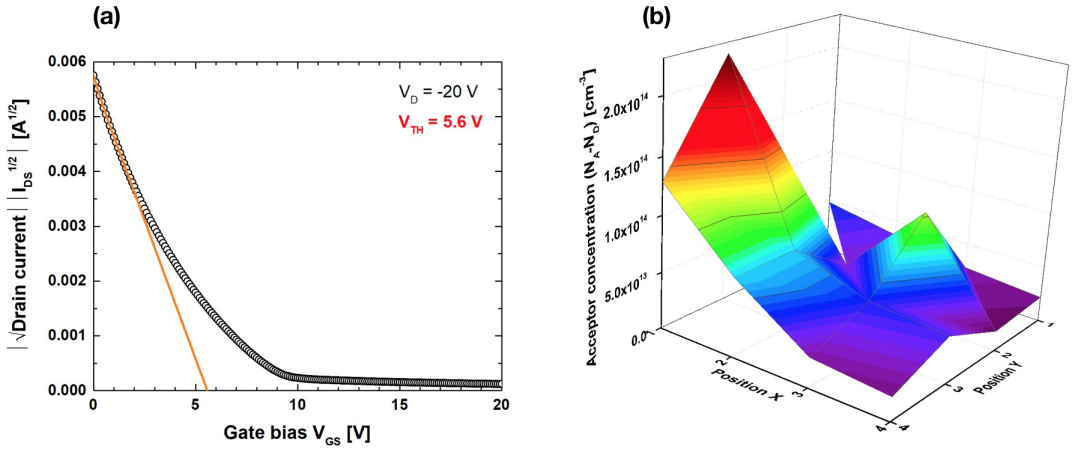

Figure 4.30: (a) Typical threshold voltage for the transistor with the lowest gate length and shortest gate to drain distance. From the extracted threshold of each transistor of MESFET#1a (b) a doping concentration mapping was realized.

4.2.2.2 Threshold voltage and doping mapping

Based on the threshold formula described in chapter 2, acceptor concentrations (N_A - N_D) were extracted for different transistor position on sample MESFET#1a surface. The square root of the drain current as a function of the gate bias data is presented in a typically obtained figure 4.30-a. The linear trends at small gate bias are extrapolated, and the threshold voltage V_{TH} extracted from the intersection at the x-axis. The threshold voltage extracted through this method gives information on acceptor concentration near the surface. The small curvature that appears before closing the channel (between 6 and 10 V) could be due to the influence of the space charge region induced by the *pn* junction. An acceptor concentration mapping of the sample was then obtained, as seen in figure 4.30-b. Near the surface, the acceptor concentration extracted seems to be not uniform.

The boron doping concentration measured by SIMS was 8×10^{15} cm^{-3}, and the acceptors' concentration obtained by threshold voltage V_{TH} varies between 1.7×10^{13} and 2.2×10^{14} cm^{-3} with considering the back depletion of the channel due to the donors' semi-insulating substrate. So far, it is impossible to determine the compensation percentage based only on the difference between $[B]_{SIMS}$ and $[B]_{TH}$, further analysis such as low-temperature C-V measurements are required.

4.2.2.3 High current density MESFET

For almost the same doping concentration (7×10^{15} cm^{-3}) and a doubled thickness of the active layer (3.2 μm), the MESFET#2a exhibited current densities much higher than MESFET#1a at room temperature. Figure 4.31-a shows a comparison of I_{DS}-V_{DS} be- tween MESFET#1a and MESFET#2a exhibiting a high current density measured. The transistors have the same L_{GS}, L_G, and L_{GD}. The maximum current density attained -2.3 mA/mm at a drain bias V_{DS} of -20 V for a gate bias V_{GS} of 0 V. The linear on-resistance R_{ON}l extracted from the linear part of the curve that gave the maximum current density was only 422 $\Omega.cm$. However, due to an increase of the gate leakage current (compliance on gate current of 10 μA) the channel remained open and hence, the transistor could not

be switched OFF as seen in figure 4.31-b. This is because of the thickness of the channel that is to thick to deplete the region under the Schottky gate. In fact, the current density obtained for MESFET#2a corresponds to a simulated transistor with no compensation. As for MESFET#1a, the low current density could be the results of high compensation level as well as a non-negligible p^+/p^- contact resistance.
A positive bias on the back substrate was applied to close the channel but no concluding results was noticed. During the homoepitaxial growth of the drift layer, if the plasma covers the whole substrate, the p^- layer also grows on the substrate sides with a growth speed much lower than that of the surface substrate. This side growth hinds the back substrate polarization and hence to spread the space charge region from the *pn* junction in the p layer.

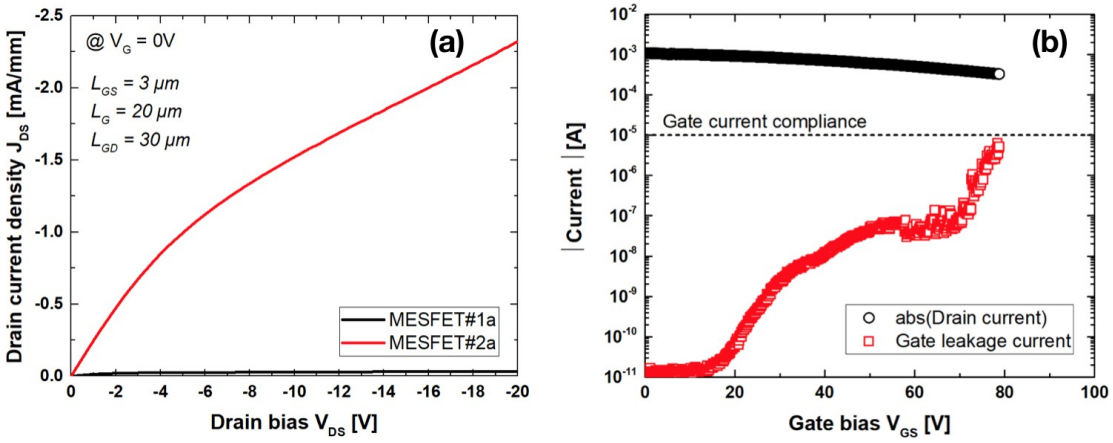

Figure 4.31: (a) Comparison of drain current density as a function of drain bias for MESFET#1a and MESFET#2a for V_G = 0 V. (b) Drain and gate current as a function of gate bias for MESFET#2a. Gate leakage increases and avoids the transistor to turn-off.

4.2.2.4 Reverse state characteristics

The certain and powerful feature of ultra wide bandgap semiconductors is their abilities to withstand high electric fields in the blocking state. In this part, we will discuss the high breakdown voltages (BVs) achieved. Since the active layer of MESFET#2a was too thick to close the channel without inducing an important gate leakage current, only MESFET#1a was characterized in blocking state. The highest obtained BV ever reported at this time for FETs is shown in figure 4.32-a. In this figure, both experimental and simulated data are enclosed. Experimentally, MESFET with the largest gate length (L_G = 30 μm) and the longest drain to gate distance (L_{GD} = 50 μm) exhibited the best BV of -2288 V. A high reverse bias of 30 V (about 5 times higher than the threshold voltage) was applied on the gate in order to reduce leakage current through the gate contact. Simulated OFF-state for the same L_G and L_{GD} values revealed a BV of -2483 V at V_G = 40 V. Watanabe's ionization coefficients were implemented for the breakdown. Even if the parameters such as the depletion region induced by substrate p-n junction and the amount of compensation that were not considered, the simulated BV was close to the experimentally obtained one. It is because when the channel is closed, the transistor behaves as a punch-through diode. A more detailed discussion will be given in the "channel field distribution" part. As for the high leakage current obtained for the simulated curve, it

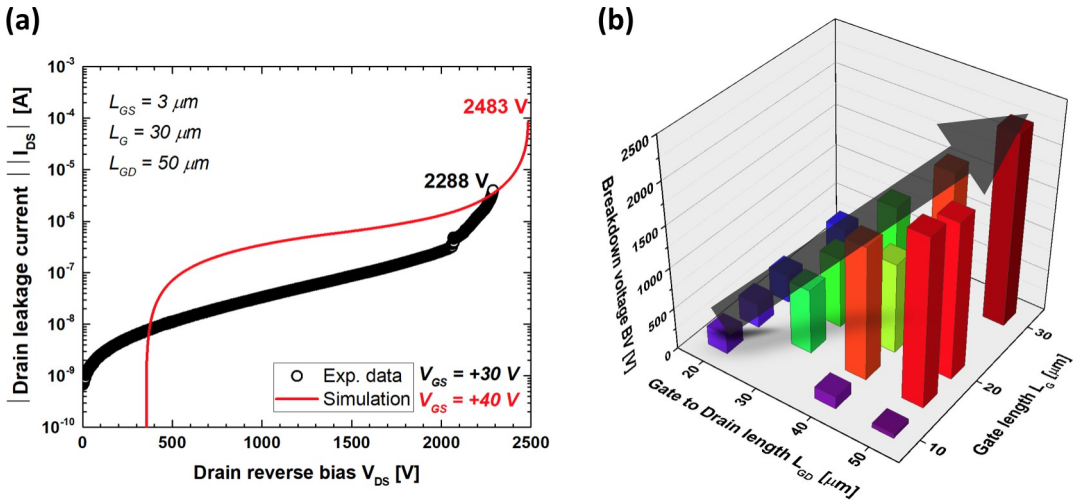

Figure 4.32: (a) Drain leakage current as a function of drain reverse bias. The highest BV of 2288 V was obtained for the largest gate and longest drain to gate distance. (b) Summary of BV for transistors with different gate length L_G and gate to drain length L_{GD}. The BV has a linear trend with L_{GD}.

could be attributed to an insufficient gate reverse bias to close the channel and avoid drain leakage current through it. Figure 4.32-b summarizes the obtained BVs for the different MESFETs fabricated and characterized. The BV tends to increase linearly with increasing the gate length and the gate to drain length which was in agreement with the reported one. The estimated electric field is 0.6 MV/cm. It is an underestimated breakdown field since a 1D is considered, the border effects are neglected. From the simulation, the electric field distribution at BV was also extracted. In figure 4.33, the 2D electric field distribution, as well as the surface electric field and electrostatic potential distribution, are shown. As expected, the peak electric field was localized at the gate edge towards the drain side and reaches a maximum value of 2.9 MV.cm^{-1}. The second peak was at the drain edge towards the gate. Between these two main electric field peaks, we can observe a steep decrease of the surface potential.

4.2.3 RB-MESFET

In this study, a reverse blocking metal semiconductor field effect transistor (RB-MESFET) was also achieved by realizing a minor change to the standard MESFET structure. The RB-MESFET distinguishes from the usual MESFET by its drain which is a Schottky contact instead of Ohmic. The gate and the drain have the same Schottky metal (Mo metal deposition done at once). This small difference makes it able to withstand reverse voltages. Details on the RB-MESFETs fabricated could be found in the previous chapter. The RB transistor provides a bi-directional switch and is of high interest for power converter topologies such as matrix converters, two-stage direct power converters (DPC) and three-level voltage source rectifiers [154]. Originally, bi-directional switches are formed by two silicon insulated-gate bipolar transistors (IGBTs) and two diodes (that play the role of the reverse blocking characteristics) anti-serially connected. However, due to the high on-state power loss obtained which is determined by the sum of the on-state of the IGBT

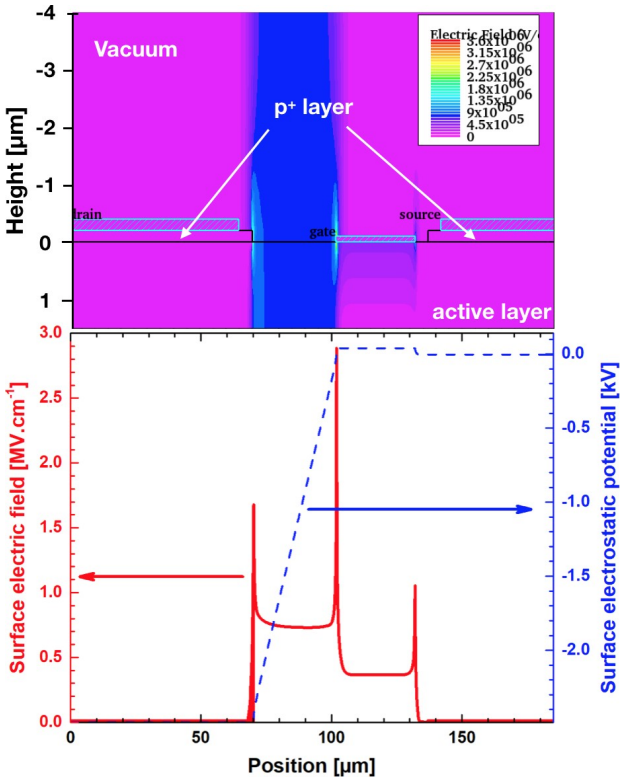

Figure 4.33: Simulated electric field distribution within the transistor at BV. Corresponding surface electric field and potential distributions are also plotted.

and the diode since the current flows through both of them, an RB-IGBT was developed to reach a low on-state power loss [155]. Therefore, to form a bi-directional switch, only two RB-IGBTs are needed and are connected in an anti-parallel way. In the following section, we will discuss the first diamond RB-MESFET fabricated and characterized. The difference between the two bi-directional switches explained are represented in figure 4.34 where the conventional IGBT was replaced by the MESFET or RB-MESFET. Some of the following results were investigated by Leo CAMBOU, a first-year Master internship student. RB-MESFET#1b and RB-MESFET#2b will be discussed.

4.2.3.1 ON-state temperature dependence electrical characterization

Figure 4.34 shows a cross-sectional view of the RB-MESFET investigated. The transistor characteristic of RB-MESFET#1b and #2b are presented in figure 4.35. Measurements were done at room temperature. Due to the Schottky contact of the drain instead of Ohmic, a built-in potential is observed for both fabricated and characterized RB-MESFET#1b and #2b. RB-MESFET#1b has L_G = 20 μm, L_{GD} = 20 μm and L_{GS} = 3 μm and RB-MESFET#2b has L_G = 10 μm, L_{GD} = 30 μm and L_{GS} = 3 μm. The maximum drain current density obtained for RB-MESFET#1b (figure 4.35-a) at a drain bias of -40 V is -1.8 μA/mm for a 0 V applied gate bias. The corresponding linear-on resistance R_{ON}l is of 207 kΩ.cm which is extremely high. The high resistance can be originated from the p- layer or the p+/p- interface. The RB-MESFET#2b with an almost same doping concentration as RB-MESFET#1b and a thickness multiplied by about 2,

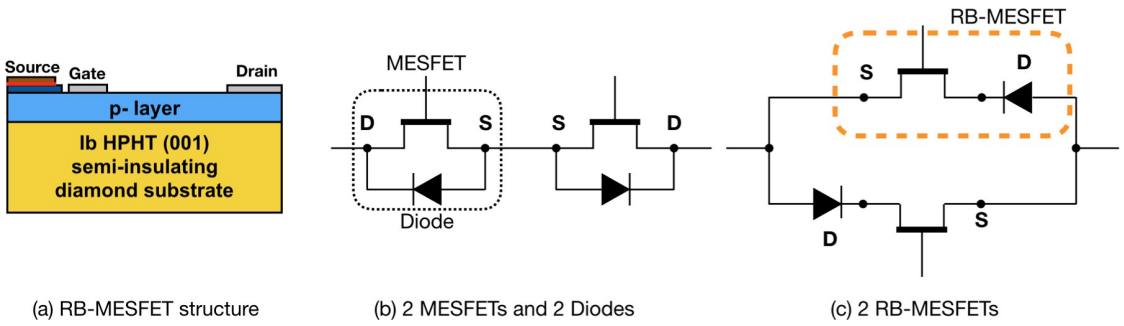

Figure 4.34: a) Cross-sectional view of Reverse Blocking (RB) MESFET as well as two configurations of bi-directional switches using b) two MESFETs and two diodes anti-serially connected and c) only two RB-MESFETs with an anti-parallel connection.

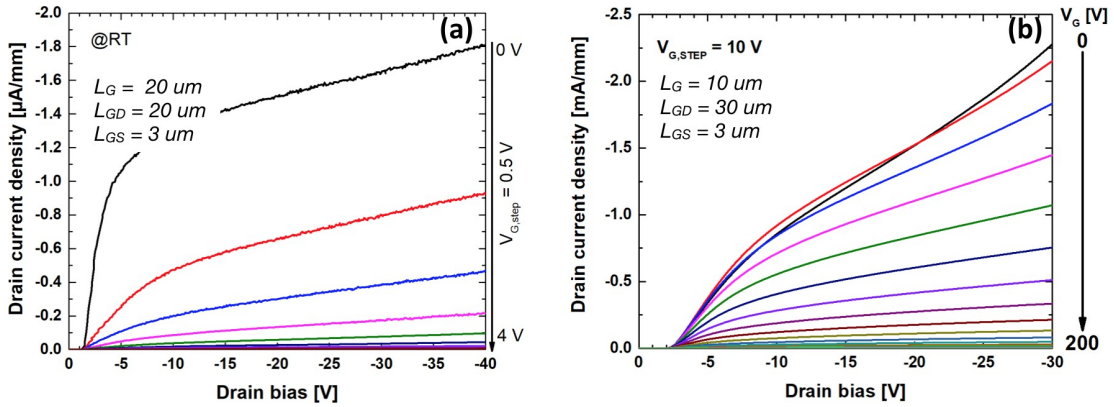

Figure 4.35: Current modulation of the reverse blocking MESFET (a) #1b and (b) #2b

exhibited a maximum drain current density at a drain bias of -30 V of -2.3 mA/mm for a 0 V applied gate bias (figure 4.35-b). The maximum current density is the highest bulk conduction value never reported so far. The lowest linear-on resistance extracted for the later is 708 Ω.cm (corresponds to 0.23 mΩ.cm^2 considering the active layer thickness). However, compared to RB-MESFET#1b where the threshold voltage is 5.1 V, the threshold voltage extracted for RB-MESFET#2b is 148 V. At this high gate biases, there is a risk that the gate electrode starts to induce leakage current, but fortunately that was not the case here. Temperature dependence for the current modulation was investigated only for RB-MESFET#1b. Figure 4.36 shows the drain current density temperature influence from room temperature to 260°C. Because of the incomplete ionization of boron impurities at room temperature, the transistor exhibited improved electrical characteristics when increasing the temperature up to 260°C. The maximum current density was multiplied by 25 and reached -0.046 mA/mm at -40 V and the linear-on resistance was divided by 9 (23 kΩ.cm).

4.2.3.2 OFF-state

One of the strengths of the reverse blocking MESFET is the possibility to apply a reverse bias (positive) on the drain side owing to the Schottky junction. As presented in figure

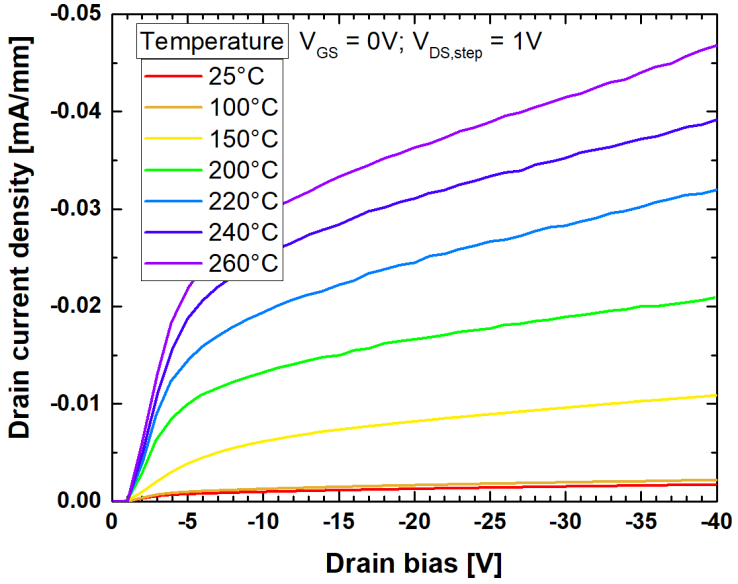

Figure 4.36: Temperature influence of the drain current density as a function of drain bias for a fixed gate bias of 0 V. The maximum current density was multiplied by 25 and the linear-on resistance divided by 9.

4.37, the breakdown voltages obtained for both RB-MESFET#1b and #2b are the highest obtained values for bulk conduction transistor and are comparable to an optimized reported SiC RB-MOSFET [156].
A reverse gate bias of 20 V and 200 V was applied to avoid any leakage current through the gate and to close the channel for RB-MESFET#1b and RB-MESFET#2b, respectively. RB-MESFET#1b has shown a drain forward BV of -1812 V and a reverse drain BV more than 3 kV (with a leakage current of 60 nA). The forward BV and reverse BV of RB-MESFET#2b were lower than that of RB-MESFET#1b with -1116 V and 2379 V, respectively. Even though, these obtained BV values have never been achieved so far for diamond bulk conduction transistor. The breakdown of the devices is due to an important increase of leakage current through the gate. Even if the breakdown voltage is the highest values ever reported so far for diamond transistors, they remain lower than the diamond potential. The estimated breakdown field is 0.6 MV/cm for the device that has shown 3 kV. One reason for this premature breakdown voltage will be discussed in the following subsection.

4.2.4 Channel field distribution

When modulating the current conduction within the channel by the Schottky junction, a depletion region is formed. This depletion region can be divided into 3 regions explained below.

Three-region model

This part assumes a uniform doping profile for the potential distribution inside the channel. When a reverse bias is applied on the gate, and a drain to source bias is applied, a depletion region underneath the Schottky gate appears as discussed previously. This zone can be

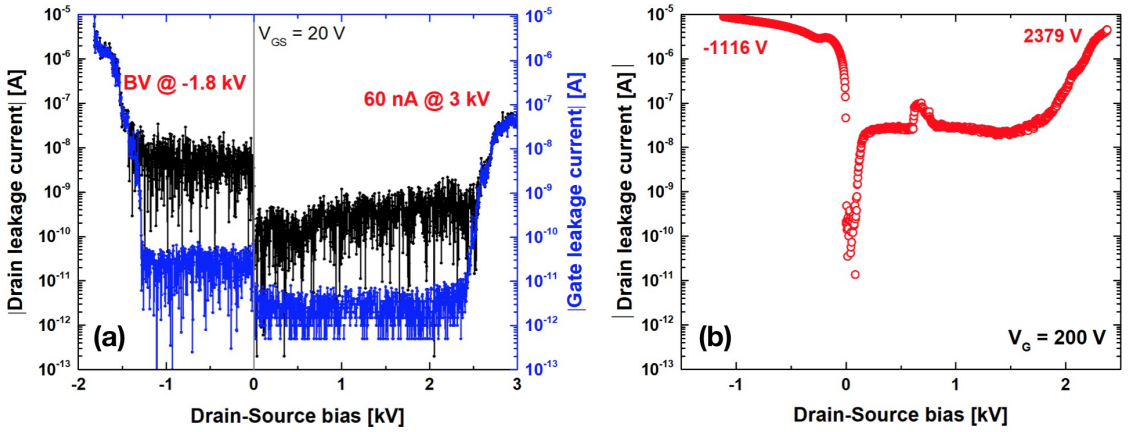

Figure 4.37: Blocking characteristics in forward and reverse voltage for (a) RB-MESFET#1b and (b) RB-MESFET#2b. RB-MESFET#1b has the highest reverse blocking voltage of 3 kV.

divided into 3 regions [157]:

**Region I* : Constant mobility region. Carriers move below the velocity saturation. This region extends from gate edge on the source side to Xa. Xa is the point where the velocity saturation occurs. Here we neglect the extension of the lateral depletion towards the source; it has no influence.

**Region II* : Saturation velocity region. This region extends from Xa to the gate edge near the drain. Drain potential dependence

**Region III* : Lateral extension of the depletion layer towards the drain side. A region where the maximum electric field is defined and hence responsible for the breakdown near or at the gate edge. This region is drain potential-dependent.

Solving Poisson equation and applying boundary condition between region I and II, then solving Laplace equation and applying boundary condition between region II and III, the depletion region height at any x position underneath the Schottky gate can be expressed as follow :

$$h(x) = \sqrt{\frac{2\varepsilon_s(V_{bi} + V_{GS} - V(x))}{qN_A}} \tag{4.2}$$

where V(x) is the bias at position x under the Schottky gate and is dependent on the drain bias. More details on the analytical model could be found in these references [157]. For $x=L_G$, the potential V(x) can be approximated to be equal to V_{DS}. Therefore, equation (4.2) becomes

$$h = \sqrt{\frac{2\varepsilon_s(V_{bi} + V_{GS} - V_{DS})}{qN_A}} \tag{4.3}$$

In most of the cases, the depletion region is assumed to occur following a quarter circle, and hence lateral depletion and depletion height have the same expression. A more accurate expression for the lateral depletion expansion could be written as [158]:

$$D_{lat} = \sqrt{\frac{2\varepsilon_s}{qN_A(V_{bi}+V_{GS})}(V_{bi} + V_{GS} - V_{DS})} \tag{4.4}$$

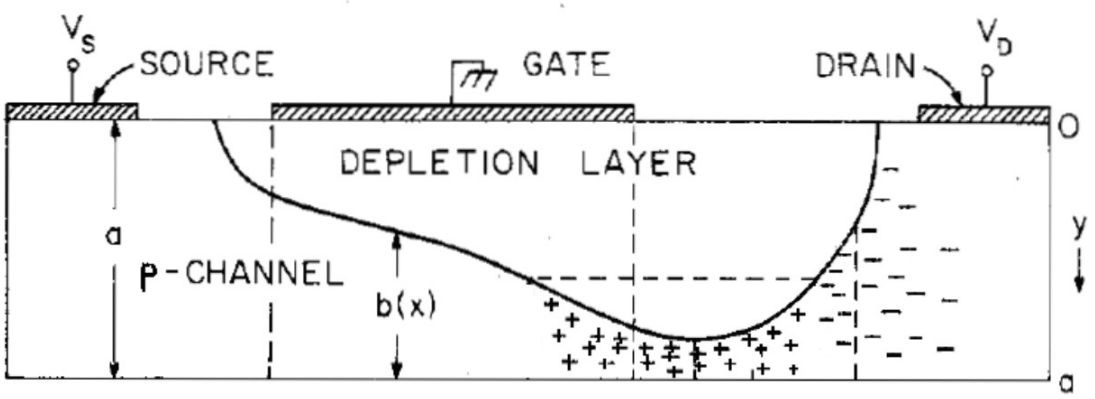

Figure 4.38: Schematic view of a MESFET p-type channel under blocking state characterization. Due to a potential difference formed a dipole is created under the gate.

Determination of lateral gate depletion expansion towards drain contact - MESFET

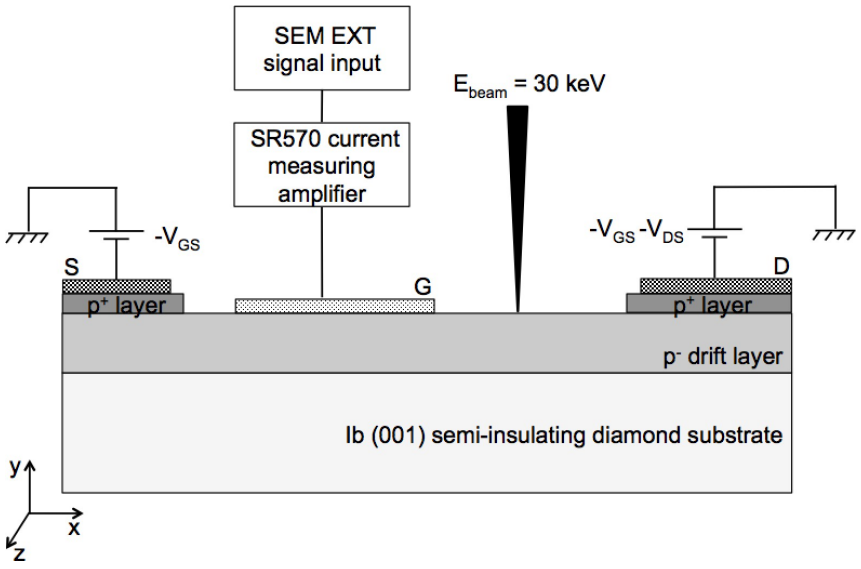

Figure 4.39: Cross-sectional view and experimental setup of the characterized transistor [159].

In this section, experiments were done using a different sample than the ones discussed previously. The design is the same but with different boron doping concentration and thickness. The cross-sectional view of the fabricated and investigated diamond MESFET, as well as the measuring circuit, is shown in figure 4.39. The p- diamond layer was

epitaxially grown by chemical vapor deposition (CVD) on an Ib (001) high-pressure high-temperature semi-insulating diamond substrate. Details about the growth condition of the p- layer have been reported in our previous work [11]. Prior to the source and drain metal deposition, a p+ heavily doped layer was selectively grown using hot-filament CVD to reduce series contact resistance. A Ti/Au metal mask was used to restrict the p+ layer growth to the source and drain regions. Information on the p+ layer growth and the metal mask used were reported in our last study [160]. The growth time was set to 1 hour in this case. The thicknesses of the drift and the heavily doped layers determined by SIMS were 2.7 μm and 0.4 μm, respectively. The boron doping concentrations were $4.7 \times 10^{15}\ cm^{-3}$ for the drift layer and more than $2 \times 10^{20}\ cm^{-3}$ for the heavily doped one. The doping concentration of the former was extracted using the usual threshold voltage formula. The sample surface was exposed by UV/O_3 treatment to terminate the surface by oxygen atoms bonding to reduce surface leakage current, and hence to avoid surface drain leakage current through the gate. Ti/Au was used for Ohmic contact and Ru for Schottky contact. The gate length L_G was 20 μm and the gate to drain length L_{GD} was 30 μm.

Determination of the laterally expended region was explored using electron beam induced current technique. The technique works in the same manner as described in chapter 3. Nevertheless, a three-probe system is needed here as compared to a Schottky diode to control the transistor. For that, two SMUs were used: One controlling the Schottky gate bias and another the drain-source bias, as shown in figure 4.39.

The electron beam energy E_{beam} was set at 10 and 30 keV and the beam radius at 6 nm. The measured beam current by Faraday cage was 3.85 nA for 30 keV and 2.41 nA for 10 keV. At this low beam current and with the extremely high diamond thermal conductivity (2200 $W \cdot m^{-1} \cdot K^{-1}$; 18 times higher than that of graphite), the temperature rise due to the electron beam is negligible [161]. Using Monte Carlo simulation, the penetration depth was determined. About 75% of the beam energy was located inside the p- layer when using a beam accelerating voltage of 30 keV. For a simplified study, the gate was fully depleted. Due to the system limitation, the full depletion under the gate was achieved by applying a negative bias on the source, resulting in a potential difference between the gate and the source. This negative bias was taken into consideration when applying the bias on the drain side. The total bias applied to the drain contact varies between -30 V and -170 V. The backside of the sample has a floating potential.

Figure 4.40 shows the EBIC image (right) and the corresponding SEM image (left) with the located drain, source and gate of the analyzed transistor. The EBIC image was captured when a drain-source bias difference of 150 V and a fixed gate bias of 50 V were applied. A bright region appeared at the edge of the gate towards the drain side. This bright region provides information on lateral depletion expansion and the minority carrier diffusion length.

A direct collection of EBIC has led to figure 4.41, where the EBIC intensity as a function of the distance from the gate edge is obtained for different drain-source biases for a closed channel (gate bias of 30 V). The peak intensity at the edge of the Schottky gate electrode at a drain bias of 0 V shifts away from the edge when a bias is further applied on the drain electrode up to 200 V. The beam accelerated voltage was 10 kV. The observed shift is due to the attraction of the formed dipole under the gate Schottky, as seen in figure 4.38 [162]. The maximum EBIC intensity changes and a *plateau* appears with increasing the drain bias because the pear shape of the created electron-hole pairs becomes more

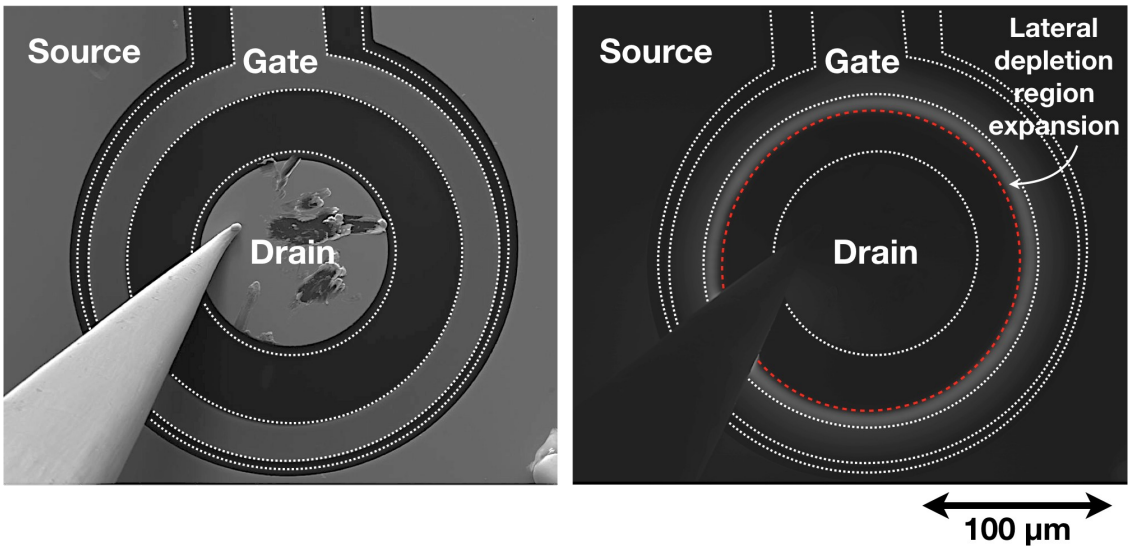

Figure 4.40: SEM and corresponding EBIC image of a closed channel MESFET. The applied gate bias is 50 V, and the drain bias is 200 V. A lateral depletion is formed starting from the gate and expanding towards the drain.

and more inside the lateral depletion region. By fitting the last part of the curves, far away from the gate edge, an effective diffusion length was obtained for each drain biases. The obtained value was independent of the drain bias and found to be 1.3 μm. Figure 4.42 summarizes the extracted values of the lateral depletion width as a function of the applied drain bias. The obtained experimental results were well fitted by the theoretical expression 4.4. Based on the experimental data, the lateral depletion reaches the drain contact for a bias of 1.5 kV suggesting an eventual reason for the premature breakdown (lateral punch-through analogy). 1.5 kV was obtained for a MESFET with L_{GD} = 30 μm. An extrapolation of the experimental data in figure 4.42 showed that at 1.5 kV applied drain bias, the lateral depletion layer expands up to 37 μm which is slightly more than the distance between gate to drain edge.

Determination of lateral drain depletion expansion towards gate contact - RB-MESFET

Same experience as reported previously was performed on an RB-MESFET in a reverse voltage. Figure 4.43-(a) is an EBIC image of the RB-MESFET with a gate reverse bias of 30 V and a drain reverse bias of 140 V. In this configuration, the lateral depletion region expands from the drain edge towards the gate side (direction represented by yellow arrows). It is because the drain electrode has a Schottky contact with 1.8 eV SBH that create a potential barrier. Then, due to a potential difference increase between the gate and the source, and the gate and the drain, the depletion regions extend. Figure 4.43-(b) presents the EBIC line scan in the green rectangular region in EBIC image. The applied reverse drain bias ranges from 20 V to 200 V for a fixed reverse gate bias of 30 V. Increasing the drain reverse bias contributes in a formation of a ”plateau” in the shape of the EBIC curve intensity. The ”plateau” means that the pear shape is almost entirely inside the depletion region.

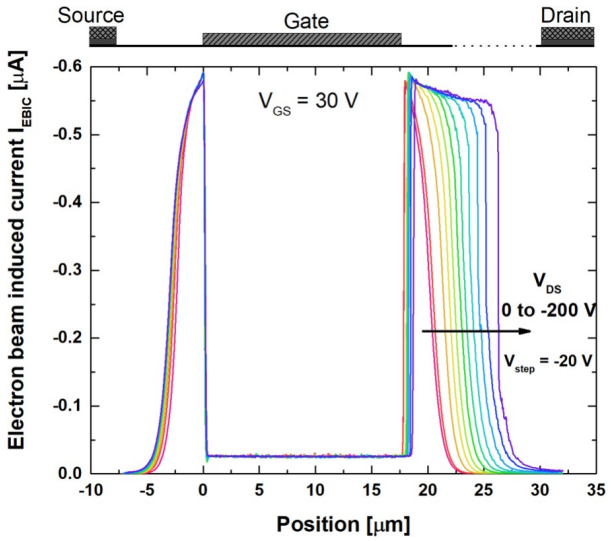

Figure 4.41: EBIC collected for different applied drain bias with a fixed gate bias of 30 V as a function of distance from the gate edge. The signal extends from the gate edge towards the drain side when the drain bias increases, this is the lateral depletion region.

4.3 Conclusion

In this chapter, an evaluation of the fabricated edge termination Schottky diodes, as well as field effect transistors, was presented. Both electrical characterizations and EBIC analysis to map the surface electric field were performed for all the devices. The edge termination architecture is of great importance for all devices to take full advantage of intrinsic material properties. An unterminated device will exhibit a premature breakdown voltage because of the device border effect that implies an electric field crowding. This electric field crowding at the edge induces leakage current and avoid the breakdown to occurs at the material. A well-designed device will show an avalanche breakdown that is induced by impact ionization. If the crowding effect remains at the edge, the impact ionization will be influenced by the border and hence will be larger. In that, it is crucial to develop an edge termination structure for diamond. As technologies such as ion implantation and well-controlled dry etching are not mastered for diamond material, simples edge termination were investigated. Floating field rings, as well as a field plate, were chosen. The FFR-SBDs and FP-SBDs have exhibited effectiveness in the electric field distribution, however, due to lack of process fabrication the edge termination SBDs reached only 0.8 MV/cm and 0.55 MV/cm breakdown fields for FFR-SBDs and FP-SBDs, respectively. Optimization of the process is under investigation for future work.
On of the device that completes the Schottky diode is the field effect transistor. In fact, in any commutation cells, rectifiers and switches are essential. MESFET and a new version RB-MESFET were realized and have demonstrated excellent characteristics. The bulk conduction MESFET exhibited a low on-resistance by the introduction of a heavily doped layer selectively grown under the source and the drain. And the highest breakdown voltage reached nearly 2.3 kV by increasing the gate to drain distance. However, as the gate to drain cannot be increased indefinitely without damaging the on-resistance, a minor change in MESFET structure leads to an increase of the breakdown voltage up to 3 kV. The RB-MESFET that uses a drain Schottky contact was fabricated for the first time and

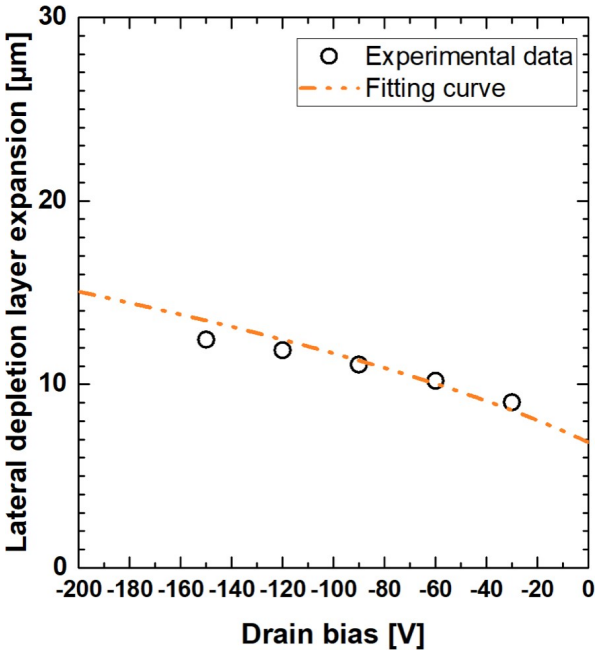

Figure 4.42: Lateral depletion expansion as a function of applied drain bias for a transistor that exhibited 1.5 kV for the BV. Experimental data were well fitted by the equation.

exhibited the lowest on-resistance and the highest breakdown voltage. EBIC has allowed an understanding of the premature breakdown of the transistors.
Based on this evaluation work, the Schottky diode that exhibits the lowest leakage current and the highest breakdown field is selected for an accurate extraction of the ionization coefficients. The next chapter will discuss the ionization coefficients extraction for diamond epilayers.

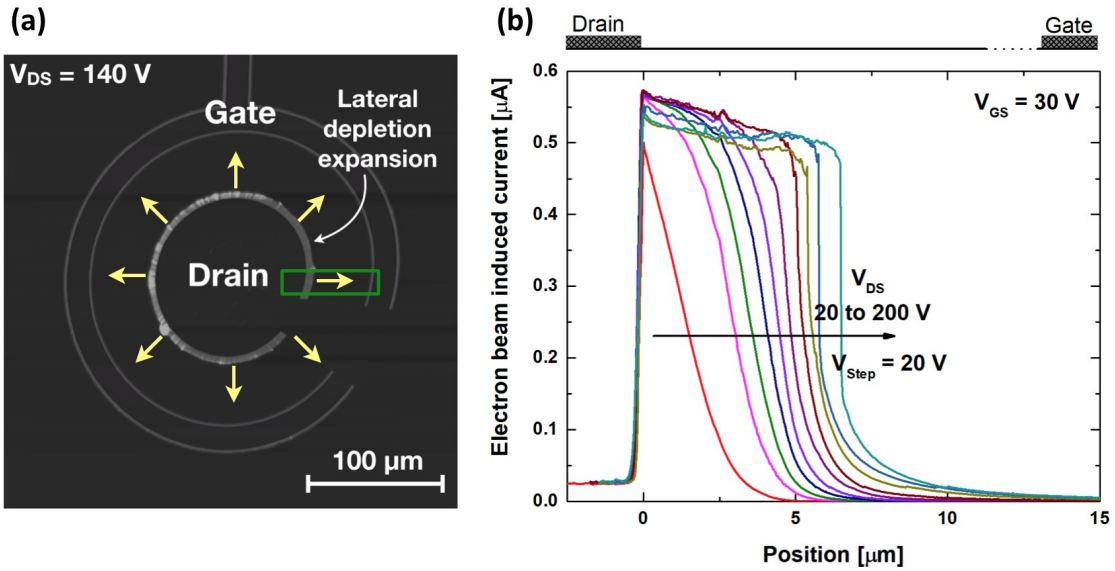

Figure 4.43: Drain lateral depletion expansion as a function of applied drain reverse bias for a fixed gate bias of 30 V.

Chapter 5

Impact ionization coefficients

To bring diamond to its highest level of technology, the route is still long. One has to master the process fabrication technology, the quality of diamond epilayers, and the optimization of device structures. G. Chicot et al. [163] have reported that an optimized drift layer regarding doping level and thickness can achieve its lowest specific ON state resistance compared to a non-optimized one for a given breakdown voltage. However, the process of determining the reverse operation limits of diamond devices is still both experimentally and theoretically imprecise but is at present under study. One of the crucial points in power devices is the high blocking voltage that a device can withstand. In this reverse operation, breakdown by avalanche phenomena is the main process that can be predicted if an accurate impact ionization coefficients are known. Several works for determining these impact ionization coefficients have been performed by extracting them under high electric fields. However, if the breakdown voltage occurring in the devices is not only due to an avalanche process, can the fitted models lead to an extrapolation of the local analysis of avalanche phenomena? Complementary works are necessary for the study of the breakdown phenomenon within diamond. It is feasible by theoretical approaches as well as experimental fits. Therefore, the best characteristics of diamond power electronic devices can emerge if both experimental and simulated approaches converge.

In this last chapter, first a complementary work by analyzing the ionization coefficients reported is discussed. The effects of these coefficients on the breakdown voltage and electric field distribution while simulating the avalanche phenomena are examined. The reverse blocking characteristics of both fabricated and simulated diamond SBDs are investigated and compared using two-dimensional (2D) simulation and reported experimental data. Then, an attempt to extract the avalanche parameters will be explained.

5.1 Impact ionization coefficients

5.1.1 Literature review of ionization coefficients

The techniques to obtain the avalanche parameters are well established since before diamond, it was realized for other semiconducting materials such as Si, GaAs, GaN or SiC. Several techniques exist to extract the impact ionization coefficients whether it is theoretically or experimentally. Here are some examples:

- *Ab initio* calculations using a full band Monte Carlo (FBMC) simulation method.
- Modeling of a device through 2D simulation with implementing numerical models such as activation of dopants, concentration and temperature dependent mobility and avalanche coefficients.
- Theoretically by fitting experimentally reported breakdown voltages.
- Analyzing the gate current behavior of a transistor.
- Initiating the avalanche optically such as photomultiplication technique or optical beam induced current (OBIC) technique.
- Initiating the avalanche electrically using electron beam induced current (EBIC) technique.

	A_p [cm^{-1}]	B_p [$V.cm^{-1}$]	A_n [cm^{-1}]	B_n [$V.cm^{-1}$]	c
R.J. Trew [166]	1.935×10^8	7.749×10^6	1.935×10^8	7.749×10^6	1
T. Watanabe [107]	1.93×10^5	4.41×10^6	4.62×10^5	7.59×10^6	1
J. Isberg[167]	4.0×10^6	11×10^6	N/A	N/A	1
	6.0×10^5	8×10^6	N/A	N/A	1
S.J. Rashid [168]	5.48×10^6	14.2×10^6	1.89×10^5	17.0×10^6	1
A. Hiraiwa [164]	6.1×10^4	13.94×10^6	1.46×10^5	24×10^6	1
Y. Kamakura [165]	4.2×10^6	21×10^6	3.7×10^6	58×10^6	1
N. Skukan [140]	0.56×10^4	216×10^4	0.56×10^4	216×10^4	1
	180×10^4	19.7×10^4	180×10^4	19.7×10^4	0.2

Table 5.1: Avalanche multiplication parameters extracted from the literature.

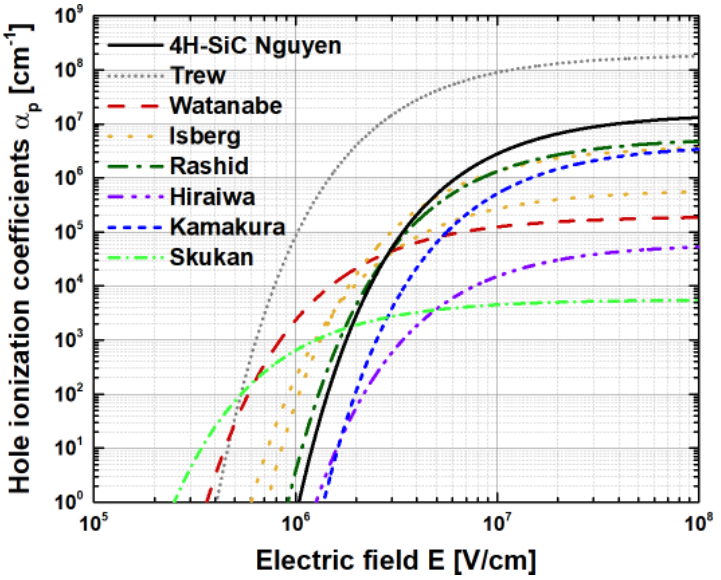

Figure 5.1: Hole impact ionization rates as a function of electric field at 300K for reported 4H-SiC and diamond.

Recently, Hiraiwa *et al.* and Kamakura *et al.* have studied the avalanche breakdown process by extracting impact ionization coefficients (IICs) in Chynoweth's form from an arbitrary relationship between breakdown voltage and doping density [108, 164], and from the high-field carrier transport using a full-band Monte Carlo (FBMC) method based on *ab initio* calculations[165], respectively. All the avalanche coefficients reported for diamond are summarized in table 5.1.

Figure 5.1 shows the impact ionization rates plotted as a function of the electric field following the Chynoweth expression given in equation 5.1 [106] and using the values summarized in Table II. The impact ionization rates for 4H-SiC reported by Nguyen *et al.* [169] were also added. From this figure, it is seen that the generation of carriers by impact ionization occurs at much larger electric fields for diamond using Skukan, Kamakura and Hiraiwa model, which is what it is expected for diamond as compared to 4H-SiC. Rashid model is close to Nguyen model, and Trew model overestimated the impact ionization rate.

$$a_{n,p} = A_{n,p}\, exp^{\left(-\frac{B_{n,p}}{E^c}\right)} \tag{5.1}$$

5.1.2 Analysis of three different ionization coefficients

5.1.2.1 Device description

The two diamond SBDs used in this part were previously reported by Dr. H. Umezawa [170, 171]. The SBDs were fabricated on a p-/p+ homoepitaxially grown diamond layers on Ib(001) high-pressure high-temperature (HPHT) diamond substrates. The SBDs have a pseudo-vertical structure. The concentrations of boron-doped layers [B] and the thicknesses for diode 1 were $\geq 2 \times 10^{20}$ cm^{-3} and 1.1 μm for the heavily doped layer p$^+$, and 2.8×10^{15} cm^{-3} and 0.96 μm for the drift layer p-, respectively. Diode 2 had a boron doping concentration $\geq 2 \times 10^{20}$ cm^{-3} and a thickness of 5 μm for the heavily doped layer p+. The drift layer p- had an increasing gradient doping profile from the surface towards the heavily doped layer ranging from 5.6×10^{16} to 1×10^{17} cm^{-3} and a thickness of 1.2 μm. The parameters were determined by SIMS. Titanium was used for Ohmic contact for both diodes 1 and 2. Platinum (Pt) and molybdenum (Mo) were utilized for diodes 1 and 2, respectively. No junction termination or field engineering at the surface was used on these pseudo-vertical SBDs (pvSBDs); thus, the electric field was not relaxed. Only oxygen was used to terminate the diamond surface to reduce the surface leakage and optimize the Schottky metal/diamond interface [**?**]. The devices were characterized using an Agilent 4156C parameter analyzer and a Keithley 237 source measurement unit.

5.1.2.2 Implemented models

The analysis of the ionization coefficients was realized by implementing the coefficients in the simulation tools and making a comparison between the results obtained experimentally and by simulation — nly the parameters reported by T. Watanabe *et al.*, A. Hiraiwa *et al.* and Y. Kamakura *et al.* were selected.

The devices described above were simulated using finite element TCAD Silvaco 2D simulation software. To reduce the calculation time, we simulated half of the devices by considering the symmetry along the y-axis. Although a diode in a vertical SBD structure exhibits a low and uniform on-resistance regardless of its position on the wafer compared with a diode in a pvSBD structure [124], and, as we are interested in the reverse blocking operation, we used a vSBD structure to simplify the calculation. We assumed a perfect diamond material without bulk defects. Indeed, these defects could be one of the factors that lower the electric field breakdown and decrease the breakdown voltage compared with the ideal case [27], and, therefore, one of the reasons why the breakdown voltage depends on the electrode distance [172]. To reproduce as closely as possible the real conditions of the devices, a positive electron affinity of 1.7 eV corresponding to an oxygenated diamond surface [173], a Schottky barrier heights (SBHs) of 2.62 eV (for Pt Schottky contact) and 1.92 eV (for Mo Schottky contact), as well as models specific to diamond - including the incomplete ionization model and the empirical model on the concentration and temperature dependent mobility - have been implemented [90, 66]. The increasing gradient doping profile was also considered for diode 2. A Shockley-Read-Hall (SRH) carrier lifetime of 2×10^{-10}s was set for both holes and electrons. The models mentioned above and others

applied to diamond that we used are clearly described by Marechal *et al.* [174]. In addition to these models, the thermionic emission (TE) model was used following the equation [175],

$$J_{TE} = A^* T^2 exp\left(-\frac{q\varphi_b}{kT}\right)\left[exp\left(\frac{qV}{kT}\right) - 1\right] \tag{5.2}$$

$$\text{with} \quad \varphi_b = \varphi_b^0 - \Delta\varphi_b \quad \text{and} \quad \Delta\varphi_b = \sqrt{\frac{qE}{4\pi E_s}}$$

where J_{TE}, T, q, k, V, and φ_b are the thermionic emission current density, lattice temperature, elementary charge, Boltzmann's constant, applied bias, and SBH, respectively. The effective Richardson constant A^*_p of 90 A. $cm^{-2}.K^{-2}$ was set. The barrier lowering phenomenon was also considered within the SBH, where φ^0_b, $\Delta\varphi_b$, E_s, and E are the SBH at zero-bias without image force lowering, the barrier variation, the diamond dielectric constant, and the electric field, respectively. Also, a hole tunneling phenomenon through the barrier was considered. The hole tunneling current density J_{tp} is given by the Tsu-Esaki model [176], as seen in the equation

$$J_{tp} = -\frac{4\pi q m^*_{ht} m_0 kT}{h^3}\int_0^{\varphi_{bp}} P(E_z)N(E_z)dE_z \tag{5.3}$$

$$\text{with} \quad P(E_z) = exp\left[\frac{-8\pi(2m^*_{ht}m^*)^{1/2}(\varphi_{bp} - E_z)^{3/2}}{2qhE}\right]$$

$$\text{and} \quad N(E_z) = ln\left[1 + exp\left(\frac{E_F - E_z}{kT}\right)\right]\Big/\left[1 + exp\left(\frac{E_F - E_z - qV}{kT}\right)\right]$$

where m^*_{ht}, m_0, h, $P(E_z)$, and $N(E_z)$ are the hole tunneling mass, electron mass, Planck's constant, transmission probability, and supply function, respectively. In this study, the hole tunneling mass was equal to the hole mass. Supposing that the breakdown voltage is related to avalanche phenomena, Selberherr's impact ionization model is implemented for electrons n and for holes p. The ionization rate model proposed by Selberherr is very similar to the classical Chynoweth model that depends on the electric field as shown in equation 5.1. The difference, however, is in the impact ionization coefficients, which are temperature-dependent parameters. In our case, we assumed that these coefficients are constant since at present no temperature-dependent ionization coefficients have been reported for diamond. Hence, we performed the simulations implementing either the coefficients reported by Watanabe *et al.*, Hiraiwa *et al.* or Kamakura *et al.*, as listed in table 5.1.

Figure 5.2 exhibits the hole and electron ionization parameters $a_{n,p}$ plotted as a function of the inverse of electric field following the expression given in equation 5.1 and values reported by Nguyen *et al.* for 4H-SiC and Watanabe *et al.*, Hiraiwa *et al.* and Kamakura *et al.* for diamond material (cf. table 5.1). Similarly to SiC, the hole ionization rate a_p reported for diamond is higher than the electron ionization rate a_n, except for Watanabe's and Hiraiwa's parameters where the ionization rate for electrons increases after a certain

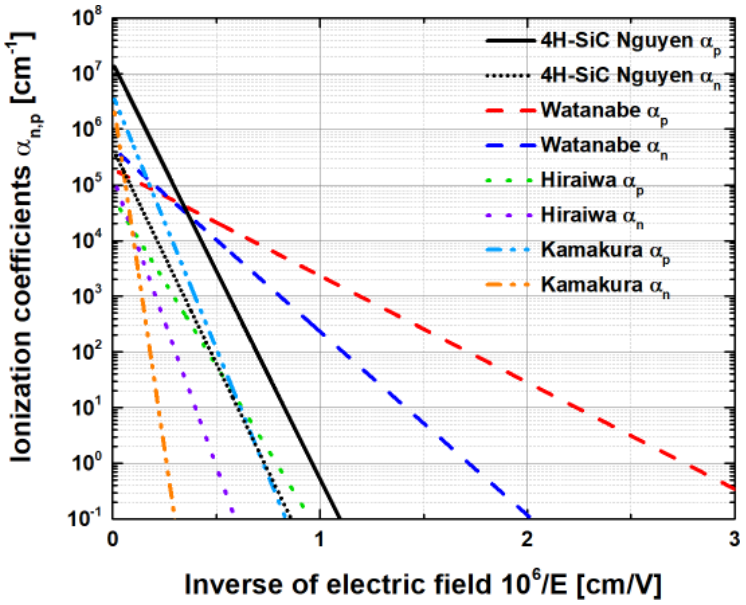

Figure 5.2: Impact ionization rates as a function of electric field at 300K for reported 4H-SiC and diamond.

electric field. The gap between the coefficients that have been published so far is not negligible, and foremost, accurate predictions of the designed structure are impossible.

5.1.2.3 Reverse electrical characteristics

Diode 1 showed a maximum leakage current of 1 μA.cm^{-2} at room temperature for a reverse electrical field of 3 MV.cm^{-1}. The diode exposed its highest operation limit for a bias of 296 V corresponding to a 1D reverse field of 3.1 MV.cm^{-1} as presented in figure 5.3-a. The electric field was calculated from the reverse bias using the 1D formula as follows [170]:

$$E_{1D} = \begin{cases} \frac{2(V+V_{bi})}{W}, & \text{if d} \geq \text{W for NPT.} \\ \frac{qN_A d}{E_s} + \frac{(V - qN_A d^2/2E_s)}{d}, & \text{if d} \leq \text{W for PT.} \end{cases} \quad (5.4)$$

$$\text{with} \quad W = \sqrt{\frac{2E_s}{qN_A}\left(V + V_{bi} - \frac{k_B T}{q}\right)}$$

where d is the thickness of diamond, W the depletion width, and N_A the density of the ionized acceptor. NPT stands for the non-punch through design and PT for the punch-through design. The curve exhibits a TE behavior ending by a sudden increase in leakage current, which is characteristic of the avalanche multiplication event. This sudden increase in leakage current is not due to the thermal runaway of the leakage current since the power density at the measured breakdown is low (about 0.28 mW.cm^{-2}), but only due to the electrostatic runaway. In the same manner, diode 2 in figure 5.3-b exhibits TE and thermionic field emission (TFE) characteristics. Albeit that the measurements

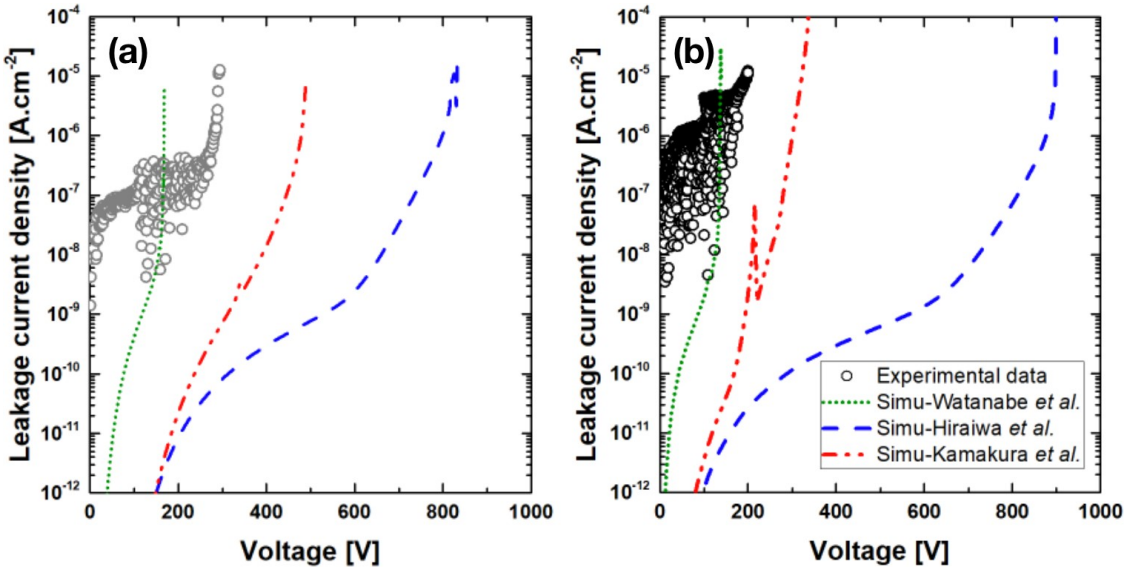

Figure 5.3: Reverse blocking conditions for experimental and simulated simple Schottky barrier diodes at 300 K using (a) Pt Schottky contact for diode 1 and (b) Mo Schottky contact for diode 2.

were stopped at 200V to protect the diode, diode 2 had the highest 1D reverse field of 3.5 MV.cm^{-1}. After implementing the three ionization coefficients in the simulation platform and checking the static limits of the diodes, we observed a discrepancy in the operation limit compared with the experimentally obtained values for both diodes 1 and 2. When using Hiraiwa's coefficients, the breakdown voltage is almost three times higher than the experimental value. The breakdown voltages obtained using Kamakura's and Watanabe's coefficients are closer to the experimental value but still two times higher for the former and two times lower for the latter. At this point, it is premature to say which one is more suitable for the simulation. However, it is clear that a change in impact ionization coefficient results in a notably different predicted breakdown voltage since the ionization integral depends on the choice of the coefficient. As indicated in the previous section, diamond is considered ideal: therefore, we did not include traps or defects, and this is why the leakage current density is very low in the simulation. In this work, we focused only on the breakdown characteristics; as a consequence, the leakage current cannot be interpreted and compared with the experimental result.

5.1.2.4 Ionization coefficients influence on electric field

Figure 5.4 shows the electric field distribution and the current flowlines at the operation limit of the diodes simulated using Watanabe IIC (a)-(a'), Kamakura IIC (b)-(b'), and Hiraiwa IIC (c)-(c'). As expected, the electric field accumulates at the edge of the electrode (labeled point B) and seems to be equally distributed under the electrode (labeled point A). The choice of impact ionization coefficients affects the leakage current location under the main contact. This is because the avalanche parameters play an important role in determining the carrier transport. The leakage current is located under the entire Schottky contact when using Watanabe IIC (a)-(a') and, at the edge when using Hiraiwa IIC (c)-(c') for both diodes, and depends on the diode characteristics when using Kamakura IIC

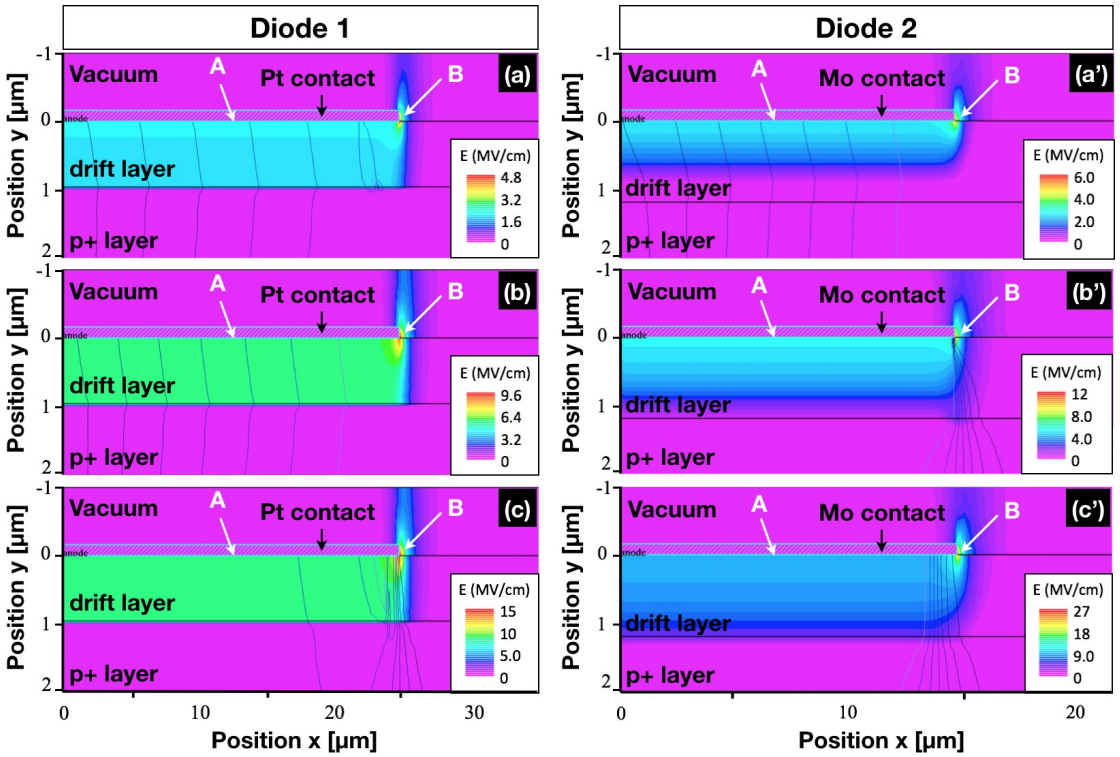

Figure 5.4: Electric field distribution and current flowlines for simulated diode 1 and diode 2 at corresponding breakdown voltages shown in figure 5.3 using (a) Watanabe's, (b) Kamakura's and (c) Hiraiwa's coefficients at 300K. "A" represents the center of the electrode and "B" the point where the peak electric field appears.

(b)-(b'). It is also shown in figure 5.4 that these coefficients change the depletion layer thickness at the predicted avalanche breakdown. Regarding the device parameters and ionization coefficients, the breakdown of the device does not happen in the same region when we consider a breakdown by avalanche phenomena. Indeed, in some cases, the leakage current is located at the edge of the contact, which characterizes a breakdown by avalanche phenomena, and in other instances, located under the entire contact, which is a breakdown due to a current limitation set.

From the structures obtained by simulation, we extracted the electric field as a function of the length represented by the x-axis in figure 5.4 at the metal/diamond interface (y = 0) for the two diodes. The obtained electric field gives a constant value at the center and a maximum value (peak) at the edge of the electrode. As shown in figure 5.5-(a), the peak electric field at 300 K for diode 1 was determined to be 13.5 MV.cm^{-1} for a BV of 832.5 V using Hiraiwa's model, 8.73 MV.cm^{-1} for a BV of 490 V using Kamakura's model, and 4.43 MV.cm^{-1} for a BV of 167 V using Watanabe's model. Diode 2 gave 22 MV.cm^{-1} for a BV of 902 V, 9.87 MV.cm^{-1} for a BV of 415 V, and 4.84 MV.cm^{-1} for a BV of 135 V using Hiraiwa's, Kamakura's, and Watanabe's models, respectively. The maximum electric field for the experimental diode was calculated using a 1D electric field as a function of reverse bias, as explained earlier. We found 3.14 MV.cm^{-1} for diode 1 and 3.5 MV.cm^{-1} for diode 2. Constant short dashed lines in 5.5 represent these values since they were calculated from the 1D formula. These calculated values do not consider the effect of the edge. An infinite contact is assumed to be formed between the metal

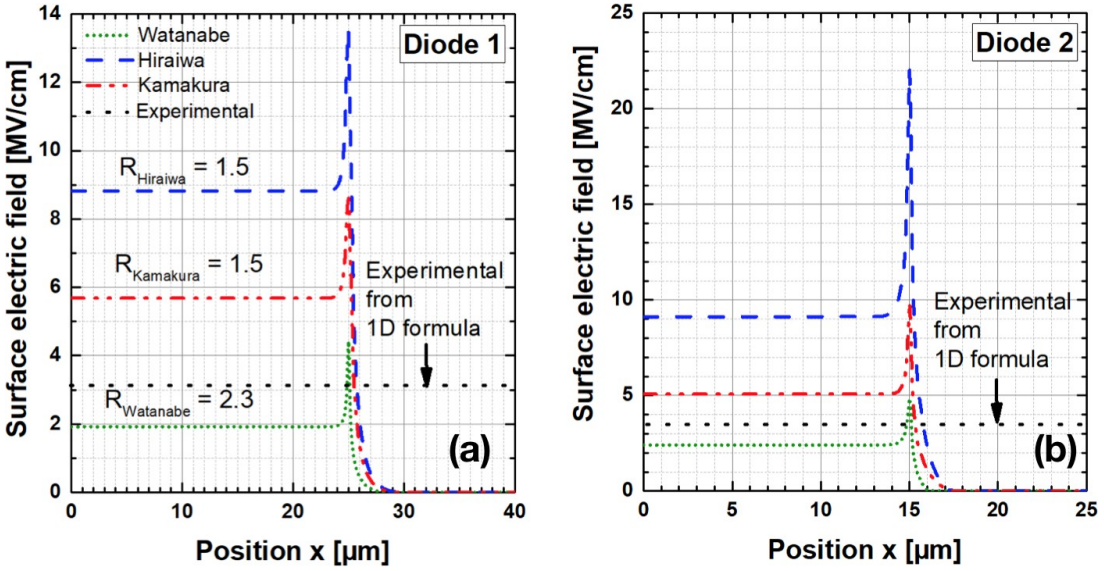

Figure 5.5: Surface electric field at a metal/diamond interface for simulated and experimental (a) diode 1 and (b) diode 2. The electric field is related to breakdown voltages given in figure 5.4 at y=0. The experimental curve was obtained using equation 5.4.

and the semiconductor, and hence, one direction is considered. The distance between the ohmic contact and the Schottky contact is much larger than the depth of the drift layer. Therefore, no effect of the lateral electric field is observed owing to the pseudo-vertical structure. We also show in 5.5 the ratio Ri, which is the maximum electric field at the edge, E_{max}, over the electric field at the center of the electrode, E_{ce} (i represents the impact ionization coefficient used). It allows us to see if the electric field is well relaxed or not. In our simulation, the ratio is extremely low compared with what it is usually reported [44]. Indeed, the electric field at the edge of the electrode reported by Ikeda *et al.* is more than 3 times higher than that at the center of the electrode, especially for a simple structure without any edge termination to smoothly distribute the electric field. This value could be enhanced using a finer mesh in diamond and a complete mesh in vacuum region.

5.2 Impact ionization extraction

5.2.1 Device selection

The Schottky diode with the lowest leakage current and the highest breakdown field is selected for impact ionization extraction. Due to a lack in the process fabrication quality of FFR-SBDs and FP-SBDs, the important leakage current of the diodes, as well as the low breakdown fields, obtained avoid to use them to extract the ionization coefficients. Indeed, a high leakage current will imply inaccuracy in the values. The highest breakdown field obtained for FFR-SBDs and FP-SBDs were only 0.8 MV/cm and 0.55 MV/cm, respectively. It is true that sample FFR#1 has exhibited breakdown field of about 2.5 MV/cm but the leakage current was excessively high.
Therefore, a Schottky diode reported in our previous work was then used [105]. A cross-sectional view is shown in figure 5.6. A pseudo-vertical structure was used with an active

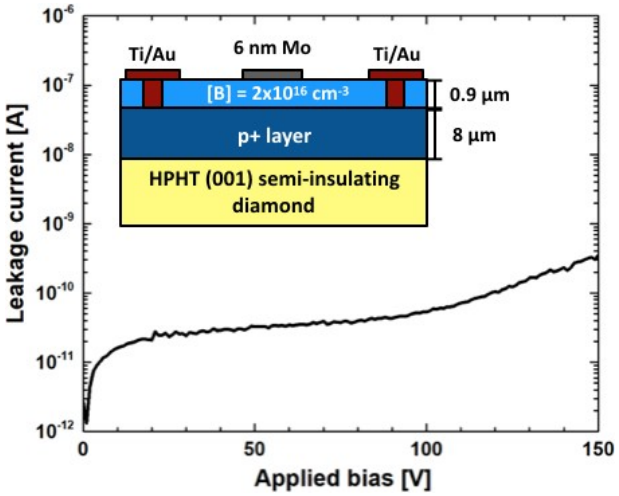

Figure 5.6: Leakage current as a function of the applied bias. The diode exhibits low leakage current up to 150 V. A cross-sectional view is shown.

layer thickness and doping concentration of 0.9 μm and 2 $\times$ 10^{16} cm^{-3}, respectively. The heavily doped boron layer has 8 μm thickness. The Schottky electrode has 6 nm Mo thickness and a diameter of 100 μm. The SBD exhibited a low leakage current and a breakdown field of 1.5 MV/cm (figure 5.6).

5.2.2 Methodology and measurement

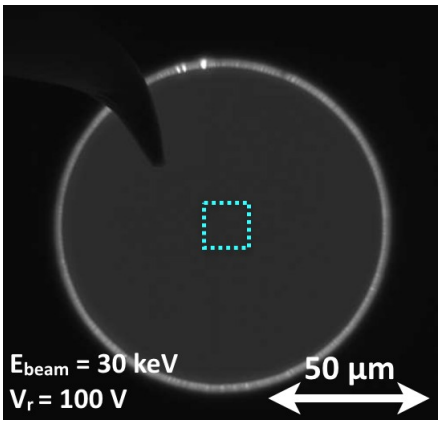

Figure 5.7: Typical EBIC image of the diode used to extract impact ionization coefficients. The electron beam energy was 30 keV. The applied bias was 100 V.

One of the strength in using the electron beam excitation method is to allow extraction of the ionization rates in a defect-free region by selecting an isolating place of the EBIC image. Indeed, as it was discussed previously, a place where a peak electric field occurs, or a defect takes place, induce an enhanced impact ionization rates. It is then important to characterize a diode in a localized region. Thus, EBIC system was used, and analysis of several EBIC images was investigated to extract the mean value of the EBIC intensity at the center of the electrode far away from the edge where the peak electric field appears, as represented in figure 5.7 by the dashed blue square. Therefore, a uniform distribution of the electric field is assumed in the below the center of the electrode. In this representative EBIC image, the applied bias was 100 V and the electron beam energy of 30 keV. The beam current measured by Faraday cage was 1.6 $\times$ 10^{-7} A. The mean value of the EBIC

intensity was obtained using equation 3.7 in chapter 3. Figure 5.8 presents the mean

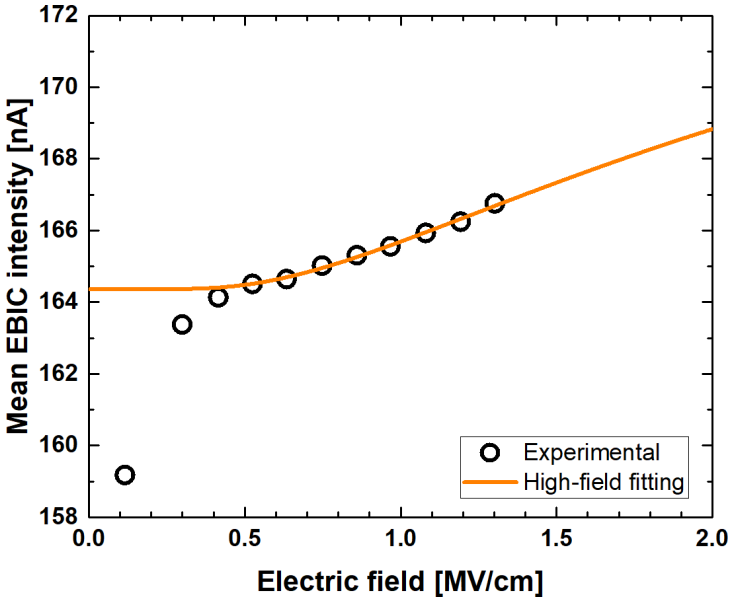

Figure 5.8: Mean EBIC intensities extracted from EBIC images as a function of the electric field under the center of the main Schottky electrode. The fitting was performed for ≥ 0.5 MV/cm.

EBIC intensity as a function of the electric field. The experimental data were fitted using equation 3.8 for an electric field ≥ 0.5 MV/cm because of the assumption of a uniform electric field. At a low electric field, it can be seen that the EBIC intensity is increased when the electric field increases. This rise of the curve corresponds to the increase of the charge collection due to the depletion region expansion in depth. When the drift layer is completely depleted (for ≥ 0.5 MV/cm), an increase of the charge collection occurs due to an increase of the electric field. The impact ionization coefficient for electron extracted in the Chynoweth form for a uniform electric field ≥ 0.5 MV/cm are $a_n = 971\ cm^{-1}$ and $b_n = 2.39 \times 10^6$ V/cm and c=1. As the beam was located near the p-/p+ diamond interface, minority carrier will drift the active layer to reach the Schottky electrode, and hence, will create other electron-hole pairs.

A comparison with the reported electron ionization coefficients in the literature is shown in figure 5.9. The measured ionization coefficient is different from the ones reported by Watanabe, Hiraiwa, and Kamakura. The ionization coefficient is lower than that reported by Skukan. Skukan has extracted the ionization coefficients on an undoped (intrinsic) single crystal CVD diamond layer, and in our study, a boron doped active layer was used. This may induce a difference in the ionization coefficients.

5.3 Conclusion

The importance of the ionization coefficients for reverse state prediction led us to an investigation of accurate extraction of the coefficients. A review of the different ionization coefficients reported in the literature for diamond showed a dispersion of these values that highlight a lack of accuracy. The extracted parameters for the electron impact ionization

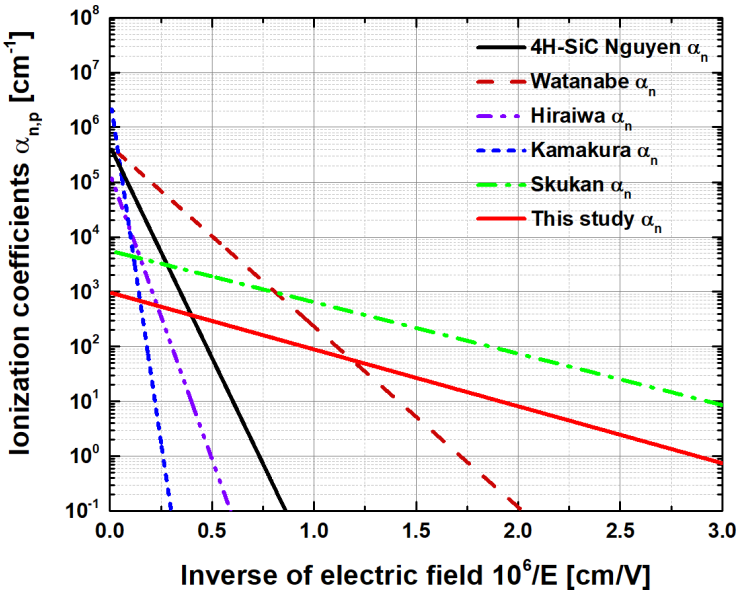

Figure 5.9: Ionization coefficients for electrons as a function of the inverse of the electric field.

were $a_n = 971$ cm^{-1} and $b_n = 2.39 \times 10^6$ V/cm for an electric field $\geq$ 0.5 MV/cm. The ionization rate obtained from this study were lower than the one reported by Skukan [140]. The powerful EBIC analysis played an important role in selecting a defect-free region. Because if defects were present, the ionization would have been larger.

Conclusions and Perspectives

This thesis was dedicated to the accurate extraction of the impact ionization coefficients for diamond semiconductor. The ionization coefficients are important material parameters that give information of diamond physical limits. Thus, they contribute in predicting the device performance when implemented in simulation tools.
The first chapter introduced the context and the place of power electronics in our current society. Among the wide bandgap or ultra wide bandgap materials, diamond is recognized as the ultimate power semiconductor owing to its exceptional properties. Power electronics require devices able to withstand high voltages in the off-state. Some of the reported Schottky barrier diodes (SBDs) have exhibited a breakdown field close to diamond critical field, but the majority know a premature BV and hence, have a low breakdown field. The lack of edge termination technique exploration avoids the development of devices with characteristics near ideality. And this is a big issue to extract the impact ionization coefficients accurately.
Chapter 2 was dedicated to the physics behind SBDs and metal-semiconductor field effect transistors (MESFETs). The Schottky contact that rectifies the diode plays an important role in MESFET working since it controls the modulation of the channel. Equations used to analyze the experimental data in forward and reverse states were recalled. In the second part of this chapter, diamond proper numerical models such as incomplete ionization, temperature and concentration dependence mobility, and positive electron affinity were implemented. The simulation tool is an essential step to go through for device design and physics prediction.
In the third chapter, the steps that led to the fabrication of each device were presented. Diamond device fabrication is a challenging process, especially when complex structures are required. The facilities for diamond device fabrication are limited due to the small size of diamond wafers. Understanding each step of the fabrication through intermediate characterizations contribute to successful device fabrication. The natural process that comes after the process engineering is the characterization. The facilities used to characterize electrically the devices were presented. A powerful system of analysis was also introduced, and its principle of work explained. The electron beam induced current (EBIC) technique was the principal system used to measure the diamond impact ionization coefficients. In fact, in addition to material parameters extraction, EBIC is well known for defect localization and device failure, but it has been shown also that it is a perfect system to investigate surface electric field distribution.
Chapter 4 was focusing on the evaluation of the fabricated edge termination SBDs and MESFETs. Floating field rings (FFRs), as well as field plate (FP) edge termination structure, were investigated to develop a Schottky diode with excellent characteristics. Using EBIC analysis, both of the edge termination structure had exhibited their effectiveness. FFR-SBDs saw its EBIC intensity dropped by 50% and at the same time, the BV was

improved by about 50% when using one ring and a spacing of 150 nm. FP-SBDs have exhibited an improvement of about 34% when using an FP oxide as compared to a simple Schottky diode. However, the highest maximum electric field obtained did not exceed 0.8 MV/cm (for FFR-SBDs) and that is low to extract the impact ionization coefficients accurately. The achieved breakdown field remains low as compared to diamond strength. In reality, the premature breakdown was initiated by the insufficiency of the process fabrication. Even is the edge termination structure were successfully fabricated, still edge metal roughness and edge oxide roughness were notices for FFR-SBDs and FP-SBDs, respectively. The roughness of the edges enhances the electric field crowding which causes an increase of the leakage current and a premature BV. The MESFETs fabricated and characterized in parallel have presented remarkable results. The on-resistance of the bulk channel conduction MESFET was improved by adding a selectively grown heavily doped boron layer beneath the source and drain electrode. The highest BV obtained was nearly 2.3 kV (0.6 MV/cm). To push even more the device off-state, a reverse blocking (RB) type MESFET was realized. The RB-MESFET demonstrated both a low on-resistance of 708 Ω.cm and a high RB-BV of 2379 V. Another RB-MESFET with higher on-resistance (207 kΩ.cm) demonstrated 3 kV reverse blocking capability corresponding to 0.6 MV/cm.
Chapter 5 was focusing on the impact ionization coefficients. In the first section, an analysis of the reported ionization coefficients was performed. The reported coefficients have presented different results when implementing in the simulation tool. This presents the need in extracting accurate values for diamond to be able to predict and to understand the reverse characteristics. As said in the previous paragraph, the ET SBDs have important leakage currents and a low breakdown field, thus, cannot be used for coefficients extraction. A Schottky diode, however, had exhibited a maximum electric field of 1.3 MV/cm and therefore was used to measure the ionization coefficients. EBIC system was used to localize the electron beam excitation far away from defect area. The measured impact ionization coefficients for electrons are $a_n = 971\ cm^{-1}$ and $b_n = 2.39 \times 10^6$ V/cm for an electric field $\geq$ 0.5 MV/cm. These coefficients are lower than the ones reported by Skukan *et al.* but have the same behavior as compared to others.
Indeed, the diamond impact ionization for electrons was successfully extracted however still confirmation need to be realized on a device with a higher maximum electric field.

To obtain accurate impact ionization coefficients for diamond, three undeniable conditions are required: (1) Low (or no) leakage current device is needed; (2) a breakdown voltage near ideality (or as higher as possible since fabrication technologies is not yet mature for diamond); (3) and, a powerful characterization system. In this study, the high breakdown field condition was missing. Further edge termination techniques exploration are needed to find the most appropriate one for diamond.
The field oxide roughness and stress observed because of the lift-off, is now under investigation for a wet etching using acid treatment. Efforts are also pursuing on FFR-SBDs by improving the lithography process. A possibility to overcome metal edge roughness can be achieved by etching even the metal instead of lift-off. After an edge termination structure demonstrates its effectiveness, it can be used for FETs to improve their capabilities. Only after reaching a high breakdown field for diamond that accuracy can be achieved for ionization coefficients.
As a complementary work, hole ionization coefficients can also be extracted using an EBIC system. A different diode such as pin diode can be used to measure the ionization coefficients and compare them with the ones extracted using Schottky diode.

Bibliography

[1] J. Cook, N. Oreskes, P. T. Doran, W. R. Anderegg, B. Verheggen, E. W. Maibach, J. S. Carlton, S. Lewandowsky, A. G. Skuce, S. A. Green, D. Nuccitelli, P. Jacobs, M. Richardson, B. Winkler, R. Painting, and K. Rice, "Consensus on consensus: A synthesis of consensus estimates on human-caused global warming," *Environ. Res. Lett.*, vol. 11, no. 4, 2016.

[2] H. Umezawa, "Recent advances in diamond power semiconductor devices," *Mater. Sci. Semicond. Process.*, vol. 78, no. September 2017, pp. 147–156, 2018.

[3] A. Traoré, P. Muret, A. Fiori, D. Eon, E. Gheeraert, and J. Pernot, "Zr/oxidized diamond interface for high power Schottky diodes," *Appl. Phys. Lett.*, vol. 104, p. 052105, feb 2014.

[4] V. D. Blank, V. S. Bormashov, S. A. Tarelkin, S. G. Buga, M. S. Kuznetsov, D. V. Teteruk, N. V. Kornilov, S. A. Terentiev, and A. P. Volkov, "Power high-voltage and fast response Schottky barrier diamond diodes," *Diam. Relat. Mater.*, vol. 57, pp. 32–36, 2015.

[5] J. Liu, M. Liao, M. Imura, H. Oosato, E. Watanabe, and Y. Koide, "Electrical properties of atomic layer deposited HfO2/Al2O3 multilayer on diamond," *Diam. Relat. Mater.*, vol. 54, pp. 55–58, 2015.

[6] Y. Kitabayashi, T. Kudo, H. Tsuboi, T. Yamada, D. Xu, M. Shibata, D. Matsumura, Y. Hayashi, M. Syamsul, M. Inaba, A. Hiraiwa, and H. Kawarada, "Normally-Off CH Diamond MOSFETs With Partial CO Channel Achieving 2-kV Breakdown Voltage," *IEEE Electron Device Lett.*, vol. 38, pp. 363–366, mar 2017.

[7] G. Chicot, A. Maréchal, R. Motte, P. Muret, E. Gheeraert, and J. Pernot, "Metal oxide semiconductor structure using oxygen-terminated diamond," *Appl. Phys. Lett.*, vol. 102, no. 24, pp. 1–6, 2013.

[8] T. T. Pham, N. Rouger, C. Masante, G. Chicot, F. Udrea, D. Eon, E. Gheeraert, and J. Pernot, "Deep depletion concept for diamond MOSFET," *Appl. Phys. Lett.*, vol. 111, p. 173503, oct 2017.

[9] T. Matsumoto, H. Kato, K. Oyama, T. Makino, M. Ogura, D. Takeuchi, T. Inokuma, N. Tokuda, and S. Yamasaki, "Inversion channel diamond metal-oxide-semiconductor field-effect transistor with normally off characteristics," *Sci. Rep.*, vol. 6, p. 31585, oct 2016.

[10] H. Umezawa, K. Tsugawa, S. Yamanaka, D. Takeuchi, H. Okushi, and H. Kawarada, "High-Performance Diamond Metal-Semiconductor Field-Effect Transistor with 1 m Gate Length," *Jpn. J. Appl. Phys.*, vol. 38, pp. L1222–L1224, nov 1999.

[11] H. Umezawa, T. Matsumoto, and S.-I. Shikata, "Diamond MetalSemiconductor Field-Effect Transistor With Breakdown Voltage Over 1.5 kV," *IEEE Electron Device Lett.*, vol. 35, pp. 1112–1114, nov 2014.

[12] T. Suwa, T. Iwasaki, K. Sato, H. Kato, T. Makino, M. Ogura, D. Takeuchi, S. Yamasaki, and M. Hatano, "Normally-Off Diamond Junction Field-Effect Transistors With Submicrometer Channel," *IEEE Electron Device Lett.*, vol. 37, pp. 209–211, feb 2016.

[13] B. Huang, X. Bai, S. K. Lam, and K. K. Tsang, "Diamond FinFET without Hydrogen Termination," *Sci. Rep.*, vol. 8, p. 3063, dec 2018.

[14] T. Makino, H. Kato, D. Takeuchi, and M. Ogura, "Device Design of Diamond Schottky-pn Diode for Low-Loss Power Electronics Device Design of Diamond Schottky-pn Diode for Low-Loss Power Electronics," vol. 090116, pp. 1–7, 2012.

[15] M. Saremi, R. Hathwar, M. Dutta, F. A. M. Koeck, R. J. Nemanich, S. Chowdhury, and S. M. Goodnick, "Analysis of the reverse I-V characteristics of diamond-based PIN diodes," *Appl. Phys. Lett.*, vol. 111, p. 043507, jul 2017.

[16] H. Kato, T. Makino, M. Ogura, D. Takeuchi, and S. Yamasaki, "Fabrication of bipolar junction transistor on (001)-oriented diamond by utilizing phosphorus-doped n-type diamond base," *Diam. Relat. Mater.*, vol. 34, pp. 41–44, apr 2013.

[17] K. Driche, H. Umezawa, N. Rouger, G. Chicot, and E. Gheeraert, "Characterization of breakdown behavior of diamond Schottky barrier diodes using impact ionization coefficients," *Jpn. J. Appl. Phys.*, vol. 56, p. 04CR12, apr 2017.

[18] K. Driche, S. Rugen, N. Kaminski, H. Umezawa, H. Okumura, and E. Gheeraert, "Electric field distribution using floating metal guard rings edge-termination for Schottky diodes," *Diam. Relat. Mater.*, vol. 82, pp. 160–164, feb 2018.

[19] Oak Ridge National Laboratory, "https://www.ornl.gov."

[20] Mitsubishi Electric's Railcar Traction Inverter with All-SiC Power Modules Achieves 40% Power Saving., "http://www.mitsubishielectric.com/news/2015/0622-a.html."

[21] S. SHIKATA and H. UMEZAWA, "Development of diamond-based power devices," *Synth. English Ed.*, vol. 6, no. 3, pp. 147–157, 2013.

[22] K. Zeng, A. Vaidya, and U. Singisetti, "1.85 kV Breakdown Voltage in Lateral Field-Plated Ga2O3 MOSFETs," *IEEE Electron Device Lett.*, vol. 39, pp. 1385–1388, sep 2018.

[23] H. Umezawa, M. Nagase, Y. Kato, and S. I. Shikata, "High temperature application of diamond power device," *Diam. Relat. Mater.*, vol. 24, pp. 201–205, 2012.

[24] E. Gheeraert, "Fundamental material's nature of diamond," in *Power Electron. Device Appl. Diam. Semicond.*, vol. 1, pp. 191–217, Elsevier, 2018.

[25] P.-N. Volpe, P. Muret, J. Pernot, F. Omnès, T. Teraji, Y. Koide, F. F. Jomard, D. Planson, P. Brosselard, N. Dheilly, B. Vergne, S. Scharnholz, F. Oms, T. Teraji, Y. Koide, F. F. Jomard, D. Planson, P. Brosselard, N. Dheilly, B. Vergne, and S. Scharnholz, "Extreme dielectric strength in boron doped homoepitaxial diamond," *Appl. Phys. Lett.*, vol. 97, p. 223501, nov 2010.

[26] T. Makino, N. Tokuda, H. Kato, S. Kanno, S. Yamasaki, and H. Okushi, "Electrical and light-emitting properties of homoepitaxial diamond p-i-n junction," *Phys. Status Solidi*, vol. 205, no. 9, pp. 2200–2206, 2008.

[27] M. Suzuki, T. Sakai, T. Makino, H. Kato, D. Takeuchi, M. Ogura, H. Okushi, and S. Yamasaki, "Electrical characterization of diamond PiN diodes for high voltage applications," *Phys. Status Solidi*, vol. 210, no. 10, pp. 2035–2039, 2013.

[28] M. Dutta, F. A. M. Koeck, R. Hathwar, S. M. Goodnick, R. J. Nemanich, and S. Chowdhury, "Demonstration of Diamond-Based Schottky p-i-n Diode With Blocking Voltage > 500 V," *IEEE Electron Device Lett.*, vol. 37, pp. 1170–1173, sep 2016.

[29] W. Huang, T. Chow, J. Yang, and J. Butler, "High-voltage diamond Schottky rectifiers," in *Proceedings. IEEE Lester Eastman Conf. High Perform. Devices, 2004.*, no. 1, pp. 248–254, IEEE, 2004.

[30] J. E. Butler, M. W. Geis, K. E. Krohn, J. Lawless, S. Deneault, T. M. Lyszczarz, D. Flechtner, and R. Wright, "Exceptionally high voltage Schottky diamond diodes and low boron doping," *Semicond. Sci. Technol.*, vol. 18, no. 3, pp. S67–S71, 2003.

[31] P. Volpe, P. Muret, J. Pernot, F. Omnès, T. Teraji, F. Jomard, D. Planson, P. Brosselard, N. Dheilly, B. Vergne, and S. Scharnholtz, "High breakdown voltage Schottky diodes synthesized on p-type CVD diamond layer," *Phys. Status Solidi*, vol. 207, pp. 2088–2092, sep 2010.

[32] H. Umezawa, Y. Kato, and S.-i. Shikata, "1 Ω On-Resistance Diamond Vertical-Schottky Barrier Diode Operated at 250 C," *Appl. Phys. Express*, vol. 6, p. 011302, jan 2013.

[33] M. Brezeanu, S. Rashid, G. Amaratunga, N. Rupesinghe, T. Butler, F. Udrea, and G. Brezeanu, "On-State Behaviour of Diamond M-i-P Structures," in *2006 Int. Semicond. Conf.*, pp. 311–314, IEEE, sep 2006.

[34] S. J. Rashid, S. Member, A. Tajani, D. J. Twitchen, L. Coulbeck, F. Udrea, T. Butler, N. L. Rupesinghe, M. Brezeanu, J. Isberg, A. Garraway, M. Dixon, R. S. Balmer, D. Chamund, P. Taylor, G. A. J. Amaratunga, and A. High-quality, "Numerical Parameterization of Diamond for Device Simulation and Analysis," vol. 55, no. 10, pp. 2744–2756, 2008.

[35] T. Makino, S. Tanimoto, H. Kato, N. Tokuda, M. Ogura, D. Takeuchi, K. Oyama, H. Ohashi, H. Okushi, and S. Yamasaki, "Diamond Schottky p-n diode with high forward current density," *Phys. Status Solidi Appl. Mater. Sci.*, vol. 206, no. 9, pp. 2086–2090, 2009.

[36] T. Makino, S. Tanimoto, Y. Hayashi, H. Kato, N. Tokuda, M. Ogura, D. Takeuchi, K. Oyama, H. Ohashi, H. Okushi, and S. Yamasaki, "Diamond Schottky-pn diode with high forward current density and fast switching operation," *Appl. Phys. Lett.*, vol. 94, p. 262101, jun 2009.

[37] T. Matsumoto, T. Mukose, T. Makino, D. Takeuchi, S. Yamasaki, T. Inokuma, and N. Tokuda, "Diamond Schottky-pn diode using lightly nitrogen-doped layer," *Diam. Relat. Mater.*, vol. 75, pp. 152–154, may 2017.

[38] F. La Via, F. Roccaforte, S. di Franco, V. Raineri, F. Moscatelli, A. Scorzoni, and G. Cardinali, "Comparison between Different Schottky Diode Edge Termination

Structures: Simulations and Experimental Results," *Mater. Sci. Forum*, vol. 433-436, pp. 827–830, sep 2003.

[39] L. Seung-Chul, H. Jin-Cherl, K. Soo-Seong, H. Min-Woo, S. Kwang-Seok, C. Yearn-Ik, and H. Min-Koo, "A new vertical GaN Schottky barrier diode with floating metal ring for high breakdown voltage," in *Proc. 16th Int. Symp. Power Semicond. Devices & IC's*, pp. 319–322, IEEE, 2004.

[40] Y. Kato, T. Teraji, and A. Power, "Key technologies for device fabrications and materials characterizations," in *Power Electron. Device Appl. Diam. Semicond.*, pp. 219–294, Elsevier, 2018.

[41] H. Niwa, J. Suda, and T. Kimoto, "Impact Ionization Coefficients in 4H-SiC Toward Ultrahigh-Voltage Power Devices," *IEEE Trans. Electron Devices*, vol. 62, pp. 3326–3333, oct 2015.

[42] Y. Lei, H. Shi, H. Lu, D. Chen, R. Zhang, Y. Zheng, L. Yong, S. Hongbiao, L. Hai, C. Dunjun, Z. Rong, Z. Youdou, Y. Lei, H. Shi, H. Lu, D. Chen, R. Zhang, and Y. Zheng, "Field plate engineering for GaN-based Schottky barrier diodes," *J. Semicond.*, vol. 34, no. 5, p. 054007, 2013.

[43] M. Tarplee, V. Madangarli, Quinchun Zhang, and T. Sudarshan, "Design rules for field plate edge termination in SiC Schottky diodes," *IEEE Trans. Electron Devices*, vol. 48, no. 12, pp. 2659–2664, 2001.

[44] K. Ikeda, H. Umezawa, and S. Shikata, "Edge termination techniques for p-type diamond Schottky barrier diodes," *Diam. Relat. Mater.*, vol. 17, pp. 809–812, apr 2008.

[45] H. Arbess, K. Isoird, S. Hamady, M. Zerarka, and D. Planson, "Original Field Plate to Decrease the Maximum Electric Field Peak for High-Voltage Diamond Schottky Diode," *IEEE Trans. Electron Devices*, vol. 62, pp. 2945–2951, sep 2015.

[46] K. Ikeda, H. Umezawa, N. Tatsumi, K. Ramanujam, and S. ichi Shikata, "Fabrication of a field plate structure for diamond Schottky barrier diodes," *Diam. Relat. Mater.*, vol. 18, no. 2-3, pp. 292–295, 2009.

[47] H. Umezawa, M. Nagase, Y. Kato, and S. Shikata, "Diamond Vertical Schottky Barrier Diode with Al₂O₃ Field Plate," *Mater. Sci. Forum*, vol. 717-720, pp. 1319–1321, may 2012.

[48] M. Brezeanu, T. Butler, N. L. Rupesinghe, G. a. J. Amaratunga, S. J. Rashid, F. Udrea, M. Avram, and G. Brezeanu, "Ramp oxide termination structure using high-k dielectrics for high voltage diamond Schottky diodes," *Diam. Relat. Mater.*, vol. 16, pp. 1020–1024, 2007.

[49] S. Rugen, H. Umezawa, and N. Kaminski, "Floating Metal-Fieldring Edge-Termination of Diamond Schottky Barrier Diodes," in *SBDDXXI Abstr. B.*, p. 94, 2016.

[50] L. Seung-Chul, H. Min-Woo, H. Jin-Cherl, K. Soo-Seong, L. Ji-Yong, S. Kwang-Seok, and H. Min-Koo, "High Breakdown Voltage GaN Schottky Barrier Diode employing Floating Metal Rings on AlGaN/GaN Hetero-junction," in *Proceedings. ISPSD '05. 17th Int. Symp. Power Semicond. Devices ICs, 2005.*, pp. 247–250, IEEE, 2005.

[51] D. C. Sheridan, G. Niu, J. Merrett, J. D. Cressler, C. Ellis, and C.-C. Tin, "Design and fabrication of planar guard ring termination for high-voltage SiC diodes," *Solid. State. Electron.*, vol. 44, pp. 1367–1372, aug 2000.

[52] S.-C. Chang, S.-J. Wang, K.-M. Uang, and B.-W. Liou, "Design and fabrication of high breakdown voltage 4H-SiC Schottky barrier diodes with floating metal ring edge terminations," *Solid. State. Electron.*, vol. 49, pp. 437–444, mar 2005.

[53] a. Aleksov, A. Vescan, M. Kunze, P. Gluche, W. Ebert, E. Kohn, A. Bergmeier, and G. Dollinger, "Diamond junction FETs based on δ-doped channels," *Diam. Relat. Mater.*, vol. 8, pp. 941–945, mar 1999.

[54] T. Iwasaki, Y. Hoshino, K. Tsuzuki, H. Kato, T. Makino, M. Ogura, D. Takeuchi, T. Matsumoto, H. Okushi, S. Yamasaki, and M. Hatano, "Diamond Junction Field-Effect Transistors with Selectively Grown n+-Side Gates," *Appl. Phys. Express*, vol. 5, no. 9, p. 91301, 2012.

[55] T. Iwasaki, Y. Hoshino, K. Tsuzuki, H. Kato, T. Makino, M. Ogura, D. Takeuchi, H. Okushi, S. Yamasaki, and M. Hatano, "High-temperature operation of diamond junction field-effect transistors with lateral p-n junctions," *IEEE Electron Device Lett.*, vol. 34, no. 9, pp. 1175–1177, 2013.

[56] T. Iwasaki, H. Kato, T. Makino, M. Ogura, D. Takeuchi, S. Yamasaki, and M. Hatano, "High-Temperature Bipolar-Mode Operation of Normally-Off Diamond JFET," *IEEE J. Electron Devices Soc.*, vol. 5, pp. 95–99, jan 2017.

[57] T. Iwasaki, J. Yaita, H. Kato, T. Makino, M. Ogura, D. Takeuchi, H. Okushi, S. Yamasaki, and M. Hatano, "600 v Diamond junction field-effect transistors operated at 200 C," *IEEE Electron Device Lett.*, vol. 35, pp. 241–243, feb 2014.

[58] G. Conte, E. Giovine, A. Bolshakov, V. Ralchenko, and V. Konov, "Surface channel MESFETs on hydrogenated diamond," *Nanotechnology*, vol. 23, p. 025201, jan 2012.

[59] E. Giovine, P. Calvani, and D. Trucchi, "Diamond MESFET performance improvement by layout optimisation," *Electron. Lett.*, 2012.

[60] H. Kawarada, M. Aoki, and M. Ito, "Enhancement mode metal-semiconductor field effect transistors using homoepitaxial diamonds," *Appl. Phys. Lett.*, vol. 65, no. 12, pp. 1563–1565, 1994.

[61] M. Liao, J. Liu, L. Sang, D. Coathup, J. Li, M. Imura, Y. Koide, and H. Ye, "Impedance analysis of Al2O3/H-terminated diamond metal-oxide-semiconductor structures," *Appl. Phys. Lett.*, vol. 106, no. 8, pp. 0–5, 2015.

[62] C. Verona, W. Ciccognani, S. Colangeli, E. Limiti, M. Marinelli, G. Verona-Rinati, D. Cannata, M. Benetti, and F. Di Pietrantonio, "V2O5 MISFETs on H-Terminated Diamond," *IEEE Trans. Electron Devices*, vol. 63, no. 12, pp. 4647–4653, 2016.

[63] K. Hirama, H. Sato, Y. Harada, H. Yamamoto, and M. Kasu, "Diamond Field-Effect Transistors with 1.3 A/mm Drain Current Density by Al$ {2}O {3}$ Passivation Layer," *Jpn. J. Appl. Phys.*, vol. 51, p. 090112, aug 2012.

[64] N. Oi, M. Inaba, S. Okubo, I. Tsuyuzaki, T. Kageura, S. Onoda, A. Hiraiwa, and H. Kawarada, "Vertical-type two-dimensional hole gas diamond metal oxide semiconductor field-effect transistors," *Sci. Rep.*, vol. 8, p. 10660, dec 2018.

[65] T.-T. Pham, J. Pernot, G. Perez, D. Eon, E. Gheeraert, and N. Rouger, "Deep-Depletion Mode Boron-Doped Monocrystalline Diamond Metal Oxide Semiconductor Field Effect Transistor," *IEEE Electron Device Lett.*, vol. 38, pp. 1571–1574, nov 2017.

[66] J. Pernot, P. N. Volpe, F. Omnès, P. Muret, V. Mortet, K. Haenen, and T. Teraji, "Hall hole mobility in boron-doped homoepitaxial diamond," *Phys. Rev. B*, vol. 81, p. 205203, may 2010.

[67] C. E. Weitzel, K. J. Nordquist, J. W. Palmour, and C. H. Carter, "4H-SiC MESFET with 2.8 W/mm Power Density at 1.8 GHz," *IEEE Electron Device Lett.*, vol. 15, no. 10, pp. 406–408, 1994.

[68] D. Twitchen, A. Whitehead, S. Coe, J. Isberg, J. Hammersberg, T. Wikstrom, and E. Johansson, "High-voltage single-crystal diamond diodes," *IEEE Trans. Electron Devices*, vol. 51, pp. 826–828, may 2004.

[69] S. Sze and K. K. Ng, *Physics of semiconductor devices*. Wiley, 2006.

[70] J. Andrews and M. Lepselter, "Reverse current-voltage characteristics of metal-silicide Schottky diodes," *Solid. State. Electron.*, vol. 13, pp. 1011–1023, jul 1970.

[71] R. T. Tung, "Electron transport at metal-semiconductor interfaces: General theory," *Phys. Rev. B*, vol. 45, pp. 13509–13523, jun 1992.

[72] R. T. Tung, "Formation of an electric dipole at metal-semiconductor interfaces," *Phys. Rev. B*, vol. 64, p. 205310, nov 2001.

[73] A. Traore, *High Power Diamond Schottky Diode*. PhD thesis, Université de Grenoble, 2014.

[74] G. Chicot, *Field effect in boron doped diamond*. PhD thesis, Université de Grenoble, 2013.

[75] Y. Varshni, "Temperature dependence of the energy gap in semiconductors," *Physica*, vol. 34, no. 1, pp. 149–154, 1967.

[76] C. D. Clark, P. J. Dean, and P. V. Harris, "Intrinsic Edge Absorption in Diamond," *Proc. R. Soc. A Math. Phys. Eng. Sci.*, vol. 277, pp. 312–329, feb 1964.

[77] G. Chicot, T. N. Tran Thi, A. Fiori, F. Jomard, E. Gheeraert, E. Bustarret, and J. Pernot, "Hole transport in boron delta-doped diamond structures," *Appl. Phys. Lett.*, vol. 101, no. 16, 2012.

[78] H. Kawarada, "High-current metal oxide semiconductor field-effect transistors on h-terminated diamond surfaces and their high-frequency operation," *Jpn. J. Appl. Phys.*, vol. 51, pp. 1–6, 2012.

[79] J. Liu, M. Liao, M. Imura, A. Tanaka, H. Iwai, and Y. Koide, "Low on-resistance diamond field effect transistor with high-k ZrO2 as dielectric," *Sci. Rep.*, vol. 4, pp. 2–6, 2014.

[80] A. Maréchal, *Metal-Oxide-Semiconductor capacitor for diamond transistor: simulation, fabrication and electrical analysis*. PhD thesis, Université Grenoble Alpes, 2015.

[81] K. Okano, H. Naruki, Y. Akiba, T. Kurosu, M. Iida, Y. Hirose, and T. Nakamura, "Characterization of Boron-Doped Diamond Film," *Jpn. J. Appl. Phys.*, vol. 28, pp. 1066–1071, jun 1989.

[82] N. Fujimori, H. Nakahata, and T. Imai, "Properties of Boron-Doped Epitaxial Diamond Films," *Jpn. J. Appl. Phys.*, vol. 29, pp. 824–827, may 1990.

[83] E. P. Visser, G. J. Bauhuis, G. Janssen, W. Vollenberg, J. P. van Enckevort, and L. J. Giling, "Electrical conduction in homoepitaxial, boron-doped diamond films," *J. Phys. Condens. Matter*, vol. 4, pp. 7365–7376, sep 1992.

[84] J. A. Von Windheim, V. Venkatesan, D. M. Malta, and K. Das, "Electrical characterization of semiconducting diamond thin films and single crystals," *J. Electron. Mater.*, vol. 22, pp. 391–398, apr 1993.

[85] T. Borst and O. Weis, "Electrical characterization of homoepitaxial diamond films doped with B, P, Li and Na during crystal growth," *Diam. Relat. Mater.*, vol. 4, pp. 948–953, may 1995.

[86] M. Deguchi, M. Kitabatake, and T. Hirao, "Electrical properties of boron-doped diamond films prepared by microwave plasma chemical vapour deposition," *Thin Solid Films*, vol. 281-282, pp. 267–270, aug 1996.

[87] J.-P. Lagrange, A. Deneuville, and E. Gheeraert, "A large range of boron doping with low compensation ratio for homoepitaxial diamond films," *Carbon N. Y.*, vol. 37, pp. 807–810, apr 1999.

[88] E. Bustarret, P. Achatz, B. Sacépé, C. Chapelier, C. Marcenat, L. Ortéga, and T. Klein, "Metal-to-insulator transition and superconductivity in boron-doped dia- mond," *Philos. Trans. R. Soc. A Math. Phys. Eng. Sci.*, vol. 366, no. 1863, pp. 267– 279, 2008.

[89] W. Gajewski, P. Achatz, O. a. Williams, K. Haenen, E. Bustarret, M. Stutzmann, and J. a. Garrido, "Electronic and optical properties of boron-doped nanocrystalline diamond films," *Phys. Rev. B*, vol. 79, p. 045206, jan 2009.

[90] P.-N. Volpe, J. Pernot, P. Muret, and F. Omnès, "High hole mobility in boron doped diamond for power device applications," *Appl. Phys. Lett.*, vol. 94, p. 092102, mar 2009.

[91] S. Koizumi, M. Kamo, Y. Sato, H. Ozaki, and T. Inuzuka, "Growth and characterization of phosphorous doped {111} homoepitaxial diamond thin films," *Appl. Phys. Lett.*, vol. 71, pp. 1065–1067, aug 1997.

[92] H. Kato, S. Yamasaki, and H. Okushi, "n-type doping of (001)-oriented single-crystalline diamond by phosphorus," *Appl. Phys. Lett.*, vol. 86, p. 222111, may 2005.

[93] H. Kato, T. Makino, S. Yamasaki, and H. Okushi, "n-type diamond growth by phosphorus doping on (0 0 1)-oriented surface," *J. Phys. D. Appl. Phys.*, vol. 40, pp. 6189–6200, oct 2007.

[94] M.-A. Pinault, J. Barjon, T. Kociniewski, F. Jomard, and J. Chevallier, "The n-type doping of diamond: Present status and pending questions," *Phys. B Condens. Matter*, vol. 401-402, pp. 51–56, dec 2007.

[95] H. Kato, H. Umezawa, N. Tokuda, D. Takeuchi, H. Okushi, and S. Yamasaki, "Low specific contact resistance of heavily phosphorus-doped diamond film," *Appl. Phys. Lett.*, vol. 93, p. 202103, nov 2008.

[96] M.-A. Pinault-Thaury, T. Tillocher, N. Habka, D. Kobor, F. Jomard, J. Chevallier, and J. Barjon, "n-Type CVD diamond: Epitaxy and doping," *Mater. Sci. Eng. B*, vol. 176, pp. 1401–1408, oct 2011.

[97] I. Stenger, M.-A. Pinault-Thaury, T. Kociniewski, A. Lusson, E. Chikoidze, F. Jomard, Y. Dumont, J. Chevallier, and J. Barjon, "Impurity-to-band activation energy in phosphorus doped diamond," *J. Appl. Phys.*, vol. 114, p. 073711, aug 2013.

[98] G. L. Pearson and J. Bardeen, "Electrical Properties of Pure Silicon and Silicon Alloys Containing Boron and Phosphorus," *Phys. Rev.*, vol. 75, pp. 865–883, mar 1949.

[99] J. Barjon, E. Chikoidze, F. Jomard, Y. Dumont, M.-a. A. Pinault-Thaury, R. Issaoui, O. Brinza, J. Achard, and F. Silva, "Homoepitaxial boron-doped diamond with very low compensation," *Phys. Status Solidi Appl. Mater. Sci.*, vol. 209, no. 9, pp. 1750–1753, 2012.

[100] M. Gabrysch, S. Majdi, A. Hallén, M. Linnarsson, A. Schöner, D. Twitchen, and J. Isberg, "Compensation in boron-doped CVD diamond," *Phys. Status Solidi Appl. Mater. Sci.*, vol. 205, no. 9, pp. 2190–2194, 2008.

[101] M. Werner, R. Locher, W. Kohly, D. Holmes, S. Klose, and H. Fecht, "The diamond Irvin curve," *Diam. Relat. Mater.*, vol. 6, pp. 308–313, mar 1997.

[102] K. Tsukioka and H. Okushi, "Hall Mobility and Scattering Mechanism of Holes in Boron-Doped Homoepitaxial Chemical Vapor Deposition Diamond Thin Films," *Jpn. J. Appl. Phys.*, vol. 45, pp. 8571–8577, nov 2006.

[103] A. Traoré, S. Koizumi, and J. Pernot, "Effect of n- and p-type doping concentrations and compensation on the electrical properties of semiconducting diamond," *Phys. status solidi*, vol. 213, pp. 2036–2043, aug 2016.

[104] T. Klein, P. Achatz, J. Kacmarcik, C. Marcenat, F. Gustafsson, J. Marcus, E. Bustarret, J. Pernot, F. Omnes, B. E. Sernelius, C. Persson, a. Ferreira Da Silva, and C. Cytermann, "Metal-insulator transition and superconductivity in boron-doped diamond," *Phys. Rev. B - Condens. Matter Mater. Phys.*, vol. 75, pp. 1–7, 2007.

[105] H. Umezawa, H. Gima, K. Driche, Y. Kato, T. Yoshitake, Y. Mokuno, and E. Gheeraert, "Defect and field-enhancement characterization through electron-beam-induced current analysis," *Appl. Phys. Lett.*, vol. 110, p. 182103, may 2017.

[106] A. G. Chynoweth, "Ionization Rates for Electrons and Holes in Silicon," *Phys. Rev.*, vol. 109, pp. 1537–1540, mar 1958.

[107] T. Watanabe, M. Irie, T. Teraji, T. Ito, Y. Kamakura, and K. Taniguchi, "Impact Excitation of Carriers in Diamond under Extremely High Electric Fields," *Jpn. J. Appl. Phys.*, vol. 40, no. 7, pp. L715–L717, 2001.

[108] A. Hiraiwa and H. Kawarada, "Figure of merit of diamond power devices based on accurately estimated impact ionization processes," *J. Appl. Phys.*, vol. 114, no. 3, 2013.

[109] R. McIntyre, "Multiplication noise in uniform avalanche diodes," *IEEE Trans. Electron Devices*, vol. ED-13, pp. 164–168, jan 1966.

[110] B. J. Baliga, *Fundamentals of Power Semiconductor Devices*. Springer US, 2008.

[111] New Diamond Technology, "http://ndtcompany.com."

[112] S. J. Sque, R. Jones, and P. R. Briddon, "Structure, electronics, and interaction of hydrogen and oxygen on diamond surfaces," *Phys. Rev. B - Condens. Matter Mater. Phys.*, vol. 73, no. 8, pp. 1–15, 2006.

[113] L. F. Dobrzhinetskaya, "Microdiamonds Frontier of ultrahigh-pressure metamorphism: A review," *Gondwana Res.*, vol. 21, pp. 207–223, jan 2012.

[114] J. Fridrichová, P. Bačík, R. Škoda, and P. Antal, "Use of spectroscopic methods for determination of diamond origin and treatment," *Acta Geol. Slovaca*, vol. 7, no. 1, pp. 11–18, 2015.

[115] F. P. Bundy, "Direct Conversion of Graphite to Diamond in Static Pressure Apparatus," *Science (80-.).*, vol. 137, pp. 1057–1058, sep 1962.

[116] R. Abbaschian, H. Zhu, and C. Clarke, "High pressurehigh temperature growth of diamond crystals using split sphere apparatus," *Diam. Relat. Mater.*, vol. 14, pp. 1916–1919, nov 2005.

[117] S. Ohmagari, H. Yamada, N. Tsubouchi, H. Umezawa, A. Chayahara, S. Tanaka, and Y. Mokuno, "Large reduction of threading dislocations in diamond by hot-filament chemical vapor deposition accompanying W incorporations," *Appl. Phys. Lett.*, vol. 113, no. 3, p. 032108, 2018.

[118] N. Tokuda, H. Umezawa, K. Yamabe, H. Okushi, and S. Yamasaki, "Hillock-free heavily boron-doped homoepitaxial diamond films on misoriented (001) substrates," *Japanese J. Appl. Physics, Part 1 Regul. Pap. Short Notes Rev. Pap.*, vol. 46, no. 4, pp. 1469–1470, 2007.

[119] Diamfab, "http://diamfab.eu."

[120] M. Yamamoto, T. Teraji, and T. Ito, "Improvement in the crystalline quality of homoepitaxial diamond films by oxygen plasma etching of mirror-polished diamond substrates," *J. Cryst. Growth*, vol. 285, pp. 130–136, 2005.

[121] J. Achard, A. Tallaire, V. Mille, M. Naamoun, O. Brinza, A. Boussadi, L. William, and A. Gicquel, "Improvement of dislocation density in thick CVD single crystal diamond films by coupling H2/O2 plasma etching and chemo-mechanical or ICP treatment of HPHT substrates," *Phys. Status Solidi Appl. Mater. Sci.*, vol. 211, no. 10, pp. 2264–2267, 2014.

[122] P. J. Dean, E. C. Lightowlers, and D. R. Wight, "Intrinsic and Extrinsic Recombination Radiation from Natural and Synthetic Aluminum-Doped Diamond," *Phys. Rev.*, vol. 140, pp. A352–A368, oct 1965.

[123] F. Omnès, P. Muret, P. N. Volpe, M. Wade, J. Pernot, and F. Jomard, "Study of boron doping in MPCVD grown homoepitaxial diamond layers based on cathodoluminescence spectroscopy, secondary ion mass spectroscopy and capacitance-voltage measurements," *Diam. Relat. Mater.*, vol. 20, no. 7, pp. 912–916, 2011.

[124] R. Kumaresan, H. Umezawa, and S. Shikata, "Vertical structure Schottky barrier diode fabrication using insulating diamond substrate," *Diam. Relat. Mater.*, vol. 19, pp. 1324–1329, oct 2010.

[125] S. Kono, T. Teraji, H. Kodama, K. Ichikawa, S. Ohnishi, and A. Sawabe, "Direct determination of the barrier height of Ti-based ohmic contact on p-type diamond (001)," *Diam. Relat. Mater.*, vol. 60, pp. 117–122, 2015.

[126] W. E. Martinez, G. Gregori, and T. Mates, "Titanium diffusion in gold thin films," *Thin Solid Films*, vol. 518, pp. 2585–2591, mar 2010.

[127] M. Wu, J. Moulin, S. Lani, G. Hallais, C. Renard, and A. Bosseboeuf, "Low temperature activation of Au/Ti getter film for application to wafer-level vacuum packaging," *Jpn. J. Appl. Phys.*, vol. 54, p. 030220, mar 2015.

[128] T. Tachibana, B. E. Williams, and J. T. Glass, "Correlation of the Electrical-Properties of Metal Contacts on Diamond Films With the Chemical Nature of the Metal-Diamond Interface .2. Titanium Contacts - a Carbide-Forming Metal," *Phys. Rev. B*, vol. 45, no. 20, pp. 11975–11981, 1992.

[129] S. Ghodbane, D. Ballutaud, A. Deneuville, and C. Baron, "Influence of boron concentration on the XPS spectra of the (100) surface of homoepitaxial boron-doped diamond films," *Phys. Status Solidi Appl. Mater. Sci.*, vol. 203, no. 12, pp. 3147–3151, 2006.

[130] A. Maréchal, Y. Kato, M. Liao, and S. Koizumi, "Interfacial energy barrier height of Al2O3/H-terminated (111) diamond heterointerface investigated by X-ray photoelectron spectroscopy," *Appl. Phys. Lett.*, vol. 111, p. 141605, oct 2017.

[131] Y. G. Chen, M. Ogura, and H. Okushi, "Schottky junction properties on high quality boron-doped homoepitaxial diamond thin films," *J. Vac. Sci. Technol. B Microelectron. Nanom. Struct.*, vol. 22, no. 4, p. 2084, 2004.

[132] H. Umezawa and S.-i. Shikata, "Leakage current analysis of diamond Schottky barrier diodes operated at high temperature," *Jpn. J. Appl. Phys.*, vol. 53, no. 4, p. 04EP04, 2014.

[133] T. Teraji, Y. Garino, Y. Koide, and T. Ito, "Low-leakage p-type diamond Schottky diodes prepared using vacuum ultraviolet light/ozone treatment," *J. Appl. Phys.*, vol. 105, pp. 2009–2011, 2009.

[134] X. Wang, A. R. Ruslinda, Y. Ishiyama, Y. Ishii, and H. Kawarada, "Higher coverage of carboxylic acid groups on oxidized single crystal diamond (001)," *Diam. Relat. Mater.*, vol. 20, no. 10, pp. 1319–1324, 2011.

[135] H. Umezawa, K. Ikeda, N. Tatsumi, K. Ramanujam, and S. I. Shikata, "Device scaling of pseudo-vertical diamond power Schottky barrier diodes," *Diam. Relat. Mater.*, vol. 18, no. 9, pp. 1196–1199, 2009.

[136] T. Sakai, K.-S. Song, H. Kanazawa, Y. Nakamura, H. Umezawa, M. Tachiki, and H. Kawarada, "Ozone-treated channel diamond field-effect transistors," *Diam. Relat. Mater.*, vol. 12, pp. 1971–1975, oct 2003.

[137] H. J. Leamy, "Charge collection scanning electron microscopy," *J. Appl. Phys.*, vol. 53, no. 6, 1982.

[138] T. Shimaoka, J. H. Kaneko, Y. Sato, M. Tsubota, H. Shimmyo, A. Chayahara, H. Watanabe, H. Umezawa, and Y. Mokuno, "Fano factor evaluation of diamond detectors for alpha particles," *Phys. Status Solidi Appl. Mater. Sci.*, vol. 213, no. 10, pp. 2629–2633, 2016.

[139] K. Kanaya and S. Okayama, "Penetration and energy-loss theory in solid targets," *J.Phys.D:Appl.Phys.*, vol. 5, pp. 43–58, 1972.

[140] N. Skukan, V. Grilj, I. Sudić, M. Pomorski, W. Kada, T. Makino, Y. Kambayashi, Y. Andoh, S. Onoda, S. Sato, T. Ohshima, T. Kamiya, and M. Jakšić, "Charge multiplication effect in thin diamond films," *Appl. Phys. Lett.*, vol. 109, no. 4, pp. 1–6, 2016.

[141] R. Kumaresan, H. Umezawa, N. Tatsumi, K. Ikeda, and S. Shikata, "Device processing, fabrication and analysis of diamond pseudo-vertical Schottky barrier diodes with low leak current and high blocking voltage," *Diam. Relat. Mater.*, vol. 18, pp. 299–302, feb 2009.

[142] S. Ohmagari, T. Teraji, and Y. Koide, "Non-destructive detection of killer defects of diamond Schottky barrier diodes," *J. Appl. Phys.*, vol. 110, p. 056105, sep 2011.

[143] G. Chen, L. Wang, R. Huang, S. Bai, and Y. Li, "Study on 2000V SiC JBS Diodes," in *Proc. 3rd Int. Conf. Electr. Electron.*, no. Eeic, (Paris, France), pp. 308–310, Atlantis Press, 2013.

[144] V. Veliadis, M. Mccoy, T. Mcnutt, H. Hearne, L.-s. Chen, G. Desalvo, C. Clarke, B. Geil, D. Katsis, and S. Scozzie, "Fabrication of a robust high-performance floating guard ring edge termination for power Silicon Carbide Vertical Junction Field Effect Transistors VJFET first ring GRs," in *Proc. Compd. Semicond. MANTECH Conf.*, (Austin, TX, USA), pp. 217–221, 2007.

[145] H. Umezawa, T. Saito, N. Tokuda, M. Ogura, S.-G. Ri, H. Yoshikawa, and S.-i. Shikata, "Leakage current analysis of diamond Schottky barrier diode," *Appl. Phys. Lett.*, vol. 90, p. 073506, feb 2007.

[146] H. Umezawa, N. Tokuda, M. Ogura, S.-G. G. Ri, and S.-i. I. Shikata, "Characterization of leakage current on diamond Schottky barrier diodes using thermionic-field emission modeling," *Diam. Relat. Mater.*, vol. 15, pp. 1949–1953, nov 2006.

[147] A. Pugatschow, R. Heiderhoff, and L. J. Balk, "Quantitative determination of electric field strengths within dynamically operated devices using EBIC analysis in the SEM," *Scanning*, vol. 30, pp. 324–330, jul 2008.

[148] H. Umezawa, H. Taniuchi, T. Arima, H. Ishizaka, N. Fujihara, Y. Ohba, M. Tachiki, and H. Kawarada, "High frequency application of high transconductance surface-channel diamond field-effect transistors," *Proc. 13th Int. Symp. Power Semicond. Devices ICs. IPSD '01 (IEEE Cat. No.01CH37216)*, pp. 195–198, 2001.

[149] P. Gluche, A. Aleksov, A. Vescan, W. Ebert, and E. Kohn, "Diamond surface-channel FET structure with 200 V breakdown voltage," *IEEE Electron Device Lett.*, vol. 18, pp. 547–549, nov 1997.

[150] Y. G. Chen, M. Ogura, S. Yamasaki, and H. Okushi, "Investigation of specific contact resistance of ohmic contacts to B-doped homoepitaxial diamond using transmission line model," *Diam. Relat. Mater.*, vol. 13, pp. 2121–2124, 2004.

[151] Y. Chen, M. Ogura, S. Yamasaki, and H. Okushi, "Ohmic contacts on p-type homoepitaxial diamond and their thermal stability," *Semicond. Sci. Technol.*, vol. 20, pp. 860–863, 2005.

[152] C. A. Hewett, M. J. Taylor, N. C. Control, and J. Z. Division, "Specific contact resistance measurements to semiconducting diamond of ohmic contacts," *J. Appl. Phys.*, vol. 77, no. 2, pp. 755–760, 1995.

[153] S. Ohmagari, T. Matsumoto, H. Umezawa, and Y. Mokuno, "Ohmic contact formation to heavily boron-doped p+ diamond prepared by hot-filament chemical vapor deposition," *MRS Adv.*, vol. 1, no. 51, pp. 3489–3495, 2016.

[154] C. Klumpner and F. Blaabjerg, "Using reverse-blocking IGBTs in power converters for adjustable-speed drives," *IEEE Trans. Ind. Appl.*, vol. 42, pp. 807–816, may 2006.

[155] M. Takei, Y. Harada, and K. Ueno, "600 V-IGBT with reverse blocking capabil- ity," in *Proc. 13th Int. Symp. Power Semicond. Devices ICs. IPSD '01 (IEEE Cat. No.01CH37216)*, pp. 413–416, Inst. Electr. Eng. Japan, 2001.

[156] S. Mori, M. Aketa, T. Sakaguchi, H. Asahara, T. Nakamura, and T. Kimoto, "Demonstration of 3 kV 4H-SiC reverse blocking MOSFET," in *2016 28th Int. Symp. Power Semicond. Devices ICs*, pp. 271–274, IEEE, jun 2016.

[157] C.-H. Chen and D. Arch, "The influence of electric field and mobility profile on GaAs MESFET characteristics," *IEEE Trans. Electron Devices*, vol. 36, no. 11, pp. 2405–2414, 1989.

[158] M. Riaz, M. M. Ahmed, U. Rafique, and U. F. Ahmed, "Assessment of intrinsic small signal parameters of submicron SiC MESFETs," *Solid. State. Electron.*, vol. 139, no. April 2017, pp. 80–87, 2018.

[159] K. Driche, H. Umezawa, S. Ohmagari, H. Okumura, Y. Mokuno, and E. Gheer- aert, "Electric Field Characterization of Diamond Metal Semiconductor Field Effect Transistors Using Electron Beam Induced Current," *Mater. Sci. Forum*, vol. 924, pp. 935–938, jun 2018.

[160] S. Ohmagari, T. Matsumoto, H. Umezawa, and Y. Mokuno, "Submicron-scale diamond selective-area growth by hot-filament chemical vapor deposition," *Thin Solid Films*, vol. 615, pp. 239–242, sep 2016.

[161] T. Tokunaga, T. Narushima, T. Yonezawa, T. Sudo, S. Okubo, S. Komatsub- ara, K. Sasaki, and T. Yamamoto, "Temperature distributions of electron beam- irradiated samples by scanning electron microscopy," *J. Microsc.*, vol. 248, no. 3, pp. 228–233, 2012.

[162] K. Lehovec and R. Miller, "Field distribution in junction field-effect transistors at large drain voltages," *IEEE Trans. Electron Devices*, vol. 22, pp. 273–281, may 1975.

[163] G. Chicot, D. Eon, and N. Rouger, "Optimal drift region for diamond power devices," *Diam. Relat. Mater.*, vol. 69, pp. 68–73, 2016.

[164] A. Hiraiwa and H. Kawarada, "Blocking characteristics of diamond junctions with a punch-through design," *J. Appl. Phys.*, vol. 117, no. 12, 2015.

[165] Y. Kamakura, T. Kotani, K. Konaga, N. Minamitani, G. Wakimura, and N. Mori, "Ab initio study of avalanche breakdown in diamond for power device applications," in *2015 IEEE Int. Electron Devices Meet.*, no. 6, pp. 5.2.1–5.2.4, IEEE, dec 2015.

[166] R. Trew, J.-B. Yan, and P. Mock, "The potential of diamond and SiC electronic devices for microwave and millimeter-wave power applications," *Proc. IEEE*, vol. 79, pp. 598–620, may 1991.

[167] J. Isberg, M. Gabrysch, A. Tajani, and D. Twitchen, "High-Field Electrical Transport in Single Crystal CVD Diamond Diodes," *Adv. Sci. Technol.*, vol. 48, pp. 73–76, oct 2006.

[168] S. Rashid, A. Tajani, L. Coulbeck, M. Brezeanu, A. Garraway, T. Butler, N. Rupesinghe, D. Twitchen, G. Amaratunga, F. Udrea, P. Taylor, M. Dixon, and J. Is- berg, "Modelling of single-crystal diamond Schottky diodes for high-voltage appli- cations," *Diam. Relat. Mater.*, vol. 15, pp. 317–323, feb 2006.

[169] D. M. Nguyen, C. Raynaud, N. Dheilly, M. Lazar, D. Tournier, P. Brosselard, and D. Planson, "Experimental determination of impact ionization coefficients in 4H- SiC," *Diam. Relat. Mater.*, vol. 20, no. 3, pp. 395–397, 2011.

[170] H. Umezawa, K. Ikeda, R. Kumaresan, N. Tatsumi, and S.-i. Shikata, "Increase in Reverse Operation Limit by Barrier Height Control of Diamond Schottky Barrier Diode," *IEEE Electron Device Lett.*, vol. 30, pp. 960–962, sep 2009.

[171] H. Umezawa, Y. Mokuno, H. Yamada, A. Chayahara, and S.-i. Shikata, "Characterization of Schottky barrier diodes on a 0.5-inch single-crystalline CVD diamond wafer," *Diam. Relat. Mater.*, vol. 19, pp. 208–212, feb 2010.

[172] T. Teraji, S. Koizumi, Y. Koide, and T. Ito, "Electric field breakdown of lateral-type Schottky diodes formed on lightly doped homoepitaxial diamond," *Appl. Surf. Sci.*, vol. 254, pp. 6273–6276, jul 2008.

[173] J. Shirafuji and S. Takashi, "Electrical properties of diamond surfaces," *Diam. Relat. Mater.*, vol. 5, pp. 706–713, 1996.

[174] A. Maréchal, N. Rouger, J.-C. Crébier, J. Pernot, S. Koizumi, T. Teraji, and E. Gheeraert, "Model implementation towards the prediction of J(V) characteristics in diamond bipolar device simulations," *Diam. Relat. Mater.*, vol. 43, pp. 34–42, mar 2014.

[175] C. Crowell and S. M. Sze, "Current transport in metal-semiconductor barriers," *Solid. State. Electron.*, vol. 9, pp. 1035–1048, 1966.

[176] R. Tsu and L. Esaki, "Tunneling in a finite superlattice," *Appl. Phys. Lett.*, vol. 22, pp. 562–564, jun 1973.